Electrical Characterization of Semiconductor Nanostructures by Conductive Probe Based Atomic Force Microscopy Techniques

Igor Beinik

A dissertation submitted to the Institute of Physics
Montanuniversität Leoben
in partial fulfillment of the requirements for the degree of

Doktor der montanistischen Wissenschaften

Under supervision of
Ao. Univ. Prof. Dr. Christian Teichert

Refereed by
Ao. Univ. Prof. Dr. Christian Teichert
and
Univ. Prof. PhD Peter Hadley

Institute of Physics

Montanuniversität Leoben

March 2011

Eidesstattliche Erklärung

The author attests that permission has been obtained for the use of any copyrighted material appearing in this thesis (other than brief excerpts requiring only proper acknowledgment in scholarly writing) and that all such use is clearly acknowledged.

Ich erkläre hiermit, dass ich die vorliegende Arbeit selbst verfasst habe. Außer den angeführten wurden keine Hilfsmittel und Quellen verwendet. Stellen, die aus anderen Arbeiten übernommen wurden, sind als solche gekennzeichnet.

Leoben, March 2011, Igor Beinik

Abstract

Low dimensional semiconductor structures exhibit novel physical properties which resulted already in devices like quantum well lasers, high electron mobility transistors, solar cells, etc. With shrinking dimensions of these structures, there is a need for their physical characterization on the nanometer scale. At this point, modern scanning probe microscopy comes into play: The conductive probe based atomic force microscopy techniques like conductive atomic force microscopy (C-AFM), Photoconductive AFM (PC-AFM) and Kelvin probe force microscopy (KPFM) provide an opportunity to study electrical and electronic properties with nanometer resolution. In this thesis, the application of these techniques for a variety of substrate supported and upright semiconductor nanostructures like nanowires (NW), nanodots (ND), nanosized defects and free standing nanorods (NR) is demonstrated. Using C-AFM under ultra-high vacuum (UHV) conditions, we examined samples containing InAs NWs and NDs grown on GaAs(110) substrates by molecular beam epitaxy. It has been demonstrated that in the case of the conventionally grown sample, InAs decorates step bunches running along $[1\bar{1}0]$ direction. For the case of H-assisted grown samples, InAs forms NDs at the apexes bounded by steps running along $[1\bar{1}5]$ and $[\bar{1}15]$ directions. These results demonstrate that C-AFM can be used for the exploration of III-V semiconductor nanostructures beyond the limits of conventional AFM.

Application of C-AFM to study so called arrowhead defects (ADs) in GaInP thin films epitaxially grown on vicinal Ge(100) surfaces revealed that the two terminating planes of the ADs exhibit increased conductivity compared to the defect free film. Although both terminating planes appear morphologically equivalent and are composed from $\{105\}$ and $\{109\}$ facets, they differ in their electrical behavior as is also confirmed by KPFM.

For the first time, C-AFM and PC-AFM have been applied to study the electrical properties of upright standing ZnO NRs. I-V characterization on a single NR utilizing C-AFM revealed different Schottky barrier heights for top and side planes. The obtained values agree with macroscopic data known from the literature. The PC-AFM measurements performed on single ZnO NRs exhibit the persistence of photocurrent with large decay times. The photocurrent spectroscopy performed on single NRs reveals the oxygen vacancy related defect mechanism of photoconductivity. The experimental findings stay in a good agreement with theoretical predictions from literature on the role of oxygen vacancies in the persistent photoconductivity of ZnO.

Kurzfassung

Niedrigdimensionale Halbleiternanostrukturen weisen neuartige physikalische Eigenschaften auf, welche bereits in Bauelementen wie Quantum-Well-Lasern, Transistoren mit hoher Elektronenmobilität, Solarzellen, usw. Anwendung finden. Die sich zunehmende Verringerung der Dimensionen solcher Strukturen erfordert physikalische Charakterisierung auf der Nanometerskala. Hier kommen moderne Rasterkraftmikroskopie (AFM) Methoden ins Spiel: Die auf der Verwendung leitfähiger Spitzen basierenden AFM-Techniken wie Leitfähigkeits-AFM (C-AFM), Photoleitfähigkeits-AFM (PC-AFM) und Rasterkelvinsondenmikroskopie (KPFM) ermöglichen die Untersuchung von elektrischen und elektronischen Eigenschaften mit Nanometerauflösung. In dieser Arbeit wird die Einsetzbarkeit dieser Methoden zu Untersuchung von liegenden und aufrecht stehenden Halbleiternanostrukturen wie Nanodrähten (NW), Nanopunkten (ND), Defekten und frei stehenden Nanostäben (NR) demonstriert.
Unter Verwendung von C-AFM im Ultra-Hochvakuum (UHV) wurden mittels Molekularstrahlepitaxie (MBE) hergestellte InAs NWs und NDs auf GaAs(110) Substraten untersucht. Es wurde gezeigt, dass für konventionell hergestellte Proben eine InAs Dekoration an Stufenbündeln entlang der [1$\bar{1}$0] Richtung stattfindet. Für Proben, hergestellt mittels wasserstoffunterstützter MBE, wurde die Formierung von InAs NDs an den Stellen von in [1$\bar{1}$5] und [$\bar{1}$15] Richtungen zusammenlaufenden Stufen festgestellt. Somit wurde gezeigt, dass C-AFM für die Untersuchung von III-V-Halbleiternanostrukturen jenseits der Grenzen der konventionellen AFM Methode einetzbar ist.
Der Einsatz von C-AFM zur Untersuchung sogenannter Pfeilspitzendefekte in - auf gestuften Ge(100) Oberflächen epitaktisch gewachsenen - GaInP Dünnschichten ergaben eine erhöhte Leitfähigkeit der begrenzenden Flächen der Defekte verglichen mit dem defektfreien Film. Obgleich, beide Grenzflächen morphologisch gleich erscheinen und aus {105} und {109} Facetten bestehen unterscheiden sie sich in ihren elektrischen Eigenschaften, welches auch mittels KPFM bestätigt werden konnte.
Erstmalig wurden C-AFM und PC-AFM zur Untersuchung der elektrischen Eigenschaften einzelner frei stehender ZnO NRs eingesetzt. Mittels C-AFM durchgeführte Strom-Spannungs Messungen an einzelnen ZnO NRs ergaben unterschiedliche Schottky-Barrieren für die Deck- und Seitenflächen. Die erhaltenen Werte stimmen mit makroskopisch bestimmten Daten aus der Literatur überein. Die an einzelnen ZnO NRs durchgeführte PC-AFM Messungen ergaben anhaltende Photoleitfähigkeit mit großen Zeitkonstanten. Weitere Photostromspektroskopie-Messungen lieferten Hinweise auf den auf Sauerstofffehlstellen basierenden Defektmechanismus der Photoleitfähigkeit. Die experimentellen Resultate stimmen mit theoretischen Vorhersagen aus der Literatur zur Rolle von Sauerstoffleerstellen in der anhaltenden Photoleitfähigkeit überein.

Keywords: Conductive AFM, semiconductors, electronic properties, photoconductivity, InAs, GaInP, ZnO

ACKNOWLEDGMENTS

I am thankful to my supervisor, **Prof. Dr. Christian Teichert**, whose guidance and support from the initial to the final level enabled me to develop an understanding of the subject.

Dr. Gregor Hlawacek and **Dr. Zakir Seidov** for their unselfish support and help in many administrative, everyday and scientific problems at the beginning of my stay in the group. I am indebted to my colleagues: **Dr. Markus Kratzer** for nice discussions on many scientific and everyday problems, moral support and friendship, **Dipl. Ing. Andreas Pavitschitz**, **Quan Shen**, **Astrid Wachauer** and **Lin Wang** for our joint work on conductive probe measurements; **Dr. Rainer T. Lechner** for XRD measurements and **Dr. Christian Motz** at the Erich Schmid Institut fuer Materialwissenschaft for FIB procedures; **Dipl. Ing. Stefan Lorbek** for nice time shared during repairs and maintenance of the UHV system; **Dipl. Ing. Franz Schmied** for helping in many different things and software related issues in particular.

I would like to show my gratitude to **Ms. Heide Kirchberger** and **Ms. Magdalena Ottrin** for their expertise and assistance with paperwork of every sort and kind; **Ing. Heinz Pirker** and **Mr. Peter Mocharitsch** for their help in solution of many technical problems.

Dr. Yuri P. Piryatinski for his PL measurements and help with their interpretation besides that I owe my deepest gratitude to him for the inspiration and many discussions, for his help that enabled me to start this thesis.

I am grateful to **Dr. Laurence Masson** at the Centre Interdisciplinaire de Nanoscience de Marseille CINaM, France for introducing me to STM and valuable discussions.

Prof. Dr. Antonin Fejfar and his PhD student **M.Sc. Aliaksei Vetushka** at the Institute of Physics, Academy of Sciences, Prague, Czech Republic to thank for fruitful discussion on C-AFM and PC-AFM topics.

Prof. Dr. Johannes Pedarnig at the Johannes-Kepler-Universität Linz and **Prof. Dr. Wolfgang Lang** at the Universität Wien for supplying us ion beam patterned HTSC samples for C-AFM measurements.

Dr. Aleksandra B. Djurišić, and her group at the Department of Physics, University of Hong Kong, PR China as well as **Dr. habil. Gerhard Brauer** and **Mr. Wolfgang Anwand** at the Helmholtz-Zentrum Dresden-Rossendorf, Germany for supplying us high quality ZnO NR samples and cooperative work on their investigations.

Dr. Paloma Tejedor and **Dr. Beatriz Galiana** at Instituto de Ciencia de Materiales de Madrid, CSIC, Madrid, Spain for their high quality samples and nice discussions.

Dr. Stefan Heun at the NEST, Istituto Nanoscienze-CNR and Scuola Normale Superiore, Pisa, Italy and **Dr. Giorgio Biasiol** at the TASC-INFM National Laboratory, Trieste, Italy for supplying us InAs QRs and their valuable input in the interpretation of the corresponding C-AFM data.

Dr. Andrei K. Kadashchuk at the Institute of Physics, Academy of Science, Kiev, Ukraine for his willingness to help people, profound and valuable discussions based on his great scientific and life experience.

Last but not the least, I would like to thank to my family and especially to my wife **Lena** for her support and love.

Many thanks to Austrian Science Fund (**FWF**) for financial support of this thesis within the project "Nanoscale electrical properties of phase-separated thin films", project number: P19636-N20 and Austrian Academic Exchange Service (**ÖAD**) for travel support.

Contents

Table of Contents **ix**

1 Introduction **1**
1.1 Semiconductor nanostructures for electric and photoelectric applications . . 1
1.2 Atomic Force Microscopy based techniques for electrical characterization on the nanometer scale 3

2 Experimental: Conductive probe based AFM techniques **5**
2.1 Conductive Atomic Force Microscopy 5
2.1.1 Technical implementation 5
2.1.2 Possible mechanisms of electrical transport 8
2.2 Kelvin probe force microscopy 13
2.2.1 Contact potential difference mapping in UHV 16
2.2.2 Photo-assisted Kelvin probe force microscopy 17
2.3 Photoconductive AFM 18
2.3.1 Light absorption in semiconductors 19
2.3.2 Technical implementation 21

3 Results I: Supported InAs nanostructures on GaAs substrates **27**
3.1 InAs nanowires (NWs) and nanodots (NDs) on self-organized GaAs(110) . . 27
3.1.1 Sample preparation: Conventional and H-assisted epitaxial growth . . 28
3.1.2 Investigation of InAs NW and ND formation by means of C-AFM . . 29
3.1.3 I-V Characterization 34
3.2 InAs quantum rings on GaAs(100) 36
3.2.1 Sample preparation 36
3.2.2 Removal of the protecting As_4 layer in UHV 37
3.2.3 Topography characterization of quantum rings 38
3.2.4 C-AFM characterization 39

4 Results II: Electrical properties of defects in GaInP epitaxial layers on Ge **47**
4.1 Sample preparation: MOVPE growth 48
4.2 Structural properties of GaInP layers 48

4.3 Electrical properties of the arrowhead defects . . . 49
4.3.1 C-AFM study . . . 49
4.3.2 KPFM study . . . 50
4.3.3 Analysis and discussion of the obtained results . . . 52

5 Results III: ZnO nanorods **55**
5.1 Synthesis of ZnO NRs . . . 56
5.2 Characterization of the morphology . . . 56
5.2.1 Structural characterization . . . 57
5.3 Time-resolved photoluminescence spectroscopy . . . 59
5.4 Electrical characterization by means of C-AFM . . . 61
5.4.1 2D current maps . . . 62
5.4.2 Current line profiles . . . 66
5.4.3 Local I-V characterization . . . 66
5.4.4 Analysis of the dark conductivity . . . 69
5.4.5 Remarks on the local electrical characterization of ZnO NRs by C-AFM 71
5.5 Electrical characterization by means of PC-AFM . . . 72
5.5.1 I-V characterization under illumination . . . 73
5.5.2 Transient photocurrent . . . 74
5.5.3 Photocurrent spectroscopy . . . 76

6 Results IV: Application of C-AFM to the electrical characterization of high-temperature superconductors **81**
6.1 Sample preparation . . . 81
6.2 C-AFM characterization ion beam patterned HTSC films . . . 82

7 Conclusions and Outlook **85**

List of Figures **89**

List of Publications **95**

Bibliography **96**

List of Acronyms **107**

Chapter 1

Introduction

1.1 Semiconductor nanostructures for electric and photoelectric applications

Recent advances in the epitaxial growth of semiconductor nanostructures with techniques such as Molecular Beam Epitaxy (MBE), make it possible to form self-assembled nanostructures of various geometries and dimensions. As a semiconductor structure shrinks in dimensions down to the nanometer scale, distinct deviation from the bulk material properties is expected. This paradigm is considered as a basis for future generations of electronic devices. It is already partially employed in devices like quantum well lasers, high electron mobility transistors, etc. The range of semiconductor materials used in modern devices is tremendous. The application range for each certain semiconductor material can be rather broad as well, however, the electronic structure of the material determines its preferential field of utilization. The materials predominantly investigated in the present work, namely InGaAs, InGaP, and ZnO are direct band gap semiconductors usually used in optoelectronic devices.

InAs/GaAs

The InAs material system is of particular interest for studies because of its high electron mobility and resulting potential for high-performance devices. Several important advantages like low band gap and strong spin-orbit coupling make InAs attractive for the production of semiconductor devices. This material is used in photo-detectors for the near IR region and lasers operating at room temperature. Recently, an enhancement of the spin relaxation time by more than one order of magnitude in InAs(110) in comparison to the corresponding (001) structures has been predicted [1, 2]. This fact makes InAs a good candidate for high-speed spintronic application. Usage of InAs low-dimensional structures, in turn, extends the possibilities for tuning the aforementioned properties and device production.

The most appropriate substrate for the growth of InAs is GaAs due to the small lattice

mismatch between these two materials on the one hand and attractive electronic properties of their interface on the other hand. Also very important is that - depending on the growth conditions - one can fabricate structures of desirable dimension, like Nanodots (NDs), Nanowires (NWs), superlattices, etc.

Recently, much attention has also been dedicated to torus-volcano shaped Quantum Rings (QRs) [3], which are formed when QDs are capped under appropriate conditions with a few nanometers of the substrate material, followed by an annealing step at the growth temperature [4]. Just like self-assembled QDs, QRs possess atom-like properties [5], making them candidates for future device applications in opto-electronics and quantum computing. On the other hand, their ring topology allows the observation of quantum-interference phenomena like the AharonovBohm effect [6]. While common characterization techniques such as photoluminescence and capacitance spectroscopy are useful for probing ensembles of QDs and QRs [7], scanning probe microscopy techniques become more advantageous when individual QDs and QRs are to be investigated [8]. Our research focuses on InAs/GaAs QRs studied by Conductive Atomic Force Microscopy (C-AFM).

GaInP/Ge

Stacked layers of epitaxially grown semiconductor materials are commonly used in multi-junction solar cells. They are employed to optimize the absorption range, gaining, in turn, the overall efficiency of solar energy conversion. A further advantage is the possibility to use relatively cheap substrates (e.g. Si or Ge) for production. The most common materials used as III-V nucleation layers on Ge are GaAs and GaInP. In order to achieve a shallow junction on Ge, which implies a better photocurrent response, the use of P as n-type dopant is preferred. Consequently, the study of the heteroepitaxial GaInP/Ge is an up-to-date topic, especially for solar cell applications. Furthermore, as a result of its low bandgap (0.67 eV), Ge is a suitable candidate to be used also as the bottom junction in tandem solar cells, which is formed by diffusion of the group-V element used in the nucleation layer into the p-type germanium. More precisely, GaInP/GaAs/Ge triple-junction solar cells have been demonstrated to attain record efficiencies of 40.7% at 236 suns [9]. In these devices, the Ge third junction is an important part of the structure of this complex solar cell, contributing around 15% (relative) to the total cell efficiency.

ZnO

A variety of physical properties [10, 11] of ZnO provides reason enough to investigate this material from different aspects. A distinguishing feature of the ZnO is the ability to form a spectrum of morphologies on the nano- and meso- scales which are of prospects to become functional. Having a wide bandgap (3.37 eV at room temeperature), high exciton binding energy (60 meV) and being piezoelectric, ZnO is one of the most promising semiconductor materials.

ZnO nanorod arrays have been of interest for applications in a variety of optoelectronic devices [11] and solar cells. For example, ZnO nanowire arrays have been utilized in dye-sensitized solar cells [12–14]. It has been demonstrated that the electron transport in a nanowire array electrode is more efficient compared to a conventional nanoparticle porous film electrode [12]. Thus, the study of electronic properties and charge transport in ZnO nanorod/nanowire arrays is of considerable interest for their practical applications. The applications mentioned above require a detailed insight into the electrical properties of the ZnO nanorods. Consequently, ZnO NRs have been the subject of active studies by means of C-AFM including experiments with applied mechanical stress [10, 15–19]. This technique is promising for the characterization of as-grown nanostructures and provides access to the electrical properties on the nanoscale.

The scope of this work is to explore the electrical properties of semiconductor nanostructures, so that we can better understand the relation between the morphological peculiarities and material parameters on one hand and the resulting electrical characteristics on the other hand.

1.2 Atomic Force Microscopy based techniques for electrical characterization on the nanometer scale

Surface science and nano technology have both grown rapidly in the past decades, and are still among the most active fields of research. Simultaneously, the semiconductor technology was significantly enhanced by account of the implementation of novel approaches which rely on the application of surface properties. The need for electrical characterization of surfaces on the nanometer scale has led to a rapid development of a variety of scanning probe microscopy based techniques. Among these techniques are C-AFM [20], Scanning Capacitance Microscopy (SCM) [21, 22], Photoconductive AFM (PC-AFM) [23, 24], Kelvin Probe Force Microscopy (KPFM) [25] and Piezoresponse Force Microscopy (PFM) [26] which utilize a conductive probe during the measurement process.

C-AFM has been developed in the mid 1990's for local electrical characterization of thin silicon gate dielectrics on the nanometer scale [27–29]. The possibility to simultaneously record the topography and current signals between tip and sample as a function of the applied bias has been used to study the processes of electrical breakdown in thin SiO_2 films. C-AFM enables one to detect currents as low as several tens of femtoamperes. Therefore, this technique is sufficiently sensitive to detect small variations in the local conductivity of the sample surface. Originally exclusively applied to characterize SiO_2 films, C-AFM has been more recently successfully applied to study so called high-k dielectric thin films [30–33]. Further, recent applications include conductivity measurements on phase separated semiconductor films [34, 35] and free standing nanorods [36] as well as electrical characterization of electroceramic devices [37].

Despite the success achieved in the field of the Scanning Spreading Resistance Microscopy (SSRM) for doping profiling with excellent concentration sensitivity and determination of

junction position with high spatial resolution [38], it remains difficult to measure structures with the size on the order of several nanometers in one of their dimensions. Another issue is the lateral resolution which drops when the contact area is increasing. Reducing the loading force below 10-20 nN - using soft cantilevers - improves the lateral resolution and one can get access to the local variation of the contact resistance. This force regime is also suitable in most of the cases for the estimation of the Schottky barrier height, leaving the contact undamaged and relatively well defined. Thus, the difference in material's properties can be resolved at low loading forces in C-AFM.

The KPFM which is also sometimes called scanning Kelvin force microscopy (SKPM) allows the detection of tip-surface Contact Potential Difference (CPD). The KPFM technique has been proposed in 1991 by Nonnenmacher et al. [25]. It has been demonstrated that the technique possesses a high resolution for both, the contact potential difference (better than 0.1 mV) and the lateral dimension (< 50 nm). The CPD maps - which are representative of work function distribution across the surface - can be collected simultaneously to the topography. The information about the local variation of the CPD derived by the KPFM method together with data obtained by means of C-AFM can be successfully employed to determine the influence of the local surface work function on the local transport properties. This knowledge of local CPD helps to explain local I-V characteristics and 2D current maps recorded using C-AFM as well as to make easier quantitative analysis of the obtained C-AFM data. Another very similar technique, namely Electrostatic Force Microscopy (EFM) which probes the distribution of electrostatic forces allows in some cases a simple qualitative analysis of charge distribution at/under the surface. With the help of this technique one can also study charging processes in metal and semiconductor nanoclusters embedded in an isolating matrix [39].

Investigation of photoelectric properties of organic thin films resulted in the development of PC-AFM [23, 24]. In fact, the PC-AFM similar to C-AFM, (details will be explained in a corresponding experimental section) employs a conductive probe to measure 2D current maps. In addition, the PC-AFM setup is extended with the illumination system and is capable to help in studying an light interaction with the surface (bulk contribution should be also considered in the case when light penetration depth is high). As will be discussed in Sec. 2.3 the PC-AFM method can be used to gain insight into the local electronic structure of the material under investigation. The method is sensitive to the variation of the band gap width and presence of defect energy levels inside the band gap. The local electronic structure can be analyzed with the help of photocurrent spectroscopy. Additional information about the photogenerated carriers kinetics can be gained via studying the transient behavior of the photocurrent.

Chapter 2

Experimental: Conductive probe based AFM techniques

The chapter is partially based on Ref. [2] from the publications list.

2.1 Conductive Atomic Force Microscopy

2.1.1 Technical implementation

The C-AFM is a conventional AFM operating in a contact regime utilizing a conductive cantilever and tip [40, 41]. Fig. 2.1 presents a principle scheme of the C-AFM set-up. Besides conventional AFM's scanner and cantilever detection technique, the set-up employs a conductive AFM probe, an external voltage source and a current amplifier connected to the AFM tip. The voltage is applied between the conductive AFM tip and the sample to obtain the desired electrical information. The resulting current is measured using a highly sensitive amplifier as a current-to-voltage converter. The amplification is especially important for samples with high resistance or even isolating behavior, where the measured currents can be as low as several femto- to picoamperes. The C-AFM technique bears a striking resemblance to Scanning Tunneling Microscopy (STM) using similar technical solutions for the current signal acquisition. However, there is a fundamental difference in the operational principle. In contrast to STM, the conductive AFM measures the current signal completely independent from the topography which is simultaneously recorded via the cantilever deflection. In order to obtain a potential drop and current across the sample, the external bias is applied to the sample. (In principle, tip biasing is also possible but rarely used.) It is also worth to notice that the contact to the sample should be preferentially ohmic, otherwise the influence of the additional barrier has to be considered carefully. The commonly used range of the applied voltage is ± 10 V. The application of higher voltages is possible using external voltage sources, though additional circuit protection should be implemented.

The current signal is amplified and converted to a voltage signal either by an electrometer

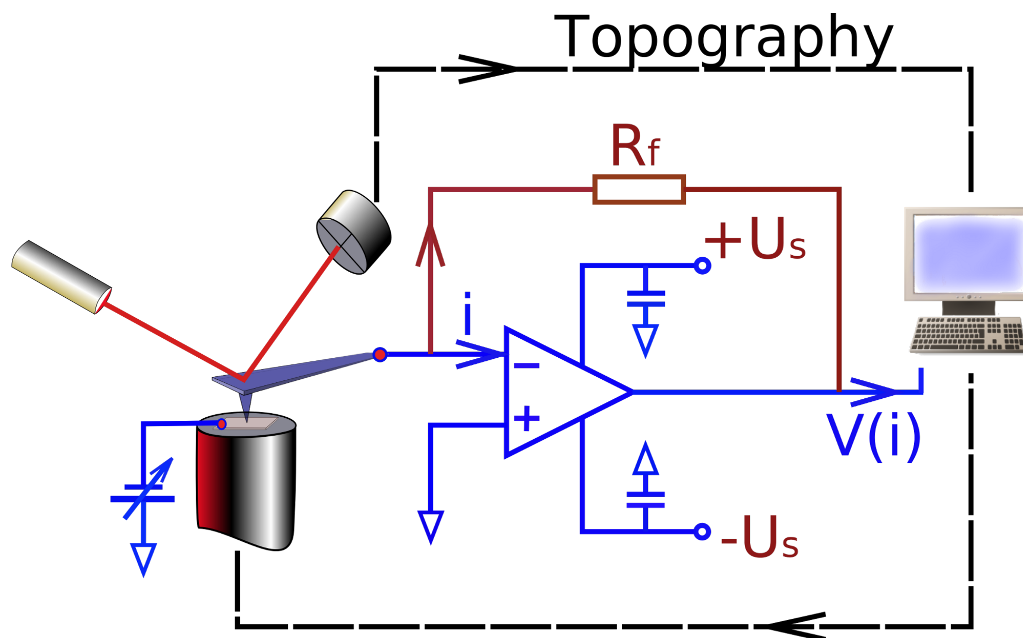

Figure 2.1 Schematic drawing of the C-AFM setup.

or logarithmic amplifier, depending on the desired range of current magnitude. The main difference between these two amplifiers is a feedback loop. In the case of the electrometer, the feedback loop is performed using a feedback resistor R_f, (see Fig. 2.1), whereas a logarithmic amplifier utilizes a nonlinear element (diode) for this purpose. The voltage signal is more convenient to deal with, since it can be easily converted to a digital form using an Analog-to-Digital Converter (ADC). Usually, the AFM electronics provides several voltage input/output channels equipped with high-resolution ADC's, which are appropriate for both, the current signal acquisition and sample biasing. For the materials under investigation, the currents to be detected will cover a range from fA (tunneling current throughout oxides) to mA for semiconducting or conducting materials. Over the last decade, several commercial solutions have been elaborated which exploit one of the above mentioned approaches. A system based on Operational Amplifier (OA) is usually able to detect lower currents (down to tens of fA) [28] with small noise levels, while systems based on logarithmic amplifiers overlap a wider range of currents (1 pA - 1 mA) [42, 43]. However, the use of logarithmic amplifiers restricts the operational mode to a single voltage operation in most of the cases.

Low-noise, high-precision operational amplifiers with inputs based on isolated field effect transistors are widely used in commercial and home-built systems as a main component. Fig. 2.1 presents a simple electrometer scheme built on the basis of such an amplifier. This setup is usually able to measure currents down to a few tenth of femtoamps when properly assembled. In principle, this scheme is a current-to-voltage converter with the simple conversion law $U_{out} = I_{inp} \cdot R_f$. Although having superior sensitivity as well as low inherent noise, the scheme requires the solution of several problems related to the design and assembly of

current-to-voltage converters for Direct Current (DC) amplification. The noise induction and electrical leaks should be carefully analyzed and suppressed if possible. Among possible solutions are the isolation of the inputs of the operational amplifier from the printed circuit board and minimization of the current paths. It has to be mentioned that the amplifier should be placed in close proximity to the AFM tip in order to avoid pick up of noise.

The input offset voltage of the utilized OA has also to be taken into account during design of the amplifier. The presence of small voltages at the input of the OA is unfortunately practically almost unavoidable. Optimally, the value of the offset voltage should not exceed 1-2 mV. For the best performance it should be 0.5 mV or less, since even a small offset voltage may account for the appearance of significant currents at the output even when the sample is grounded. Parameters, like voltage noise, drift, and power-supply rejection should also be considered. There are several commercially available high precision OA that meet the above mentioned demands. One of those, namely OPA129 is utilized in a home-built C-AFM setup for measurements under ambient conditions [44]. The noise level of the amplifier finally achieved is about 50 fA, the input offset voltage does not exceed 1 mV.

Commercially available setups for C-AFM are usually operating in air. However, one gains several advantages of performing the C-AFM experiments under Ultra High Vacuum (UHV) conditions. First of all, the presence of the water film in the ambient can be easily avoided in vacuum by annealing at low temperatures prior to the measurement. Second, when applying positive sample bias, the oxide layer formation and anodic oxidation processes are excluded [28]. (In air this leads to water dissociation [45].) A comparative study of C-AFM measurements performed under ambient and UHV conditions is given in Ref. [43].

A UHV implementation of the C-AFM setup is in fact only little different from the one used in the ambient with the one difficulty to place the OA close to the AFM tip, i.e. into UHV. The UHV set-up used for the C-AFM measurements is based on a combined Omicron AFM/STM system operating at room temperature equipped with Anfatec controller and modified current pre-amplifier [28]. The system has also been equipped with a high voltage unit which extends the applicable voltage range from ±10 V up to ±150 V. The amplification factor was set to 10^8 V/A for the input amplification stage and can be additionally increased by a factor of 2 or 20 at the second amplification stage. The resulting noise level in the system is approximately 0.2 pA. In order to have more flexibility in data acquisition and analysis, the system has been supplemented with a data acquisition module (National Instruments) and LabView software. Particular attention during C-AFM experiments has to be paid to the contact properties which depend to a large extent on the tip conditions. Although any conductive AFM probe, e. g., conventional doped silicon probes, can be used in C-AFM, probes with conductive, wear resistive coatings are favored. The reason is the high stability of the tip geometry and its electrical properties. There are several types of commercially available conductive probes designed especially for C-AFM. These are conventional AFM probes for contact mode with one of the following coatings: heavily doped diamond, PtIr, TiN, W_2C, and Au. The best results are usually obtained with diamond coated tips. There are two types of diamond coated C-AFM probes on the market, one is heavily boron doped (p-type) and another one is heavily nitrogen doped (n-type) [46]. The

Coating	Pt [48]	Au [48]	W_2C [49]	PtIr [50]	Diamond [51]	TiN [52]
Work function (eV)	5.65	5.10	4.7-4.8	5.6	5.7	4.8-5.3

Table 2.1 Work functions of materials used as conductive coatings in C-AFM probes

doping is so high that the Fermi level is shifted into the valance or the conduction band of the diamond, respectively. Thus the tip can be assumed as metallic. The resulting resistivity of the diamond coating is normally about 0.5-1 Ω·cm. Despite the fact that the metal coatings like Au or PtIr have lower resistivity (0.01-0.025 Ω·cm), their lifetime is low compared to the diamond coated ones since the soft coating is worn much faster. The typical curvature radius of probes with metal coating is about 35 nm, whereas for the diamond coated ones it can be more than 100 nm, resulting in lower resolution on rough surfaces. However, the diamond coatings exhibit a nanoroughness in the 10 nm regime which leads to excellent resolution on flat surfaces. Recently, conductive probes fabricated entirely of diamond have become commercially available (NaDiaProbe from nanoScience Instruments). They are manufactured entirely from electrically conductive Ultrananocrystalline Diamond (UNCD) [47] with a resistivity less than 1 Ω·cm, therefore problems caused by coating damage are no longer present. One additional advantage of the coated and entirely diamond probes is the low adhesion and low surface energy of diamond, which helps to avoid tip contamination and thus yields reproducible contrast during current imaging. Another important parameter is the work function of the coating which has influence on the type of the tip-to-sample electrical contact and barrier height in the case of barrier formation. The work functions for several materials used as C-AFM tip coatings are summarized in Tab. 2.1.

An evaluation of probes for AFM electrical modes can be found in Ref. [53]. The search for an appropriate probe is a kind of compromise between desired resolution and probe life time. From a practical point of view it is always useful to check several probes and choose the one with the best performance since optimal conditions may vary significantly for different materials and surface morphologies.

2.1.2 Possible mechanisms of electrical transport

As it was described above, the C-AFM technique provides an opportunity to investigate local electrical properties at the nanoscale. For the analysis of the obtained data, however, it may be rather complicated to define the mechanism of electrical transport in each certain case. Nevertheless, we can arbitrarily distinguish several main mechanism which may contribute to the current via the tip-to-sample interface:

- Diffusion
- Thermionic emission
- Direct and Fowler-Nordheim tunneling

- Poole-Frenkel emission

Diffusion

Diffusion transport occurs when there is a gradient of carrier concentration. Then, the carriers diffuse from the region of high concentration toward the region of low concentration until the system is in the state of equilibrium. Conditions which cause a gradient of carrier concentration may be different: gradient of temperature, nonuniform illumination, local injection of carriers from a junction, etc. The diffusion current densities for electrons and holes, respectively, are given by:

$$J_n = qD_n \frac{d\Delta n}{dx} \tag{2.1}$$

$$J_p = -qD_p \frac{d\Delta p}{dx} \tag{2.2}$$

where q is the elementary charge, D_n and D_p are diffusion coefficients for electron and holes, respectively. Δn and Δp are the incremental carrier densities defined as $\Delta n = \tau_e G_e$ and $\Delta p = \tau_h G_h$, where $\tau_{e,h}$ are the carrier's lifetime and $G_{e,h}$ are generation rates for the electron and holes, respectively.

The important relationship between the diffusion coefficients and charge carrier mobilities is given by the Einstein relation (see details in Ref. [54]):

$$D_n = \left(\frac{k_B T}{q}\right) \mu_n \tag{2.3}$$

$$D_p = \left(\frac{k_B T}{q}\right) \mu_p \tag{2.4}$$

It is worth to mention that the Einstein Relation (ER) can be measured using KPFM [55], whereas carrier mobilities in some cases (space charge limited current transport) can be obtained from C-AFM experiments [56]. In Ref. [55] the ER was measured as a function of charge concentration in doped and undoped disordered organic thin films. It has been demonstrated that the ER significantly deviates from $k_B T/q$ and is sensitive to changes in the Density of States (DOS).

Thermionic emission

The thermionic emission phenomenon is associated with the current of the majority carriers in the presence of a potential barrier (such as a Schottky barrier). In C-AFM, the potential barrier is usually formed at the tip-to-sample interface as a result of the Fermi level alignment between tip and sample when they are brought into contact. The total thermionic electron current density over the barrier is given by:

$$J = A^* T^2 \exp\left(-\frac{q\Phi_b}{k_B T}\right) \tag{2.5}$$

where A^* is the effective Richardson constant, k_b is the Boltzmann constant, T is the temperature and Φ_b is the barrier height. The Richardson constant can be defined in a simplified way as:

$$A^* \equiv \frac{4\pi q m^* k_B^2}{h^3} \tag{2.6}$$

where m^* is the effective mass of the charge carrier and h is the Planck's constant.

Direct and Fowler-Nordheim tunneling

Tunneling is a purely quantum-mechanical phenomenon which consists in the ability of electrons to penetrate into and through an energy barrier of finite height and width. The direct tunneling is the main mechanism responsible for the formation of the contrast in STM, whereas in C-AFM it contributes to the formation of the contrast in current maps. The tunneling current density is given by:

$$J_{tun} = \frac{qm^*}{2\pi^2\hbar^3}\int F_A N_A T_t (1 - F_B) N_B \, dE \tag{2.7}$$

where where F_A, F_B, N_A, and N_B represent the Fermi-Dirac distributions and densities of states in the corresponding regions before and after the barrier. T_t is the tunneling probability which can be calculated by:

$$T_t \simeq \exp\left\{-2\int_{x_1}^{x_2}\sqrt{\frac{2m^*}{\hbar^2}[U(x) - E]}\, dx\right\} \tag{2.8}$$

where E is the electron energy and $U(x)$ defines the potential barrier height and shape.

Fowler-Nordheim Tunneling (F-N) tunneling is associated with the tunneling through a thin layer of insulator and considered as the main transport mechanism in thin insulating films of SiO_2, HfO_2 and Al_2O_3. In C-AFM experiments it is necessary to distinguish between the direct and F-N tunneling regimes. F-N is characterized by two distinguishing properties: the barrier has a triangular shape, and tunneling occurs only through a part of the insulator layer.

Both, direct and F-N mechanism are contributing usually to a higher or lesser extent depending on the conductivity of the substrate, tip geometry and applied electrical field. In the presence of a surface oxide layer the main contribution is determined by the thickness of the oxide layer. Direct tunneling occurs when the thickness of the oxide layer is below ~5 nm, for thicknesses above this value F-N mechanism commonly is considered as dominant [57]. The F-N current density is given by [58, 59]:

$$J_{F-N} = \frac{q^2\mathcal{E}^2}{16\pi^2\hbar\phi_{ox}}\exp\left[\frac{-4\sqrt{2m^*}(q\phi_{ox})^{1.5}}{3\hbar q\mathcal{E}}\right] \tag{2.9}$$

where ϕ_{ox} is the barrier height associated with the presence of the oxide layer, m^* is the effective mass of the electron and $\mathcal{E}$ is the electric field applied across the oxide.

It may also appear appropriate in some cases to approximate the tip-to-sample interface of semiconductor surfaces by a Metal-Insulator-Semiconductor (MIS) structure if the surface of the measured semiconductor is covered with a thin oxide layer. The current density in this case can be defined as:

$$J_{MIS} = A^{*}T^{2} \exp\left(-\alpha_T d\sqrt{q\phi_T}\right) \exp\left(\frac{-q\phi_B}{k_B T}\right) \left[\exp\left(\frac{qV}{\eta k_B T}\right) - 1\right] \tag{2.10}$$

where ϕ_B and ϕ_T are the Schottky and tunneling barrier heights, d is the oxide thickness and V is the voltage applied.

It is important to note that the F-N tunneling mechanism implies that electrons are free to move through the oxide layer. Such an assumption is valid for the thermally grown silicon oxide, but is inappropriate for deposited insulators where the density of structural defects is high. The localized trap states - appearing as a result of structural imperfection - restrict the current flow and cause a deviation from the F-N mechanism. The existence of the trap states in the band gap, however, makes the Poole-Frenkel mechanism workable.

Poole-Frenkel mechanism

Poole-Frenkel Emission (P-F) occurs due to emission of trapped electrons into the conduction band. At low voltage and high temperature, current is carried by thermally excited electrons hopping from one isolated state to the next. This mechanism yields an ohmic characteristic exponentially dependent on temperature. It can be used to describe electrical transport in insulators at elevated temperatures and high electric fields. The current density for the P-F mechanism is defined as:

$$J_{P-F} = qn_0\mu\mathcal{E} \exp\left[\frac{-q}{k_B T}\left(\phi_B - \sqrt{\frac{q\mathcal{E}}{\pi\varepsilon}}\right)\right] \tag{2.11}$$

where μ is the carrier mobility, $\mathcal{E}$ is the electric field applied across the insulator, n_0 is the charge carrier density and ε is permittivity. It has been demonstrated recently that the P-F model can be applied successfully to explain the data obtained by means of C-AFM on nitrides [60].

Space charge limited currents

The carrier concentrations in semiconductors or insulators can be significantly increased beyond their values in equilibrium by carrier injection. The injected carriers in this case control the space charge and spatial distribution of the electric field within the semiconductor. The current dominated by the drift component of the injected carriers is called the space Space Charge Limited Current (SCLC). This results in a feedback mechanism where the field drives the current, which in turn builds up the field. There are three possible regimes for SCLC [54]:

1. Mobility regime, described by the Mott-Gurney law [61]:

$$J_m = \frac{9\varepsilon\mu V^2}{8L^3} \tag{2.12}$$

where L is the distance that the charge carrier should move across before being collected at the electrode (back electrode or C-AFM tip depending on the direction of the current flow) and V is the voltage applied.

2. Velocity-saturation regime, where the velocity of the charge carriers reaches its saturation and does not depend on the applied field anymore, described as:

$$J_{vs} = \frac{2\varepsilon v V}{L^2} \tag{2.13}$$

where v is the charge carrier velocity.

3. Ballistic regime, occurs in the absence of scattering, described by the Child-Langmuir law [62]:

$$J_B = \frac{4\varepsilon}{9L^2}\sqrt{\frac{2q}{m^*}}V^{1.5} \tag{2.14}$$

The SCLC model is widely used to fit I-V characteristics measured on organic materials. However, the current density measured with C-AFM is substantially higher than the ones measured in planar devices at the same bias. This leads in turn to an overestimation of carrier mobilities when using the Mott-Gurney law. Reasonable values of mobilities can be obtained using semi-empirical scaling factor based on the ratio of the diameter of the tip contact area to the sample thickness. A semi-empirical expression for the current density measured in C-AFM is [56]:

$$J_{CAFM} = \alpha\varepsilon\varepsilon_0\mu_0 \exp\left[0.89\gamma\sqrt{V/L}\right]\frac{V^2}{L^3}\delta\left(\frac{L}{d}\right)^{1.6\pm0.1} \tag{2.15}$$

where α is the prefactor determined from numerical calculations [56] to have a value of $\sim$8.2 (instead of 9/8 from the Mott-Gurney law), δ is an empirical dimensionless parameter equal to 7.8$\pm$1, d is the estimated diameter of the tip-to-surface contact area, γ expresses the apparent field dependence of the mobility (e.g. $\gamma = 0$ for P3HT), L is the active layer thickness, V is the voltage applied across the active layer.

2.2 Kelvin probe force microscopy

The Kelvin probe method has been developed by the Scottish scientist Lord Kelvin in 1861. It is a non-contact, non-destructive measurement tool used to investigate the work functions of various materials. In fact, the technique is sensitive to the CPD, Φ_{CPD}, between the exposed surfaces of two samples of interest. The conventional Kelvin probe setups employ mm-scale electrodes and can not be utilized for the characterization of the surfaces on the nanometer scale.

As an alternative, KPFM, also called Scanning Surface Potential Microscopy has been proposed in 1991 by Nonnenmacher et al. [25]. It has been demonstrated that the technique possesses a high resolution for both, the contact potential difference (better than 0.1 mV) and the lateral dimension (< 50 nm). The CPD maps - which are representative of work function distribution across the surface - can be collected simultaneously to the topography. The KPFM is a derivative of AFM which operates in intermittent contact mode [25]. Conventional Kelvin probe and KPFM techniques are very similar conceptually, but differ in the way they measure CPD. The conventional Kelvin probe measures displacement currents while the KPFM relies on nullification of tip-to-sample electrostatic forces. The KPFM setup is schematically depicted in Fig. 2.2.

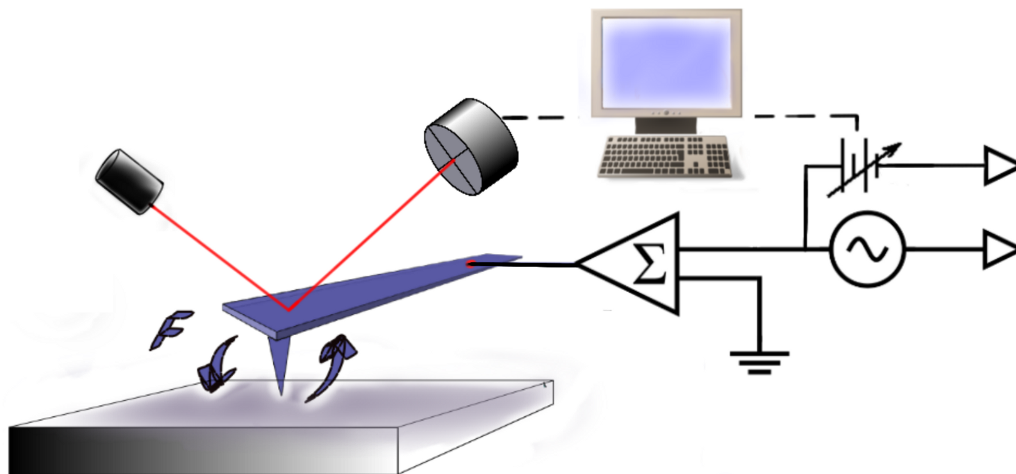

Figure 2.2 Schematic drawing of the Kelvin probe force microscopy (KPFM) setup.

As it has been mentioned above, the KPFM setup measures - or it is more correct to say - steadily compensates the electrostatic interaction between the probe and sample. In fact, the KPFM setup can be realized in a way similar or exactly the same compared to the conventional Kelvin probe method. In this case one would need to modulate the tip-to-sample spacing $d = d_0 \sin(\omega t)$ and to measure (or nullify by active feedback) the displacement current which is given by:

$$I = \frac{dQ}{dt} = \frac{dC}{dt}[-(\Phi_S - \Phi_{tip}) + U_{comp}] \tag{2.16}$$

where Q is the net charge, Φ_S and Φ_{tip} are the work functions of the sample and tip respectively, U_{comp} is the voltage applied to compensate the work function difference, and C is the net capacitance. However, this current can be as small as several pico-amperes or even smaller. Thus, a very sensitive, high-impedance amplifier is needed.

Instead of measuring currents, the KPFM principle of operation relies on the measurements of the electrostatic forces between the conductive AFM probe and the metal or semiconductor surface. This force appears due to the difference in work functions of the tip and sample and can be nullified by applying a proper DC voltage to the tip or sample. The electrostatic force is given by:

$$F = \frac{1}{2}(U_{CPD})^2 \frac{dC}{dz} \tag{2.17}$$

where z is the tip-to-sample distance, U_{CPD} is the contact potential difference and C is the tip-to-sample capacitance. In order to increase the sensitivity of the measurement, the tip-to-sample electrostatic interaction is modulated by applying an AC voltage (U_{AC}) to the tip or sample. The modulated force response is detected thereafter using lock-in technique. Therefore, Eq. 2.17 can be split into three terms:

$$F = F_0 + F_\omega + F_{2\omega} \tag{2.18}$$

$$F_0 = \frac{1}{2}\left((U_{CPD} + U_{comp})^2 + \frac{U_{AC}^2}{2}\right)\frac{dC}{dz} \tag{2.19}$$

$$F_\omega = (U_{CPD} + U_{comp})U_{AC}\sin(\omega t)\frac{dC}{dz} \tag{2.20}$$

$$F_{2\omega} = \frac{1}{4}U_{AC}^2\cos(2\omega t)\frac{dC}{dz} \tag{2.21}$$

where F_0, F_ω and $F_{2\omega}$ are the zero, first, and second order harmonic force responses, U_{AC} is the amplitude of the AC voltage applied to the tip at frequency ω. The conventional realization of the KPFM setup is a two-pass AFM technique. The surface topography is recorded during the first pass along a scan line and is then used to keep a constant tip-to-sample separation at the level of 10-100 nm during the second pass along the same scan line. The amplitudes of the cantilever's oscillations during the second pass at ω and 2ω frequencies are proportional to the corresponding force components and can be monitored during AFM operation. The response is monitored using lock-in amplifiers connected to the output of the AFM photodiode which detects the cantilever's oscillation. Typically, the response at frequency ω is used for CPD maps acquisition, the AFM electronics is trying to nullify the response at this frequency by adjusting U_{comp}. At the same time, the response on frequency 2ω can be used for the tip-to-sample capacitance monitoring.

It is worthwhile to mention that the cantilever-to-sample capacitance plays also an important role in the CPD measurement. At high tip-to-sample separation this contribution may appear very significant and may even hinder local changes of the surface work function. Therefore, it is important to take the cantilever-to-sample capacitance into account. Its

derivative vs. distance is given by [63]:

$$\frac{\partial C_{cant}}{\partial z} = \epsilon_0 \frac{wL \sin\varphi}{\varphi(h_t + z + L\sin\varphi)(h_t + z)} \tag{2.22}$$

where L and w are the length and width of the cantilever respectively, φ is the angle of inclination of the cantilever relative to the sample, h_t is the tip's height and ϵ_0 is the dielectric constant of free space. The tip-to-sample capacitance derivative vs. distance is given by [63]:

$$\frac{\partial C_{tip}}{\partial z} = 2\pi\epsilon_0 \frac{r_t}{z} \tag{2.23}$$

For a better visualization these two contributions are plotted in Fig. 2.23 simultaneously using the following parameters:

cantilever's length: $L = 125$ μm
cantilever's width: $w = 35$ μm
tip height: $h_t = 15$ μm
tip radius: $r_t = 40$ nm
tip inclination angle: $\varphi = 10°$

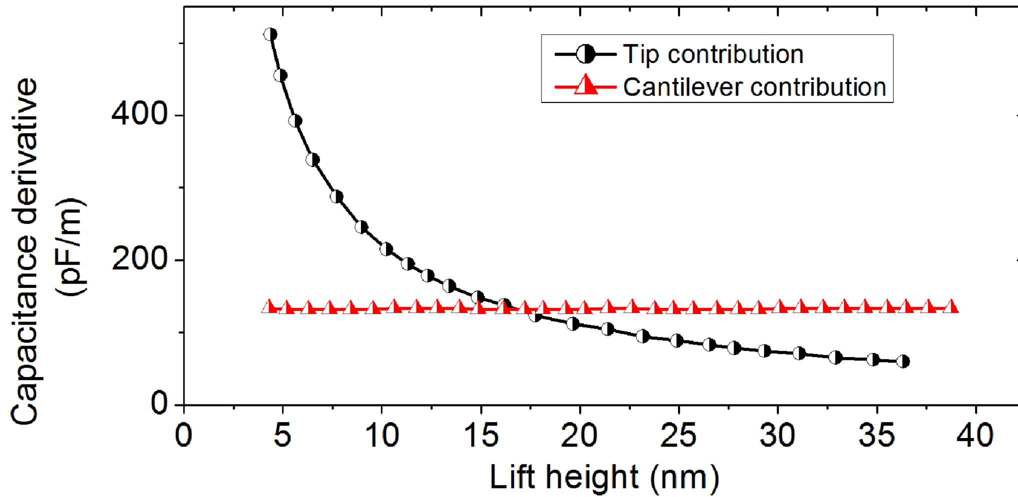

Figure 2.3 The tip and cantilever derivative contributions are plotted simultaneously. The tip contribution becomes "visible" at the tip-to-sample separation equal to 15 nm or less for a given set of parameters. (example is taken from [63])

Another resolution limiting factor is the thermal noise of the cantilever, the minumum detectable value of CPD by KPFM is given by [63]:

$$\Delta\Phi_{min} = \frac{1}{\epsilon_0 U_{AC}} \frac{z}{r_t} \sqrt{\frac{K_B T k B}{\pi^3 Q f_o}} \tag{2.24}$$

where U_{AC} is the AC voltage applied to the tip, K_B is the Boltzmann constant, T is the temperature, B is the electronics bandwidth, Q is the quality factor and k is the spring constant of the cantilever.

An important problem of KPFM imaging is also the stability of the tip coating. A majority of commercially available tip coatings is listed in Tab. 2.1. As it has been demonstrated in [64], the components of the metal coating can become detached during scanning, introducing sudden offset jumps in the potential maps typically up to 350 mV between adjacent scan lines. In UHV, however, one can use non coated heavily doped silicon probes. Prior to measurements they should be cleaned in-situ, in order to remove the native oxide layer.

2.2.1 Contact potential difference mapping in UHV

The commercial Kelvin probe setup for macroscopic characterization usually operates under high vacuum or UHV conditions. The operation in UHV has significant advantages to the measurements performed under ambient conditions. It has been shown that for KPFM in air, where large tip-to-sample distances are required due to the water film on the sample surface, the variations in CPD are very hard to resolve [65]. In UHV, the presence of the water film and various adsorbates can be avoided and the accuracy of the work function determination may be notably improved.

There are, however, problems of an easy implementation of KPFM setup operating in UHV. Basically, the problems are related to the performance of AFM in UHV. As it has been mentioned that KPFM is a variant of AFM operating in intermittent contact mode, where both the topography and KPFM feedbacks are based on Amplitude Modulation (AM). This kinds of implementation is not suitable for UHV conditions because of the significant increase of the cantilever's quality factor in absence of cantilever damping and subsequent increase in the response time of the probe.

In principle, the electronic damping using an out of phase signal applied to the probe simultaneously with the excitation signal is possible, however, the stability of such an operation mode has not been studied yet. To overcome the problems induced by AM, the Frequency Modulation (FM) can be routinely employed. Instead of using the amplitude of the cantilever's oscillation as a feedback parameter, the frequency shift can be employed as a measure for the tip-to-sample interaction. The FM-AFM implementation also allows the realization of a single-path KPFM using multichannel lock-in amplifiers which also allows a simultaneous monitoring of the tip-to-sample capacitance in addition to the CPD and topography [66]. It has also been demonstrated that AM-KPFM can be implemented on the basis of an FM-AFM setup. Using AM detection at the second resonance frequency, very high sensitivity at low AC voltages was achieved. This is a simple and stable detection method, where topography and CPD are acquired simultaneously but nearly independent of each other [67].

2.2.2 Photo-assisted Kelvin probe force microscopy

The KPFM technique can also be applied to the investigation of Surface Photovoltage (SPV) phenomena. The Photo-Assisted KPFM (PA-KPFM) setup resembles the conventional KPFM [68, 69] setup with an added illumination system which provides the opportunity for contactless studies of SPV with high spatial resolution. The SPV phenomenon consists of an illumination-induced change in the potential distribution within a semiconductor. The changes in potential distribution result in a charge re-distribution which can be subsequently examined using PA-KPFM. This technique provides also a possibility to investigate a photovoltaic effect which occurs on the surfaces of some semiconductors (e.g. Si or Ge) and metal-semiconductor or semiconductor-semiconductor junctions.

The SPV dependence on the wavelength of incident light can be used to extract important information about the band structure of the sample under investigation. In the case of band-to-band absorption, the band gap can be determined from extrapolation using the following relations [68, 70]:

- for direct band gap semiconductor:

$$SPV \sim \sqrt{h\nu - E_g} \tag{2.25}$$

- for indirect band gap semiconductor:

$$SPV \sim (h\nu - E_g)^2 \tag{2.26}$$

where E_g is the band gap and $h\nu$ is the energy of the incident photon.

The SPV method is well established as macroscopically applied technique [68], the variant based on KPFM, however, is not so frequently used so far. One of the main problems limiting its application are difficulties with proper sample illumination. A possible solution for this problem is the utilization of AdvancedTEC^{TM}EFM probes which recently became commercially available from Nanosensors. The SEM image of such a probe is presented in Fig. 2.4. The probe features a tetrahedral tip that protrudes from the very end of the cantilever. This allows a direct optical access to the point of measurements avoiding a shadowing of the area under investigation by the cantilever. A bright light source with the possibility of focusing to a small spot (several mm in diameter) should be used in order to achieve a high illuminance of the surface. To measure induced SPV, the sample should have an Ohmic back contact and has to be grounded. In absence of photochemical activity, the change in surface work function is equal to the generated SPV.

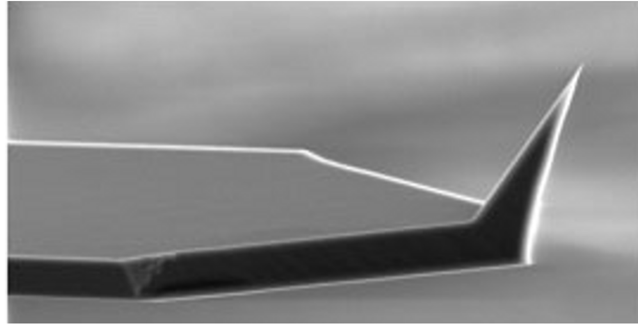

Figure 2.4 SEM image of AdvancedTEC probe from Nanosensors [71] used in conductive probe based AFM experiments under illumination.

2.3 Photoconductive AFM

One of the biggest advantages of Scanning Probe Microscopy (SPM) based techniques is their high versatility and applicability to different fields of research. It was shown above that the C-AFM technique is an efficient tool for the local electrical characterization of semiconductor materials on the nanometer scale. However, in some cases information obtained by C-AFM can be significantly enhanced via supplementary sample illumination. This modification of C-AFM is referred to as PC-AFM. The technique was originally developed for 2D mapping of photoelectric properties of organic thin films [23, 24, 72].

The PC-AFM setup is schematically depicted in Fig. 2.5. In PC-AFM, the sample surface

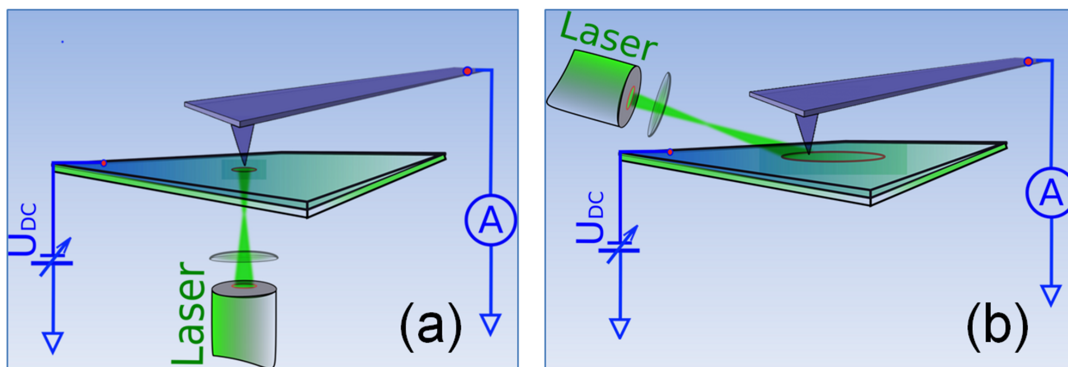

Figure 2.5 Schematic drawing of the photoconductive AFM (PC-AFM) setups presented in the literature so far: illumination from the back side (a) of the sample, oblique illumination from the top (b)

is biased and stays under illumination while current passing throughout the AFM tip is measured as a function of illumination intensity and/or wavelength. There are in principle two possible geometries of sample illumination, either the illumination from the back side of the sample [24, 72] or from the top [73] as depicted in Fig. 2.5. The first procedure

holds much favor because of the easier focusing and higher illumination intensity at the measurable region. Whereas the latter has been implemented so far at grazing incidence making light focusing rather problematic. Since the majority of materials demonstrate weak photoresponse, a high intensity light source is preferable. The simplest way is to use a laser. The difference in currents measured by PC-AFM between illuminated and dark situation carries important information like the optical absorption edge and the presence of electrically active defects.

PC-AFM is also used to track processes on the surface of a working solar cell. Recently, local photocurrents in blend polymer/fullerene solar cells were mapped by PC-AFM with a resolution down to 20 nm [24, 72, 74]. Its efficiency was demonstrated also for direct imaging of photocurrent pathways in ZnO based solar cells [75], WO_3, TiO_2, and composite WO_3/TiO_2 thin films [76].

In principle, the majority of semiconductors demonstrates photoresponse to a greater or lesser extent. Microscopically this effect is relatively easy to investigate since the integral photocurrent is sufficiently large in most of the cases. This is in contrast to the situation realized in PC-AFM where the amount of "working" material is limited by the volume under the tip-to-sample contact. The fraction of the photocurrent becomes vanishingly small, comparable to the dark current. Therefore, photocurrent detection by using lock-in technique seems suitable. This approach has been already successfully implemented in STM [77] to perform illumination-dependent studies, but was not applied to AFM so far.

In our PC-AFM setup, we implemented the lock-in detection and illumination from the top side using the above mentioned ATEC probes which significantly enhances sensitivity of the measurement (discussed in Sec. 2.3.2).

2.3.1 Light absorption in semiconductors

The process of light absorption in semiconductors may result in two types of electron transitions, namely intrinsic or band-to-band transitions (1) and extrinsic, involving levels in the band gap (2 and 3) depicted schematically in Fig. 2.6. As a result of intrinsic transitions, an electron appears in the conduction band leaving behind a hole in the valence band. Subsequently, the conductivity of the semiconductor increases due to increased charge carrier concentration. This increase of conductivity can be described as:

$$\Delta\sigma = q(\mu_n \Delta n + \mu_p \Delta p) \tag{2.27}$$

where μ_n and μ_p are the electron and hole mobilities, Δn and Δp are the excesses of electrons and holes due to the illumination. A very important parameter which characterizes the photo-conductivity of a semiconductor is the quantum efficiency, defined as a number of charge carriers produced per incident photon [54]:

$$\eta = \frac{I_{ph}}{q\Phi} = \frac{I_{ph}}{q}\left(\frac{h\nu}{P_{opt}}\right) \tag{2.28}$$

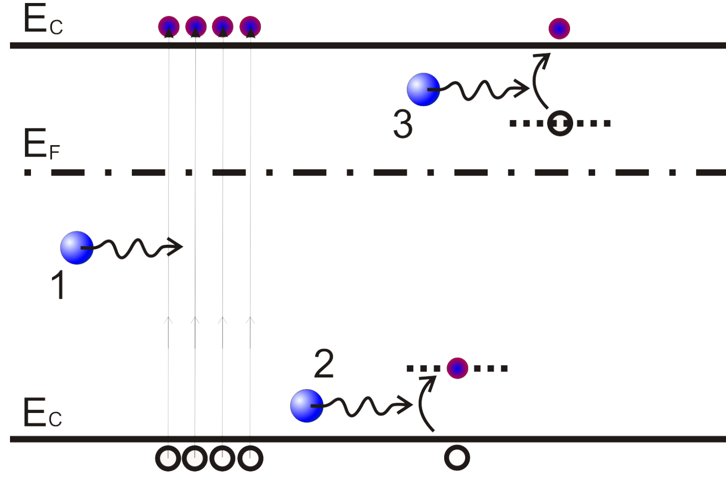

Figure 2.6 Possible mechanisms of light absorption in semiconductors.

where I_{ph} is the photocurrent, Φ is the photon flux and P_{opt} is the optical power. The photocurrent is directly proportional to the quantum efficiency and the number of incident photons. In general, the number of charge carriers generated by light is given as:

$$\Delta n = \tau_e G \quad (2.29)$$

$$\Delta p = \tau_h G \quad (2.30)$$

where G is the generation rate of electron-hole pairs, τ_e and τ_h are free lifetimes of the electron and hole, respectively.

Thus, the magnitude of photoresponse as well as transient properties may be strongly influenced by the setup configuration. In the following, a configuration of PC-AFM with the illumination of the sample surface from the top is implied. Independent of the absorption mechanism, the intensity of the incident light decays exponentially inside the material according to Lambert's law:

$$I(z) = I_0[1 - R(\lambda)] \cdot \exp(-\alpha z) \quad (2.31)$$

where $R(\lambda)$ is the reflectivity at wavelength λ, I_0 is the light intensity at the surface and α is the absorption coefficient. Therefore, almost all charge carriers are generated within a thin layer of thickness $1/\alpha$ and diffuse towards the back electrode. There are two extreme cases that one can consider:

- The thickness of an active layer is much larger than the carrier diffusion length. In this case, the charge carrier distribution within a semiconductor will have an exponential profile and the concentration at the back electrode will be small. In general, it is expected to observe a negligibly small increase in photocurrent since the current flow would be efficiently prohibited by the build-up of space charge. Therefore, such a situation should be avoided carrying out the PC-AFM measurements.

- The thickness of an active layer is comparable to the diffusion length. In this case, the charge carrier concentration at any point will depend upon the generation and recombination rates as well as upon the diffusion of the carriers from the surface. Here, one can expect to detect local variations with PC-AFM.

In the case of both, a conductive probe and a semiconductor sample, the tip-to-sample interface can be considered as metal-semiconductor junction (or diode). Therefore, under steady-state conditions the total photocurrent density through the reverse-biased depletion layer is given by:

$$J_{tot} = J_{dr} + J_{diff} \tag{2.32}$$

where J_{dr} is the drift current and J_{diff} is the diffusion current due to carriers generated outside the depletion layer in the bulk of the semiconductor and diffusing into the reverse-biased junction.

The electron-hole pair generation rate is given by:

$$G = \Phi\alpha \exp(-\alpha z) \tag{2.33}$$

where Φ is the incident photon flux per unit area and α is the optical absorption coefficient. The drift current J_{dr} is given by:

$$J_{dr} = \int_0^{W_d} G(z)\,\mathrm{d}z = q\Phi[1 - \exp(-\alpha W_d)] \tag{2.34}$$

where W_d is the width of the depletion layer.

The diffusion current density (for the minority carriers, e.g. holes) is given by:

$$J_{diff} = -qD_h \frac{\partial p}{\partial z} = q\Phi \frac{\alpha L_h}{1 + \alpha L_h} \exp(-\alpha W_d) + \frac{qp_0 D_h}{L_h} \tag{2.35}$$

where $L_h = \sqrt{D_h \tau_h}$ and p_0 is the equilibrium hole density. Therefore, the total current can be expressed as (details can be found in Ref. [54]):

$$J_{tot} = q\Phi \left[1 - \frac{\exp -\alpha W_d}{1 + \alpha L_h}\right] + \frac{qp_0 D_h}{L_h} \tag{2.36}$$

and quantum efficiency is given by:

$$\eta = (1 - R)\left[1 - \frac{\exp(-\alpha W_d)}{1 + \alpha L_h}\right]. \tag{2.37}$$

2.3.2 Technical implementation

Our home-made PC-AFM system for characterization of photoelectric properties is based on the MFP3D$^{\mathrm{TM}}$ AFM from Asylum Research equipped with the standard ORCA$^{\mathrm{TM}}$ module

which allows to carry out C-AFM experiments measuring currents in the range from 1 pA to 20 nA. To extend the range of measured currents we modified a standard cantilever holder from Asylum Research. The cantilever has been electrically isolated from the rest of the AFM's electronics. The currents were measured using an external circuit. We employ an external current preamplifier Model 1211 from DL Instruments for current detection in the range from 100 μA to 100 fA with a rise time constant of 10 μs or smaller. The system was extended with an external illumination system (see below) to carry out PC-AFM experiments.

To extend the sensitivity, a lock-in amplifier can be added to the setup. The use of lock-in technique for PC-AFM measurements is schematically depicted in Fig. 2.7. The system is equipped with the SR830 lock-in amplifier from Stanford Research Systems. The lock-In amplifier has differential inputs with 6 nV/$\sqrt{Hz}$ input noise. The input impedance is 10 MΩ, and the minimum full-scale input voltage sensitivity is 2 nV. The input can also be configured for current measurements with selectable current gains of 10^6 and 10^8 V/A. A line filter (50 Hz or 60 Hz) and a second harmonic line filter (100 Hz or 120 Hz) are provided to eliminate line related interference. For low frequency measurements (below 200 Hz), synchronous filters can be employed to notch out multiples of the reference frequency. Since the harmonics of the reference have been eliminated (notably $2f$), effective output filtering can be achieved with much shorter time constants.

The illumination of the sample surface is performed using either the external 150 W halogen lamp utilized in general for the optical imaging of the sample surface within the AFM or a Xe 150 W arc lamp. For investigation of the spectral dependence of the photocurrent, the light from the Xe arc lamp is collimated at the entrance slit of an OmniLab-150 monochromator from LOT - Oriel, coupled to an optical fiber at the exit port of the monochromator and then transmitted to the AFM head. The setup is demonstrated in the scheme shown in Fig. 2.7.

For light modulation, a chopper Model 197 from Signal Recovery is used. The chopper has a dual aperture and can operate in the range from 15 Hz to 3 kHz. For the experiments which require highest possible sensitivity and low noise, the operational range should be limited to 200 Hz to be consistent with the low-frequency filter of the used lock-in amplifier and illumination from the side. Since the chopper is equipped with an internal primary frequency standard, there are two possibilities to arrange the lock-in operation. The first option is to use the primary frequency standard of the chopper as a synchronization signal which is then applied to the triggering input of the lock-in amplifier. The second option is to use the internal generator which is a part of the lock-in SR830 amplifier to trigger the chopper. Both variants were tested and no significant difference in the performance of the lock-in amplifier was found.

We also implemented additional LabView procedures to optimize the investigation of the persistent photoconductivity using a PCI-6024E data acquisition board from National Instruments. The photocurrent spectra can be measured starting from longer wavelengths with the time delay varying in the range from 0.1 s to 2 min between acquisition of two neighboring data points. This time delay is usually sufficient to account for the time needed

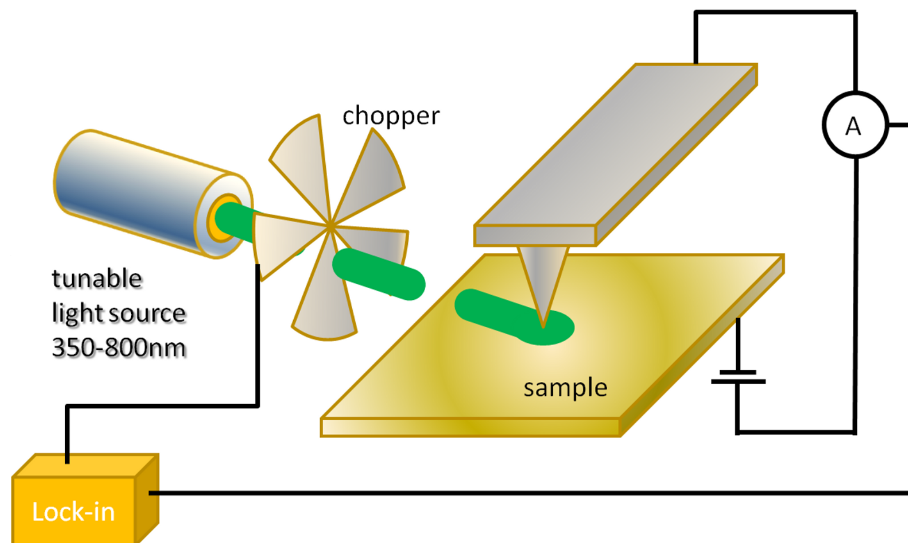

Figure 2.7 Schematic drawing of the implemented PC-AFM setup employing lock-in detection principle.

for the photocurrent saturation. The data can be additionally averaged. In usual operation, each data point in the photocurrent spectra represents the average value of 100 points measured at 1 kHz of acquisition rate.

The illumination at large angle of incidence (with respect to the surface normal) has also some disadvantages, like increased reflection from the surface which results in a drop of photoresponse. Thus, we implemented the illumination from the top. (With some extensions that are available from Asylum Research the system can be configured for the illumination from the bottom (compare Fig. 2.5(a)), however this has some disadvantages discussed in the following.) It is essential that illumination of the sample's surface was done in the configuration "from the top" which is schematically depicted in Fig. 2.8. This helps to reduce the loss of light intensity compared to the configuration "from the bottom" where the light is transmitted throughout the sample bulk until it reaches the area under the tip ending. This becomes especially important when the substrate has a large coefficient of absorption or is not transparent in the desired wavelength range at all.

In particular, the situation presented in Fig. 2.8 is realized for the arrays of upright standing ZnO NRs which were under investigation in the present work. The glass substrate with the ITO layer would significantly reduce the light intensity in the ultraviolet (UV) region, the region of the optical absorption of ZnO. Whereas the advantages of the configuration for illumination "from the top" are obvious, it has one disadvantage which is the difficulty of the technical implementation. The major technical problem is the shadowing of the tip-to-surface electrical contact area by the cantilever. Since the majority of the commercially available conductive probes have the tip attached under the cantilever and relatively far away from the cantilever edges, it is unlikely that the area close to the tip-to-surface contact

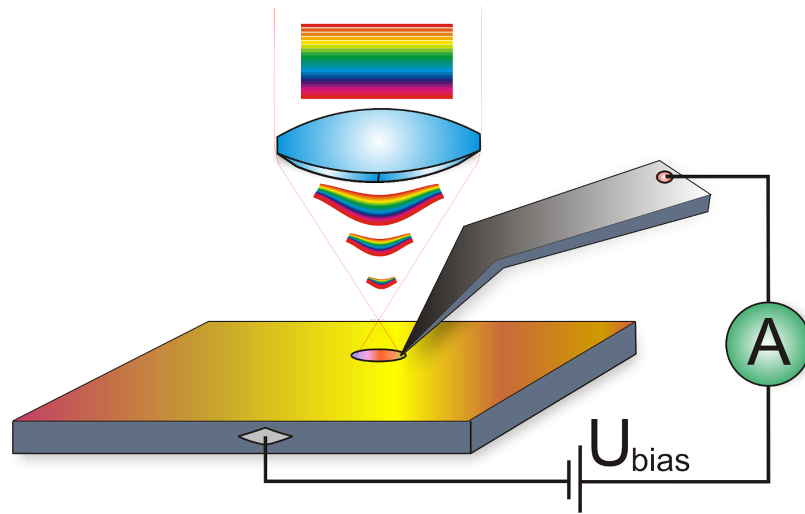

Figure 2.8 Schematic drawing of the modified PC-AFM setup using AdvancedTEC conductive probes. The sample in the present configuration is illuminated from the top side and biased. Conductive, Pt- coated ATEC-CONTPt^{TM} probes are used to avoid shadowing of the area under investigation by the cantilever.

can be appropriately illuminated.

Partially, this problem can be solved by using the Nanosensors^{TM} AdvancedTEC^{TM} CONTPt^{TM} (ATEC-CONTPt^{TM}) conductive probes which have a tetrahedral tip that protrudes from the very end of the cantilever (shown in Fig. 2.4 and schematically depicted in Fig. 2.8). Therefore, the surface is not shadowed by the cantilever and can be illuminated at small angles (0°-20°) of incidence. The probes are heavily doped and have a 25 nm thick $PtIr_5$ coating on both sides, so the illumination does not influence the conductivity of the probe by itself.

The transparency of the optical system used for the illumination was carefully examined. It has been determined that the system is transparent in the range from 360 to 900 nm. The illumination from the AFM's feedback laser diode which has a wavelength of ~850 nm is also coupled to the illumination system. Nevertheless, the illumination from the feedback laser diode does not affect the measurement in most of the cases since its wavelength lies in the transparency range for the majority of materials.

In the configuration "from the top", we employ the optical system of the MFP3D^{TM}AFM which is normally used for the optical imaging of the cantilever on the sample surface. Using some additional external elements, like optical fiber couplers and an especially designed fiber holder, the light is transmitted from the exit port of the monochromator throughout the AFM head and the prism of the cantilever holder to the sample surface and focused in a spot of about 1 mm in diameter. A calibration curve which accounts both, for the transmittance of the optical system and the emission spectrum of the light source has been recorded and used for the correction of the photocurrent spectra.

Since operation in UHV is preferable in many cases we have made attempts to implement a similar illumination system into our UHV Omicron AFM/STM system, however, experienced problems with the increased mechanical noise due to design flaws. Nevertheless, the implementation is feasible and basically, requires exchange of some mechanical components of the original Omicron AFM/STM system.

Chapter 3

Results I: Supported InAs nanostructures on GaAs substrates

In the fabrication of functional semiconductor thin films for lasers, solar cells, and photodetector applications, phase-separated nanostructures like supported NWs, Nanorods (NRs), QRs or antiphase defects are frequently evolving. These structures may be advantageous or disadvantageous for the device performance. In any case, their electrical properties have to be studied on the nanometer scale. Besides KPFM, C-AFM is a technique to reveal the electrical characteristics of such phase-separated semiconductor nanostructures as this will be demonstrated in two exemplifying cases.

3.1 InAs nanowires (NWs) and nanodots (NDs) on self-organized GaAs(110)

The present section is based on the results published in Ref. [3] from the publications list.

Self-assembled InAs and InGaAs nanostructures have been studied over many years but are still of great interest for application in electronics, high-speed spintronic devices, etc. Samples for our investigation were epitaxially grown on misoriented GaAs(110) substrates.

Applying C-AFM, we examine here InAs nanostructures, namely nanowires and nanodots grown by molecular beam epitaxy on GaAs. Two different self-organized GaAs substrates have been used as stepped templates. We demonstrate that C-AFM is suitable for the characterization of low-dimensional structures, like supported NWs and NDs beyond the limits of conventional AFM. C-AFM technique was used to study the surface topography and conductivity simultaneously.

3.1.1 Sample preparation: Conventional and H-assisted epitaxial growth

The InAs samples were grown by our collaborators at the Instituto de Ciencia de Materiales de Madrid, Spain using a solid-source Varian MBE-360 system described elsewhere [78]. The native oxide on the GaAs(110) substrates misoriented towards (111)A by 2° was removed prior to epitaxial growth under an As_4 flux of (2-3)$\times 10^{15}$ molecules $cm^{-2}s^{-1}$ either by thermal desorption at 610 °C or by atomic H irradiation at 450 °C. GaAs buffer templates with a thickness of 100 nm (500 ML in the [110] direction) were then deposited under different kinetic regimes. Template A was grown under As-rich conditions (430 °C, As:Ga flux ratio of 30) to favor the formation of $[1\bar{1}0]$-oriented bunched steps. The formation of terraces bounded by $[1\bar{1}5]$-type steps in template B, where the influence of both chemisorbed H and step orientation on In migration and incorporation kinetics were investigated, was induced during growth under As-deficient conditions (500 °C, As:Ga flux ratio of 10) after H-assisted surface cleaning, as atomic H promotes the rapid reorganization of the surface steps along $[1\bar{1}n]$ ($n \geq 2$) in this growth regime [78]. The appearance of the templates A and B is schematically depicted in Fig. 3.1. Subsequently, 5 ML of InAs were deposited on each of these templates under identical As-rich conditions (425 °C, As:In flux ratio of 60) at a growth rate of 0.1 ML$\cdot s^{-1}$.

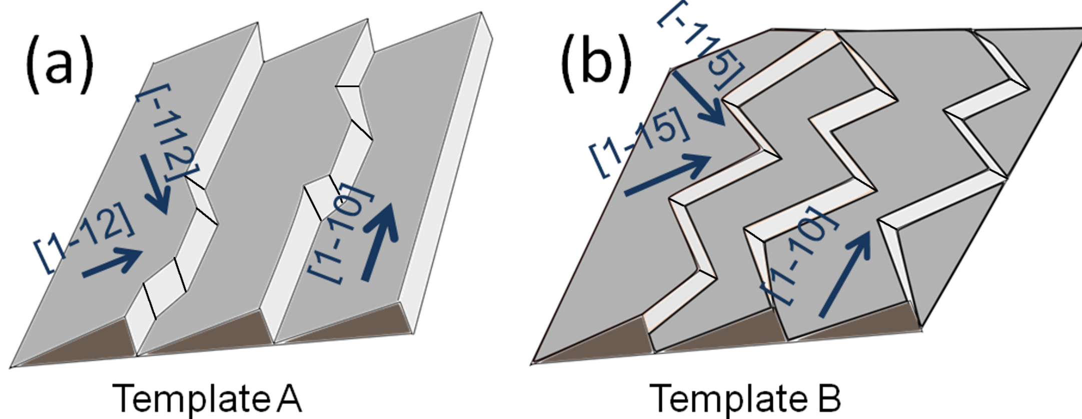

Figure 3.1 Schematic representation of self-organized GaAs(110) substrates used for the growth of supported InAs NWs (a) and NDs (b).

3.1.2 Investigation of InAs NW and ND formation by means of C-AFM

Conductivity measurements of InAs NWs

C-AFM under ambient conditions. In preliminary measurements, a sample containing InAs NWs was measured under ambient conditions using DCP11 probes from NT-MDT^{TM}with a force constant in the range of 5-12 N/m. Measurements have been preformed using DI Nanoscope IIIa equipped with the homemade C-AFM module. The samples were contacted using silver paint applied to its back side. Prior to the contacting, the native oxide was mechanically removed from the surface. The applied loading forces ranged from 30 to 100 nN. In Fig. 3.2, the topography (a) and current map (b) recorded at a sample bias of -5 V are presented. The topography image Fig. 3.2 (a) reveals a characteristic multiatomic step array with step edges running along $[1\bar{1}0]$, $[1\bar{1}2]$, and $[\bar{1}12]$ directions separated by (110) terraces. The current absolute values ranged from 0 to 15 pA. The current map reveals an increase of conductivity at the step edges of the GaAs substrate indicated by current peaks occurring along the $[1\bar{1}0]$ direction but almost no current along the $[1\bar{1}2]$ and $[\bar{1}12]$ step edges. However, the current spots are streaky and not continuous along the $[1\bar{1}0]$ direction, which as will be shown in the following does not reflect the real situation.

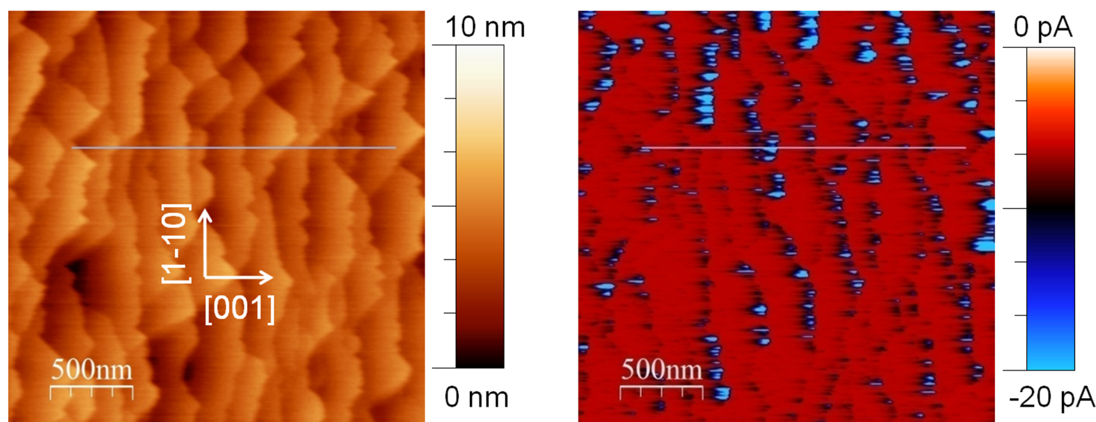

Figure 3.2 2.5 μm×2.5 μm topography image of InAs/GaAs NWs measured under ambient conditions (a) and 2D current map recorded at -5 V of sample bias (b) (from [29]).

C-AFM in UHV. The topography and current map recorded under UHV conditions for the same sample are depicted in Fig. 3.3 (a) and (b). The sample bias applied in this case was -9.1 V (higher than in ambient) because of the smaller sensitivity of the pre-amplifier used in the UHV C-AFM setup [29]. The tip load was about 100 nN. In addition to 2D current maps we also performed the I-V characterization under UHV conditions which will

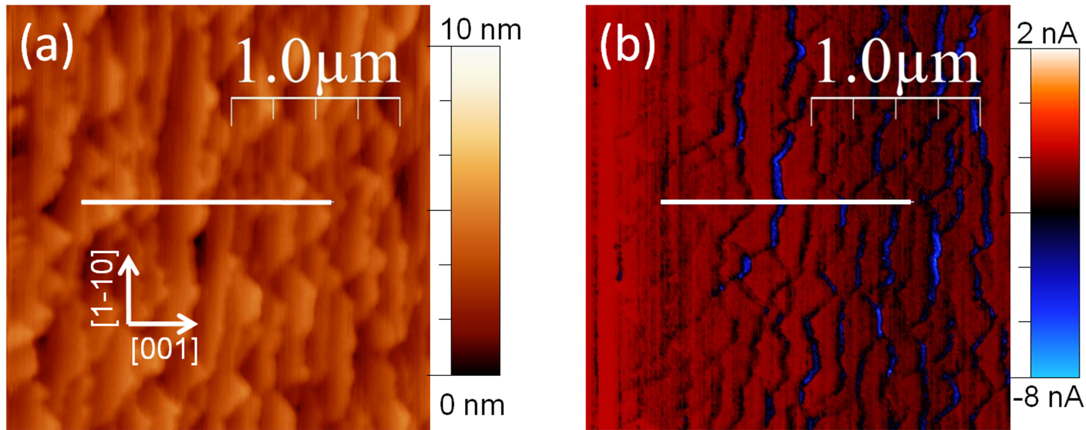

Figure 3.3 C-AFM results of InAs NW on GaAs recorded in UHV. 2.5 μm× 2.5 μm topography image (a), 2D current map recorded at -9.1 V of sample bias (b) (from [29]).

be discussed in Sec. 3.1.3. The application of higher voltages during the measurements in UHV is caused by a smaller gain factor of the current pre-amplifier in UHV C-AFM setup (compared to the one used in ambient). Here, the current image clearly shows stripes of high conductivity running along the $[1\bar{1}0]$ direction. In contrast to the images recorded under ambient conditions, weak but detectable conductivity is also observed along the $[1\bar{1}2]$ and $[\bar{1}12]$ directions. The overlap of the corresponding cross-sections of the topography and current images taken along the [001] direction which is depicted in Fig. 3.4 (a) clarifies that

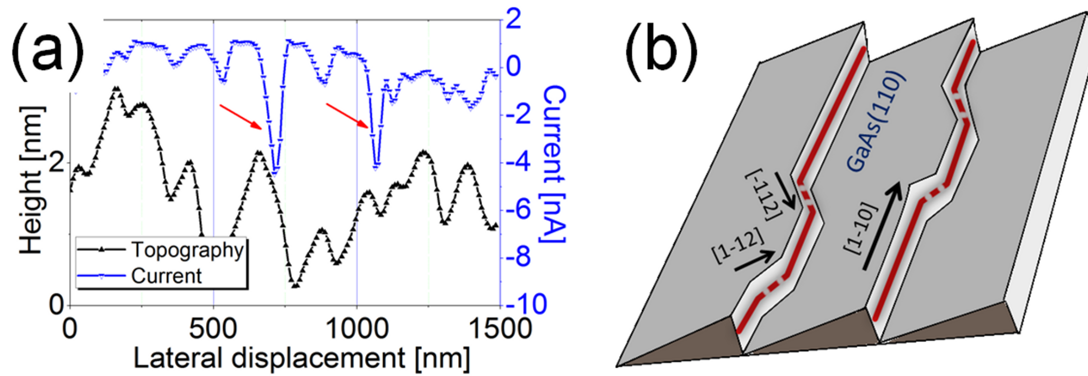

Figure 3.4 Cross-sections along the line marked in Fig. 3.3; (a), schematic drawing of InAs NWs growth on the giant steps of the GaAs surface (b). Comparatively small amounts of InAs on the $[1\bar{1}2]$ and $[\bar{1}12]$ edges depicted by the *dashed line* (from [29]).

the regions of maximum conductivity coincide with the center of the step bunches.

When considering the tip-to-sample contact, we assume that the Schottky barrier height for InAs is lower than the height for the GaAs (the electron affinity for the GaAs is 4.07 eV

and 4.9 eV for InAs). Therefore, the areas of higher conductivity can be attributed to the presence of InAs.

The difference between the current maps measured in UHV and under ambient conditions can be attributed to instabilities caused by the presence of adsorbed water on the surface exposed to air. Since the current maps were acquired at negative bias voltages, anodic oxidation of the surface can be ruled out [44]. The instabilities can be explained via contact rupture during the imaging process. When the conductive tip comes into contact with the adsorbed water film on the biased surface, water dissociation takes place and contact rupture occurs. This appears in the current maps as a current termination and lateral spreading of the current peaks. Therefore, UHV C-AFM current maps demonstrate much higher stability than those taken in the ambient.

Referring to the current map measured in UHV, (Fig. 3.3(b)) InAs preferentially decorates step edges along the $[1\bar{1}0]$ direction. The InAs decoration is less pronounced along the $[1\bar{1}2]$ and $[\bar{1}12]$ step edges. This result is schematically illustrated in Fig. 3.4(b)).

The latter finding is in good agreement with earlier cross-sectional Transmission Electron Microscopy (TEM) investigations [79], which revealed that the formation of InAs NWs is a result of step decoration of the self-organized GaAs layer. The TEM measurements showed that InAs preferentially decorated the $[1\bar{1}0]$ step edges rather than those along $[1\bar{1}2]$ and $[\bar{1}12]$. In contrast to cross-sectional TEM investigations with little statistics, the 2D current maps reveal the uniformity in lateral arrangement of the NWs [34].

Mechanism of nucleation. The origin of the preferred nucleation of InAs on $[1\bar{1}0]$ step edges is to be found in its inherent topology [80]. The dangling bonds of the Ga-terminated $[1\bar{1}0]$ step edge cannot re-hybridize their charge density to satisfy the auto-compensation principle and consequently, these steps are very reactive, acting as sinks for diffusing adatoms. In addition, the sticking of adatoms is likely to have a low activation energy because no bonds need to be broken to accommodate the incoming In adatoms. But re-hybridization of the dangling bond charge density in the case of $[1\bar{1}n]$-type steps can be readily achieved by the creation of vacancies and/or step edge re-bonding to form As dimers [81], resulting in very stable step configurations. Therefore, the limiting factor of InAs nucleation on $[1\bar{1}2]$-type steps at the temperature of our growth experiments is most probably the high activation energy associated with the insertion of In adatoms into step edge As dimers. This kinetic hindrance induces a flux of migrating In adatoms away from $[1\bar{1}n]$-type steps toward $[1\bar{1}0]$-type steps, where incorporation is more favorable as has been discussed in Ref. [34].

Conductivity measurements of InAs NDs

The current maps of the surface containing InAs nanostructures on template B measured under UHV conditions were acquired under similar conditions to those used for InAs NWs imaging. The morphology of the surface under investigation and the corresponding 2D current map are shown in Fig. 3.5 (a) and (b), respectively. As shown in [34], the specific morphology of the template along with the H-assisted surface cleaning preliminary to MBE

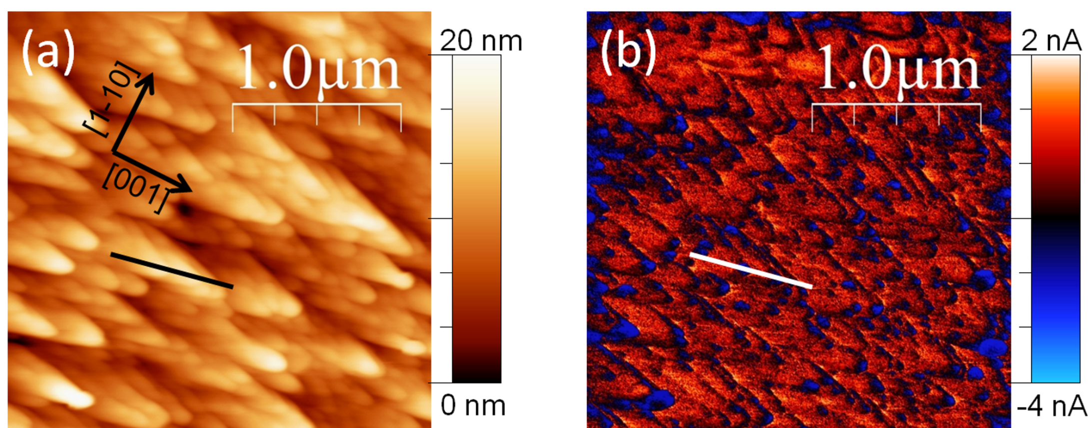

Figure 3.5 C-AFM results of InAs/GaAs NDs measured under UHV conditions. 2.5 μm×2.5 μm topography image (a), 2D current map recorded at -9.1 V sample bias (b) (from [29]).

growth offers preferred nucleation sites resulting in a lateral confinement of InAs. This leads to the transition from 2D growth to 3D mound formation which is energetically and kinetically most favorable [34]. The analysis of the correlation between topography (Fig. 3.5(a)) and current map (Fig. 3.5(b)) simultaneously with the corresponding profiles (Fig. 3.6(a)) taken almost along the tilt direction on the terraces bounded by $[1\bar{1}5]$ and $[\bar{1}15]$ steps, revealed several current peaks originating from the terrace. The current from the terrace apex is most pronounced and has a magnitude of $\sim$ 4 nA. The comparison with data ob-

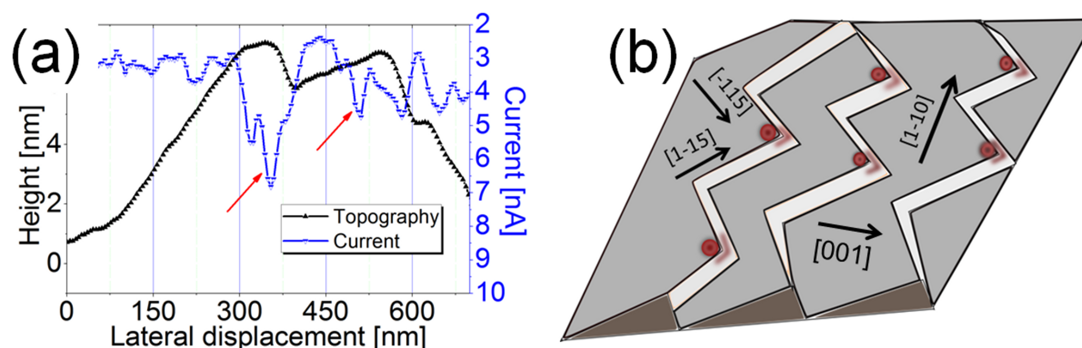

Figure 3.6 Topography and corresponding 2D current map cross-sections (a) along the lines marked in Fig. 3.5, current peaks are marked by arrows. Schematic drawing of InAs ND growth on the terrace apexes of GaAs surface is presented in (b) (from [29]).

tained from the surface containing InAs NWs enables us to conclude that InAs deposits form three-dimensional (3D) clusters with an average lateral size of ∼65 nm at the apexes of the

triangular terraces. The estimated density of the clusters is 4×10^9 cm^{-2}, the height of the clusters can be as high as 50 nm, that is, more than three times greater than the nominal 5 ML coverage, which suggests that they have grown by incorporating material both from the incoming flux and from the surrounding layer.

Additionally, it was found that the entire surface of the terraces is covered by small and dense 2D islands which are about 10 nm in lateral dimension [34], their height is estimated as $\sim$1-2 nm. The currents measured from these 2D islands were smaller than those measured for 3D islands at the same bias voltage. This observation is hard to interpret, since the effective contact area between the tip and the surface can be smaller than the size of the 2D islands, causing therefore smaller currents at the same current density. However, this still may serve as an evidence of some chemical exchange which takes place between In atoms in the 2D nuclei and the substrate Ga atoms underneath and leads to the formation of InGaAs [34]. We expect a smaller concentration of In atoms in 2D islands and therefore an increase in the Schottky barrier height.

Mechanism of nucleation. At the temperature applied in our experiments, the InAs growth reaction is likely to follow a different pathway on the H-terminated surface, involving H-bonded In adatoms and AsH_x intermediate species [82]. As shown earlier, H-assisted growth through these intermediate species enhances the As incorporation kinetics [78], favoring the preferential attachment of adatoms to upper step and island edges. In our opinion, the most plausible explanation for the observed surface morphology after 5 ML InAs deposition is the destabilization of the growth front due to this preferential attachment of adatoms to ascending step edges in the presence of a weak Ehrlich-Schwoebel barrier. According to theoretical models described in Ref. [83], this creates a growth-induced diffusion flux in the uphill direction that destabilizes growth on the vicinal surface leading to 3D mound formation, irrespective of the occurrence of an induction layer-by-layer period. In this growth scenario the adatoms arriving at the terraces by upward mass transport or from the deposition flux will tend to incorporate preferentially at the upper side of the steps where InAs material can be partially relaxed, rather than at energetically less favorable sites on the terrace center or at the foot of steps where InAs would be overstrained [84]. This is in good agreement with Fig. 3.5(b).

Consequently, the selective nucleation at the apices tends to make the protruding parts of the steps unstable towards transverse meandering [85], while the strain energy increases until the height of the steps reaches a critical thickness and 3D clusters are formed on the terrace apices. Besides, chemisorbed H lowers the surface energy of the growing layer favoring the formation of a 3D island morphology [86]. In addition, the height of the clusters can reach 50 Å, which is more than three times larger than the nominal 5 ML coverage, which suggests that they have grown by incorporating material both from the incoming flux and from the surrounding layer. The observed change from step decoration to 3D growth for InAs on the vicinal GaAs (110) surface is consistent with an enhancement in the adatom incorporation kinetics to upper step edges via AsH_x intermediate species and to the reduced free energy

of the H-terminated surface. In turn, the specific morphology of the template used in the H assisted MBE experiment contributes to confine laterally the InAs nanostructures by offering preferred nucleation sites where the transition from 2D growth to 3D mound formation is energetically and kinetically most favorable [34].

3.1.3 I-V Characterization

The I-V characteristics recorded from the NW region (a) and the InAs free terrace (b) of the conventionally grown sample (template A) are presented in Fig. 3.7. I-V spectroscopy reveals the formation of a Schottky-type junction between the diamond coated Si (DCP11) tip and the semiconductor surface in both cases. The I-V characteristics recorded from the InAs NW region are characterized by slightly lower values of the cut-in voltages (indicated in Fig. 3.7 by green arrows) with an average value of ∼2.1 V whereas ∼2.2 V are observed for the characteristics recorded from the terrace region. In contrast to the cut-in voltage, the breakdown voltages (red arrows in Fig. 3.7) determined for the InAs NW region are higher compared to those obtained for the InAs free terrace. The average breakdown voltage equals to -3.9 V and -2.6 V for the InAs NW and terrace region, respectively. In general, the values

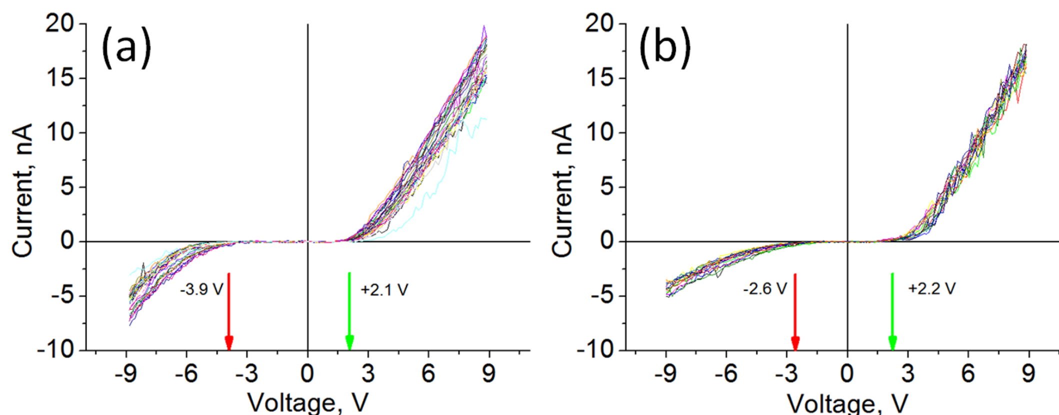

Figure 3.7 The I-V curves recorded from the NW region (a) and the terrace free of InAs (b) of the conventionally grown sample (template A).

of the cut-in voltage are consistent with the data known from the literature. In [87], it was shown that I-V characteristics recorded from the InAs NW region demonstrate degenerated behavior, whereas KPFM data revealed more negative surface potentials for the same region. Such a behavior can be explained in terms of electron accumulation which occurs near the surface of InAs [88].

We have also made an attempt to perform I-V characterization of the H-assisted grown sample (template B), however, low reproducibility of the measured data hampers any further analysis. The difficulties are mainly caused by the small lateral dimensions of the InAs NDs

and the rough substrate morphology which makes defined positioning of the tip with the given UHV C-AFM setup almost impossible.

Conclusions

The results presented in the following, prove that the C-AFM technique might be successfully applied not only as a tool for the investigation of electrical properties in $III-V$ quantum dots and wires on the nanometer scale but also to a broad range of nanostructures with phase separation. Using C-AFM it has been revealed that in the case of the conventionally grown sample InAs decorates step bunches along $[1\bar{1}0]$, $[1\bar{1}2]$, and $[\bar{1}12]$ directions forming InAs NWs. For the H-assisted grown sample it has been found out that InAs forms NDs at the apexes bounded by steps running along $[1\bar{1}5]$ and $[\bar{1}15]$ directions. Local I-V characteristics recorded from the InAs NW region and the InAs free terrace demonstrate Schottky like behavior. The NW region exhibits a lowering of the cut-in voltage and increase of the breakdown voltage compared to the terraces. At the same time, the I-V characteristic recorded from InAs rich regions demonstrate rather significant scatter of parameters, which makes them difficult for a numerical analysis and comparison with those recorded from InAs depleted areas.

3.2 InAs quantum rings on GaAs(100)

As discussed in Sec. 1.1, quantum nanostructures play an important role in nowadays electronic devices, like photodiodes, lasers, etc. The spatial confinement of the charge carriers leads to changes in the material's electronic structure, providing a way for tailoring of electronic properties. These changes are also advantageous for the device's performance, improving the operational characteristics at room temperature. Nanostructures with quantum confinement can be obtained by strain-driven self-assembly. Shape, dimensions and compositional distribution in strain-driven self-assembled semiconductor nanostructures can be tailored, in turn, by the deposition of a capping layer [89].

Here, we studied the electrical properties of InAs QRs in order to gain information about the compositional distribution by means of UHV C-AFM. Previous C-AFM measurements of InAs QRs performed under ambient conditions [90] revealed some open questions with respect to results obtained by methods of in-situ characterization [8, 89, 91].

Attempts to perform C-AFM characterization of the sample containing InGaAs quantum rings under ambient conditions may lead to an ambiguous interpretation of the obtained results [90]. The main obstacle is the formation of a non-uniformly thick surface oxide layer. In the absence of an oxide layer, the current recorded from the sample surface can be correlated to the content of In in the InGaAs solid alloy. Larger currents normally correspond to higher content of In. The higher conductivity is due to the low Schottky barrier height for the contact formed between InAs and the majority of conductive probe materials [92–94]. On the other hand, the presence of an oxide layer on the surface alters the current flow. If, for some reasons, the oxide layer thickness is larger over the In-rich region (compared to the pure GaAs), the current map may appear reversed. To circumvent this, the characterization of the InGaAs QR samples has been entirely performed in UHV.

3.2.1 Sample preparation

The samples were grown by cooperation partners at the Instituto Officiana dei Materiali CNR, Laboratorio TASC in Trieste (Italy) using molecular beam epitaxy on a GaAs:Si(001) buffer layer. First, QDs were formed by depositing about two Monolayer (ML) of InAs at a substrate temperature of 540 °C in 15 cycles at a rate of 0.03 ML/s, alternated with 2 s growth interruptions. The temperature was then lowered to 490 °C, followed by the deposition of a 2 nm capping GaAs layer at 1 ML/s and 30 s annealing at the same temperature (details can be found in [95]). The steps of sample preparation are schematically depicted in Fig. 3.8. The sample was finally rapidly cooled down and overgrown with a protective layer of As_4 to avoid oxidation of the surface during exposure to air. With this As_4 layer the sample could be shipped under ambient conditions.

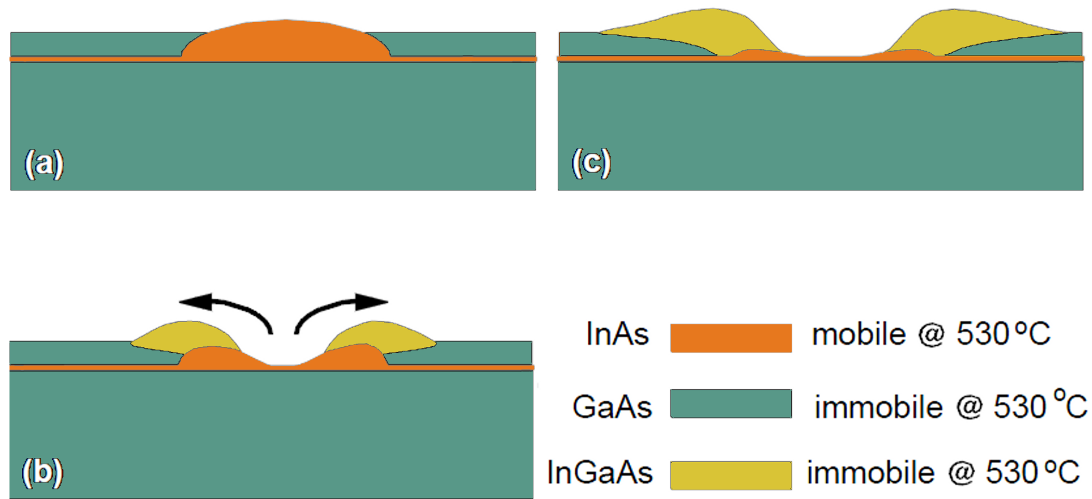

Figure 3.8 Possible mechanism for the self-assembled InAs quantum ring formation (adapted from [96]). First, InAs quantum dots are epitaxially grown on GaAs and followed by the deposition of a 2 nm capping GaAs layer with 30 s annealing at 490 °C (b). The InAs transport from the central hole and mixing with GaAs is denoted by arrows. The resulting structure is schematically depicted in (c).

3.2.2 Removal of the protecting As_4 layer in UHV

Prior to the C-AFM investigations in our UHV system, the As_4 capped samples were placed for at least $\sim$ 24 hours into the load lock chamber with a base pressure of $\sim 5\times10^{-6}$ mbar for the initial degassing. The temperature during the degassing process was held at $\sim$ 70-80 °C. After degassing the samples were introduced into the main UHV chamber with a base pressure of $\sim 5\times10^{-10}$ mbar. For the removal of the protecting As_4 layer (denoted in the following as "uncapping") the samples were heated up to 350 C° in order to evaporate the protecting layer. Simultaneously the pressure was screened by a hot cathode ionization gauge. The temperature ramping rate during uncapping did not exceed 3 °C/min and was reduced to $\sim$ 0.5 °C/min at the expected temperature of As_4 desorption. The uncapping was considered as successful when a pressure increase around the desorption temperature of amorphous As_4 was observed. Once the pressure increase happened we kept the sample at the corresponding elevated temperature for another 15-20 min. The control of the surface quality after uncapping has been performed by means of in-situ AFM characterization in contact and intermittent contact mode (see Fig. 3.9(a) and (b)). In some cases, residuals of the As_4 layer were found after the uncapping. To remove them completely, we repeated the described procedure several times until a surface free of any residuals had been reached.

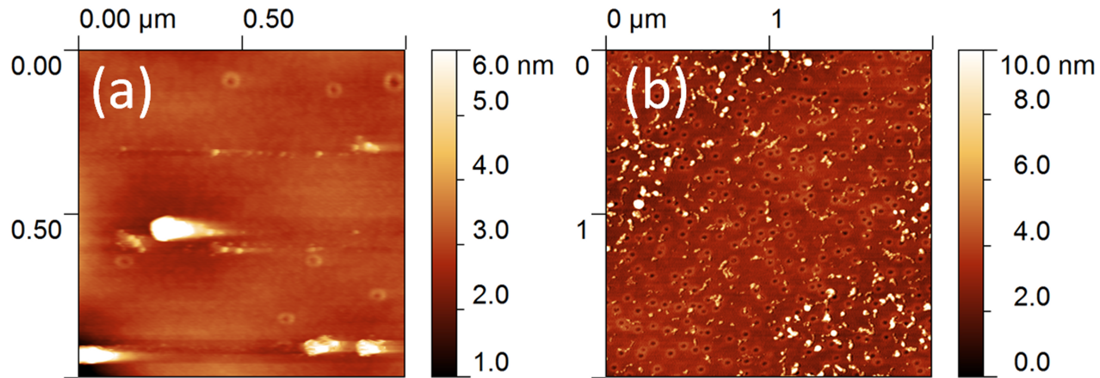

Figure 3.9 Contact (a) and intermittent contact (b) mode topography AFM images of InGaAs quantum ring sample containing some small amounts of As_4 residuals (seen as small white spots of random shape) in addition to the QRs.

3.2.3 Topography characterization of quantum rings

A contact mode AFM topography image of an InGaAs QR sample obtained after proper uncapping is depicted in Fig. 3.10. The image has been acquired with a TiN coated CSG01 probe from NT-MDT^{TM}. Since the distribution of morphological and electrical properties within the ensemble of QRs are of big importance we performed statistical analysis employing autocorrelation functions. The diameter of the quantum rings was evaluated using 2D

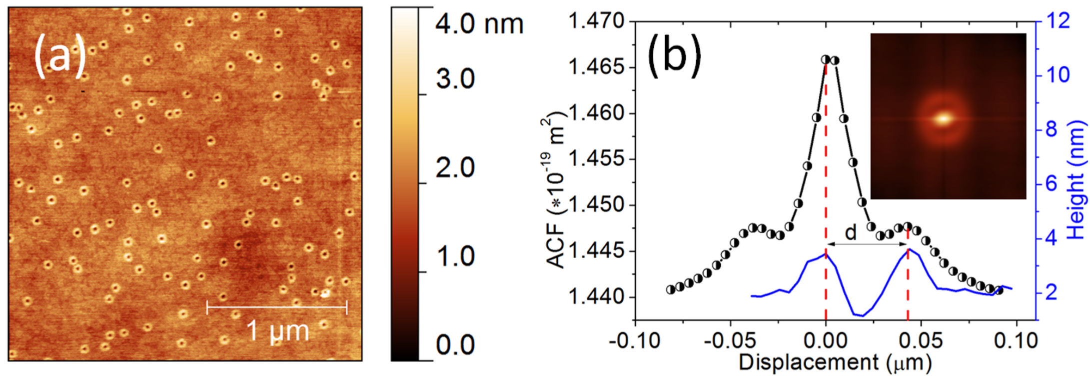

Figure 3.10 Topography acquired in contact mode under ambient conditions (a) and cross-sections (b) taken from the topography image and corresponding 2D autocorrelation hight map. The 2D ACM is given as inset in (b).

Autocorrelation Height Map (ACM) (depicted as an inset in Fig. 3.10 (b)). The ACM was calculated for a 512×512 pixels topography image. The ring feature revealed by the ACM is highly central symmetrical, indicating high central symmetry of the quantum rings. The average QR diameter has been determined from the cross-section of the 2D ACM calculated

from the topography data. Contact mode topography images were acquired using DCP11 diamond coated probes with a guaranteed tip radius of 80 nm. The cross-section was taken along the direction 45° oriented towards the scan line direction. The average diameter for this particular sample has been determined to be 40 ± 10 nm. We also succeeded in measuring structures with diameters down to 20 nm. The C-AFM characterization of such small quantum rings is presented in the following.

3.2.4 C-AFM characterization

The C-AFM measurements were performed at a pressure of $\sim 5{\times}10^{-9}$ mbar using the UHV C-AFM setup described in Sec. 2.1. The tip loading force during the course of the measurements was in the range of 10-100 nN. The current maps have been recorded both at positive and negative sample bias. For the present analysis, the current maps recorded at +2 V and -2 V were used.

2D current maps: Influence of the sample bias polarity

Positive bias. Topography and corresponding current map recorded at a sample bias of +2 V are presented in Fig. 3.11. The tip loading force during the course of the experiment did not exceed 30 nN. The topography image reveals the presence of QRs free of As_4 residuals after the 3rd cycle of uncapping. The visible elongation of the rings along the fast scan direction is an artifact of the measurement. The influence of these artifacts has been statistically eliminated, employing 2D autocorrelation analysis. The average QR's diameter for the present sample has been determined from the 2D ACM corresponding to the topography image to be $\sim$ 22 nm. This value, however, can slightly exceed the actual one due to the tip convolution. We have also made an attempt to estimate the actual diameter by a peak fitting procedure applied to the cross-sections of the 2D ACM described below (see Fig. 3.13 (d)). The current map recorded at the same time, reveals a higher conductivity at the maximum of the quantum ring's rim.

Negative bias. The current map recorded at -2 V of sample bias from the same surface area is presented in Fig. 3.12. The current map recorded at negative surface bias exhibits basically the same trend regarding the preferential current paths. The rims of the QRs appear more conductive than the central hole and surrounding. Interestingly, re-scanned surface areas exhibit increased conductivity with respect to the first scan. This may point towards the presence of As_4 residuals. As this will be shown further, the presence of such residuals also leads to an increase of conductivity (see Fig. 3.15). The current magnitude is at the level of $\sim$ 30 nA regardless of the bias polarity and, therefore, the current flow direction. This may serve as an evidence for symmetrical I-V characteristic with respect to the zero point.

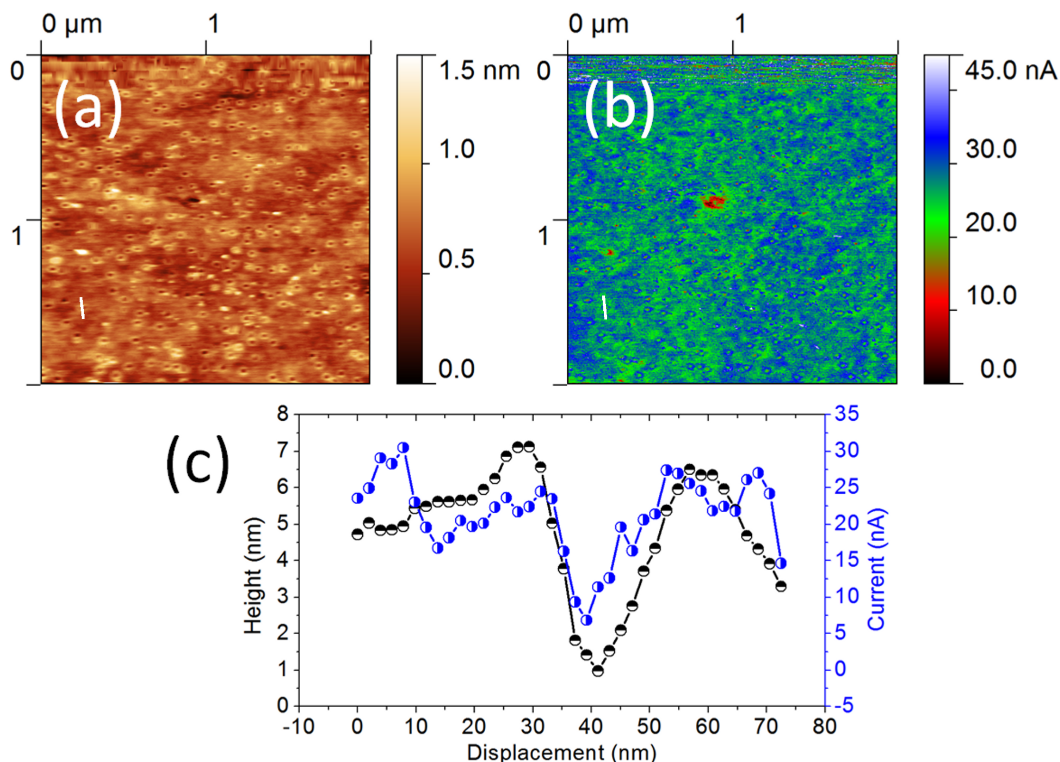

Figure 3.11 C-AFM images of InGaAs quantum rings recorded in UHV: topography (a), current map (b) and corresponding cross-sections (c) taken along the white lines indicated in (a) and (b). The images were acquired in contact mode AFM at +2 V of sample bias.

Comparison to the data obtained by other techniques. A similar C-AFM experiment on quantum rings [90] performed under ambient conditions yielded a similar 2D current map as obtained in UHV. The results were, however, argued and attributed to the influence of a native oxide layer which alter the current map significantly. Basically, the main difficulty of the data interpretation is the low conductivity of the central QR's hole. The results obtained by means of the cross-sectional scanning tunneling microscopy (XSTM) [8], cross-sectional transmission electron microscopy (XTEM) [91], and X-ray photoemission electron microscopy (XPEEM) [89] suggest that the In content increases monotonically towards the ring center. This would mean that in C-AFM current maps the center of the QR should appear more conductive with respect to the outer rim and surrounding. This, however, is not observable neither in the C-AFM experiments performed in UHV nor in the experiments performed under ambient conditions. The inconsistency can be a subject for further discussion.

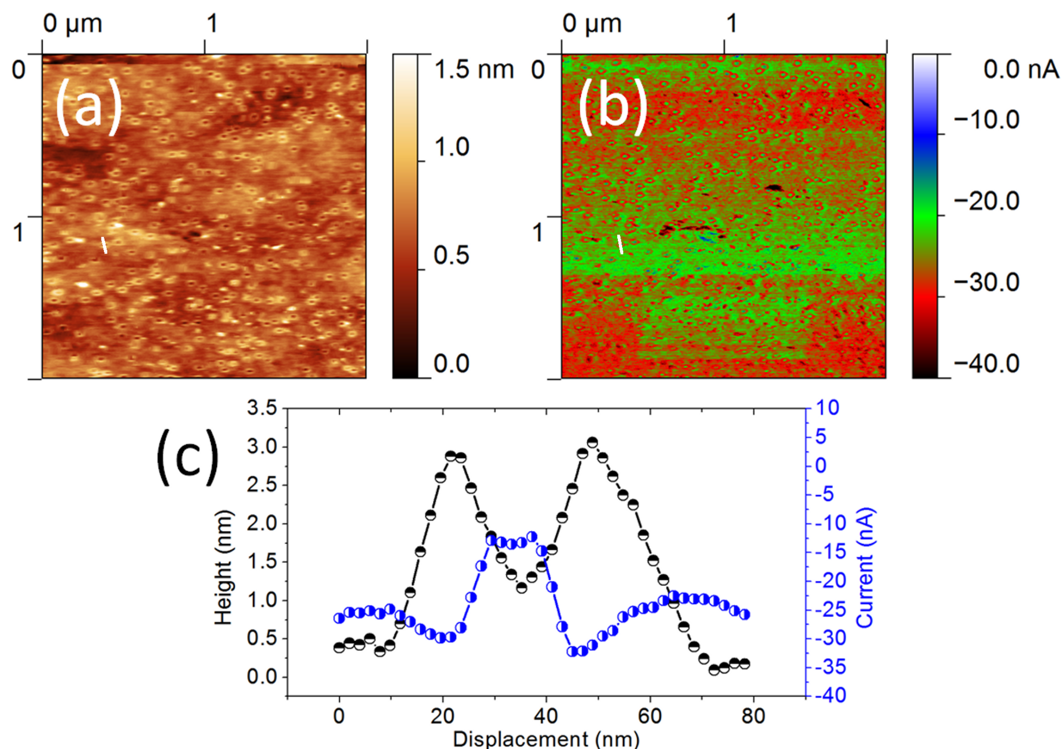

Figure 3.12 C-AFM images of InGaAs quantum rings recorded in UHV: topography (a), current map (b) and corresponding cross-sections (c) recorded along the white lines marked in (a) and (b). The images were acquired in contact mode AFM at -2 V of sample bias.

2D autocorrelation map analysis

Ring structures as the one under consideration are a challenge for C-AFM since the resolution of the technique relies to a high extent on the electrical properties and geometry of the conductive probe used. We analyzed the topography image and the corresponding current map utilizing 2D ACM. The advantage of this kind of representation is its statistical character. The 2D ACM reflects the peculiarities common to all the QRs present on the surface in contrast to profiling of a particular QR. This helps to increase the accuracy and reduces influence of artifacts due to the local character of the measurement.

The 2D ACM of the topography image is presented in Fig. 3.13(a). There, the zero point corresponds to the central bright spot in the center of the image. The structure observed in the 2D ACM has elliptical shape and - as mentioned above - originates from measurement artifacts. The diameter d of the QRs has been determined from the distance between the central 0-order peak and the 1st-order peak along the ACM cross-section taken at 45° with respect to the scan line direction. The same procedure has been applied also to 2D ACM of the corresponding current map and presented in Fig. 3.13(b). The fact that the cross

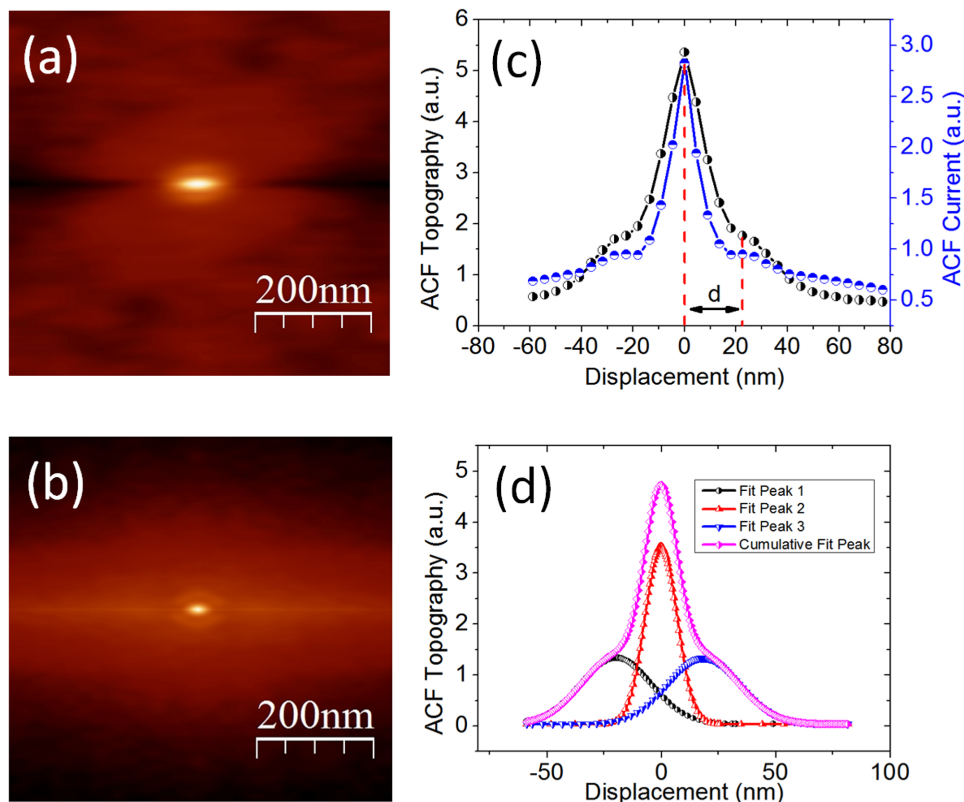

Figure 3.13 2D autocorrelation maps of the topography (a) and corresponding current map (b) recorded in contact mode AFM at -2 V sample bias. A comparison of the topography and current map ACM cross-sections (c) taken at 45° with respect to the fast scan line direction. A possible decomposition of the topography ACM cross-section into several peaks is presented in (d).

sections of the ACM were taken at 45° does not entirely eliminate the artifact's influence, but helps to improve the accuracy of the measured distances.

Correlation between the topography and current ACM cross-sections. A comparison of the ACM cross-sections taken from the same location at the topography image and the corresponding current map is presented in Fig. 3.13(c). The diameter determined from the cross-sections directly (without any post-processing) equaled to 22 nm. In fact, with the tips in use one can achieve resolution in the nanometer range on flat surfaces since their granular coating consist of small diamond grains with size of a few nanometers. Therefore, the resolution relies significantly on the geometry of the "last" grain at the tip ending. This situation is schematically depicted in Fig. 3.14 (a). In the present case, we can judge about the probe conditions only by implication, in particular on the basis of ACM cross-sections. A comparison of the topography and current map ACM cross-sections reveals that the current

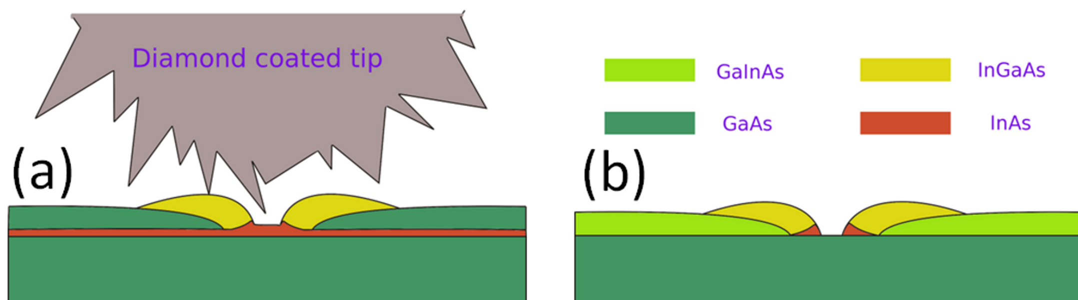

Figure 3.14 Schematic drawings of the C-AFM measurement of QRs performed using diamond coated tip (a), and possible compositional distribution within a single InGaAs QR (b).

reaches its maximum simultaneously, in this case, with reaching the maximum of the height of the QR's rim.

ACM cross-section peak fitting. In order to resolve the peaks attributed to the current and topography maxima we performed a peak fitting procedure, the results are presented in Fig. 3.13(d). The separate peaks were fitted by Gaussian functions, the cumulative peak exactly reproduces the shape of the original topography ACM cross-section. The diameter determined from the distance between the fitted peaks equaled to 18 nm, which is ∼4 nm smaller than the value determined from the original cross-section. Thus, the actual diameter of the QRs may be slightly smaller than the diameter determined directly from the AFM topography profiles.

The effect of residuals on the current maps

It has been noticed that the presence of residuals of As_4 on the surface may lead to tip contamination and alter the current flow. In many cases, the current flow has been interrupted. This situation could be solved preferentially by tip replacement. Interestingly, the presence of As_4 residuals may also lead to a local current increase. Such a situation is depicted in Fig. 3.15. The presented topography and corresponding current maps are taken from different regions of the sample with the same tip. The images presented in Fig. 3.15 have been recorded at -2 V of sample bias. The current maps reveal increase of conductivity for the contaminated areas due to lowering of the barrier height. Nevertheless, the current map still reveals the contrast from the quantum ring regions, where the ring has a higher conductivity compared to the central hole and the surrounding.

Conclusions

To summarize, the correlation between the current maxima and topography peculiarities can be better visualized and quantitatively characterized using cross-sectional analysis of the

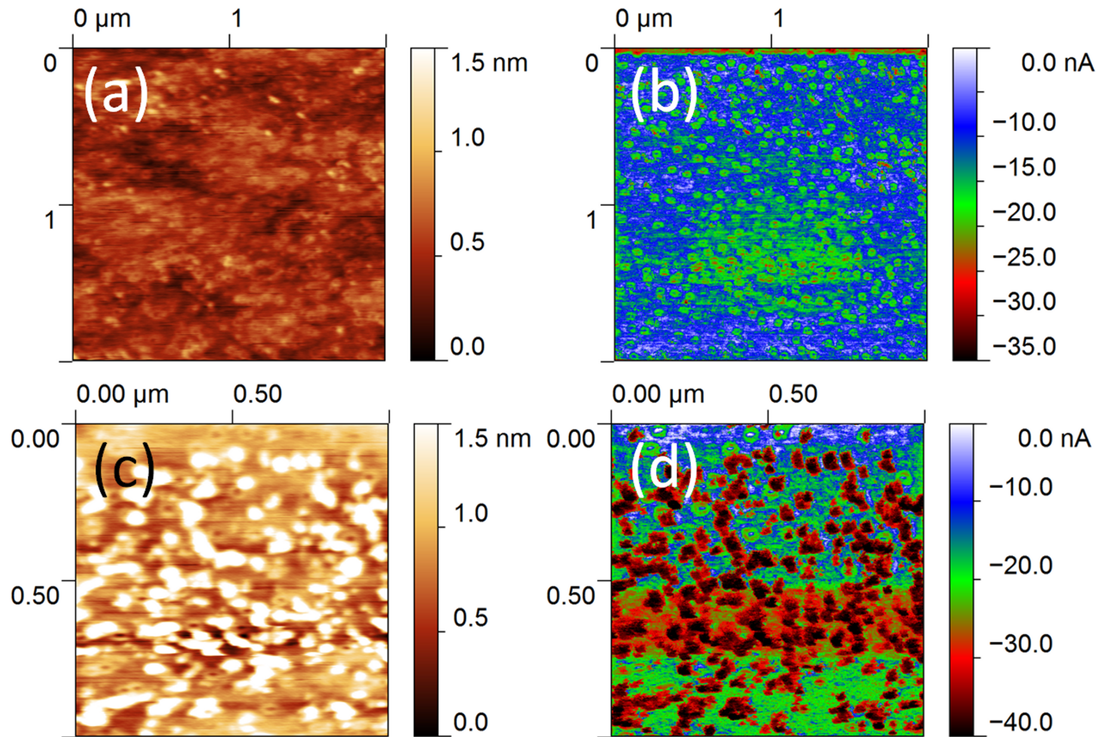

Figure 3.15 The effect of As_4 residuals on the topography and current maps. The images acquired in contact mode AFM at -2 V of sample bias. 2 μm×2 μm and 1 μm×1 μm topography images (a,c) with the corresponding current maps (b,d) were recorded from the same sample after the first cycle of uncapping.

corresponding 2D ACM. A peak fitting procedure can additionally be employed in order to improve the accuracy of the analysis. Its application to the QRs compositional analysis, the comparison of the topography and current map ACM cross-sections reveals a straightforward correlation between the topography and current, where the current and topography maxima coincide. Relying solely on the C-AFM results this can be interpreted in terms of higher In content within the QRs. Contrariwise, the compositional analysis performed via other techniques mentioned above suggests that the central hole of the QRs is the region with the highest In concentration.

To our opinion, a possible source of the difference between C-AFM data (both, recorded under ambient conditions and in UHV) and data obtained by other techniques mentioned above is probably a too large probe radius used in C-AFM experiments. One of the possibilities to overcome this problem is to use much sharper conductive probes. The best instances of the commercially available conductive probes possessed a tip radius of $\sim$ 30 nm at the time when C-AFM experiments on the InGaAs QRs have been actively performed in our lab which was still not sufficient to reach the desired resolution. As for now, a new attempt can be made using probes with the attached conductive whiskers which just recently be-

came commercially available (e.g. CSC05_10° from NT-MDT^{TM}). Another possibility is to combine the action of a high tip loading force with the advantages of modern all-diamond probes with the guaranteed tip radius of $\sim$ 50 nm or smaller. However, such an imaging conditions need an additional investigation. A further possibility to clarify this issue would be to investigate larger QRs where the large tip radius has less impact.

The analysis of the topography and corresponding current maps obtained during C-AFM experiment provides sufficient evidences to conclude that the spatial resolution of the technique is high enough to resolve the central hole of the QRs. An additional confirmation can be obtained from detailed examinations of the current profiles. The situation when the central hole of the QRs appears less conductive is possible only in the case when the tip has no contact with the more conductive outer rim. This condition implies in turn that in our case the tip has a reasonably good electrical contact to the central hole of the QRs. Therefore, we can conclude that the observable contrast is unaltered and the content of In is smaller in the central hole compared to the ring. This situation is schematically depicted in Fig. 3.14. Moreover, the high conductivity of the matrix compared to the QRs' can be assigned to the intermixing of the InAs wetting layer with the GaAs capping layer.

Chapter 4

Results II: Electrical properties of defects in GaInP epitaxial layers on Ge

The present chapter is based on the results published in Ref. [1] from the publications list.

The growth of III-V semiconductor devices on Ge substrates has received considerable attention, particularly in the field of photovoltaic cells [97], first for space aspects and more recently for terrestrial high concentrator applications [98]. The main reason for this fact is that germanium has a small lattice mismatch with GaAs. Additionally, germanium offers clear advantages over conventional GaAs substrates in certain applications such as high crystallographic perfection, high mechanical strength, slightly higher thermal conductance, and lower cost; also, germanium is an environmental friendly substrate easy to recycle.

The prosperous usage of this approach, however, is often limited by the presence of defects, such as Antiphase Domains (APD) and Arrowhead Defects (ADs) [99], which diminish the quality of the overgrown epitaxial layers and account for the loss of conversion efficiency. Previous morphological and compositional investigations [99] of GaInP thin films, grown by Metalorganic Vapor Phase Epitaxy (MOVPE) on Ge (100) misoriented by 6° towards (111), have revealed the presence of two sorts of defects on the surface of the epilayer: on the one hand, truncated asymmetric pyramids, similar to the findings of Chapman and Lankinen [100, 101] and, on the other hand, ADs [99]. It has been found that the density of the latter increases as the layer gets more Ga-rich, while the density of the truncated pyramids, in turn, did not demonstrate any dependence on the layer composition.

Additionally, the composition and quality of GaInP/Ge epilayers were also investigated by means of high resolution x-ray diffraction but no conclusions related to variations in the defect composition could be achieved. In other studies, a deeper analysis of the truncated asymmetric pyramids was carried out, although neither compositional study of arrowheads nor characterization of their electrical properties were performed [100, 101]. C-AFM, I-V spectroscopy, and KPFM are suitable techniques to extract electrical properties related to

the ADs since they operate on the nanometer scale.

Previous investigations using KPFM measurements [102] and I-V characteristics achieved from C-AFM measurements [103] have revealed that both techniques are sensitive to variations in the degree of GaInP ordering. The ordering is described as the alternation of (111) planes consisting of either Ga or In atoms on the group III sublattice [104]. This gives rise to an ordered CuPt -type structure, which results in a narrowing of the band gap of the material, whose exact value depends on the degree of ordering. Reductions above 100 meV can appear. The ordering depends on growth conditions and substrate preparation.

4.1 Sample preparation: MOVPE growth

The samples have been grown by our collaborators at the Instituto de Ciencia de Materiales de Madrid, Spain using MOVPE in a 2 in. AIX200 horizontal reactor system. The substrates used were p-type Ge wafers 150 μm thick, (100) oriented with a miscut of 6° off toward the nearest (111) plane. Typically, the MOVPE growth process took place at a temperature of 640 °C, a pressure of 100 mbars and with a total flow of 14 slpm of palladium-purified hydrogen. The precursors used were pure PH_3, AsH_3, trimethylgallium (TMGa), and trimethylindium (TMIn). The growth routine is based on four steps, namely:

- Ge substrate annealing at high temperature (700 °C) to form a double atomic height step structure
- P monolayer deposition at 700 °C to achieve a single domain surface
- deposition of a thick, nominally undoped GaInP layer lattice matched to Ge (ranging from 600 to 1000 nm) at T=640 °C, $V/III = 120$, and growth rate equal to 2 μm/h
- deposition of a thin GaAs capping layer of around 100 nm, which was chemically etched before all measurements using HF solution.

4.2 Structural properties of GaInP layers

Prior to investigation of electrical properties the surface topography was examined with a Digital Instruments Nanoscope™IIIa AFM operating in Tapping Mode™ under ambient conditions. The images in this mode have been recorded with Nanosensors™ SuperSharpSilicon™ AFM probes (SSS-NCHR) with the tip radius as low as 2 nm; the half cone angle at ∼200 nm from apex ∼10°; the resonance frequency was typically ∼300 kHz.

The surface morphology of the GaInP containing the arrowhead defects is depicted in Fig. 4.1(a). The ADs are clearly recognized in the 3D AFM image by two rather smooth triangular side planes (named here as L and R planes). The typical width of the ADs is in the range from 400 nm to 3 μm, while the corresponding height varies from 10 to 170 nm. It is significant that the ADs are always pointing to the $[01\bar{1}]$ direction, i.e., the same as

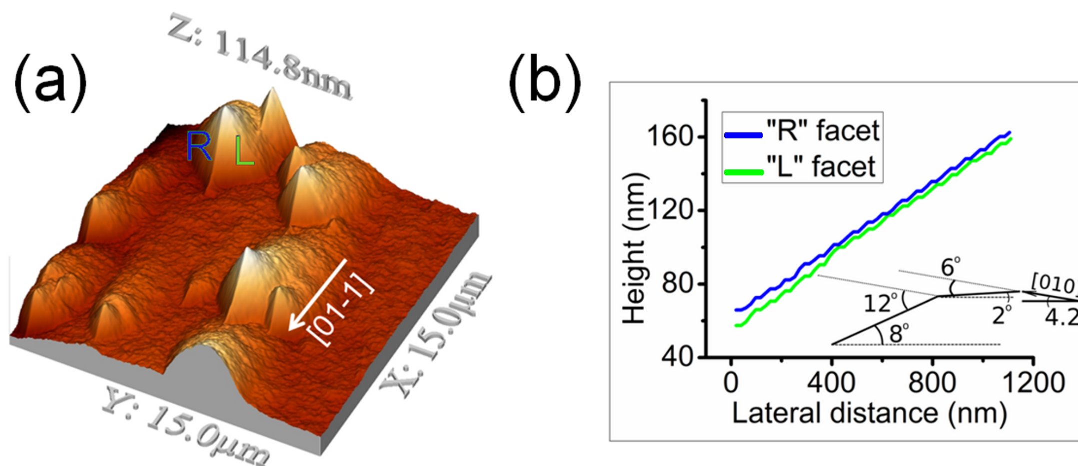

Figure 4.1 3D AFM image of arrowhead defects on the surface of InGaP/Ge(100) (a) recorded in intermittent contact mode. Analysis of the cross-sectional profiles taken along [001] and [0$\bar{1}$0], respectively, reveals that both terminating planes (L and R) are composed of alternating facets of {105} and {109} type, which are tilted with respect to (100) by about 12° and 6°, respectively (b) (From [35]).

the step flow direction, and the film exhibits a good crystallinity [99]. The overall rms film roughness is ~32 nm for a 100 μm^2 representative central area of the sample.

4.3 Electrical properties of the arrowhead defects

4.3.1 C-AFM study

Experimental details

C-AFM measurements were carried out under ultrahigh vacuum conditions with a base pressure of 5×10^{-9} mbar. Prior to C-AFM measurements, the samples were held in the load lock chamber for up to 10 h at a temperature of 70 °C, and a base pressure of 5×10^{-6} mbar, in order to degas and remove the water physisorption layer. In the course of C-AFM measurements, we used DCP11 diamond coated (heavily doped with nitrogen) tips from NT-MDT™, and the cantilever force constant varied in the range from 3 to 10 N/m. The tip radius curvature is 50-70 nm, but the grain structure of the coating makes it possible to resolve features with sizes below 10 nm laterally. The resistivity of the tip coating is 0.51 Ω·cm.

2D current maps

Figure 4.2 represents the morphology (a) of the AD obtained simultaneously with the data on local conductivity (b) under UHV conditions in contact mode acquired at -3 V of sample bias on the surface of the GaInP/Ge sample. The topography image appears a bit blurred in

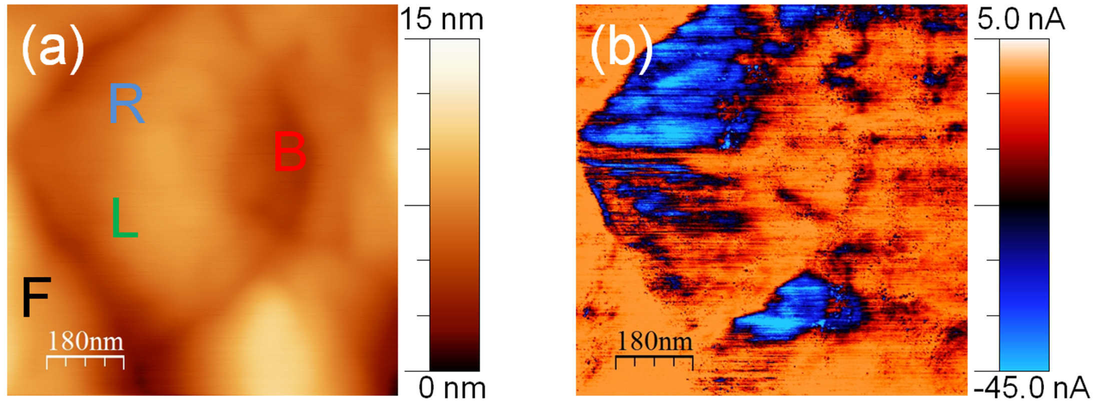

Figure 4.2 C-AFM investigation of arrow head defects. Morphology image (a) and corresponding two dimensional current map recorded at -3 V (b). The current map of the arrowhead defect reveals a different conductivity for (L) and (R) terminating planes. (F) and (B) denote the surrounding film and the back side of the AD, respectively.

comparison to images obtained in tapping mode, mainly because of the higher forces acting in the C-AFM mode. This leads to a larger contact area between the tip and the surface, resulting finally in a decrease of resolution. As one can see in Fig. 4.2 (b), the distribution of the currents is inhomogeneous and it differs significantly for the L and R terminating planes. In order to extract quantitative information, the current density for each plane and the surrounding area has been calculated. The current densities for the L and R planes amount to (-278±35) and (-445±35) μA/m^2, respectively, calculated in average for 0.1 μm^2 of the projected area close to the AD apex and a bias of -3 V. The values for the surrounding film and the back side of the AD are (-20±35) and (-40±35) μA/m^2, respectively.

I-V Characterization

In order to extract more information, current-to-voltage characterization has also been carried out (Fig. 4.3. The characterization was performed with a bias sweep in the range of 10 V, and the measured current varied from 0 to 50 nA. As it can be observed, all curves exhibit a rectifying behavior, although the L plane characteristic differs from the R plane and the defect free surface of GaInP.

4.3.2 KPFM study

Experimental details

In order to gain further insight into the electrical properties of the AD, we performed Kelvin probe force microscopy measurements of the same sample using $PtIr_5$ coated AFM probes. The topography together with the corresponding CPD (bucking voltage) map is depicted

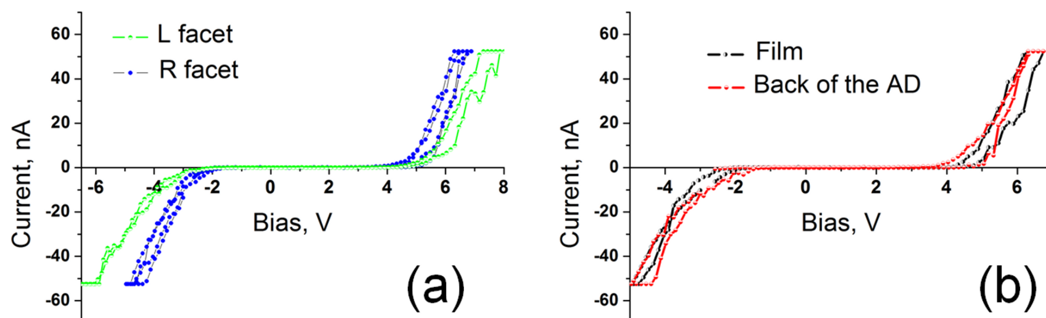

Figure 4.3 Current-voltage curves recorded for several (L) and (R) planes of the arrowhead defects (a), surrounding film (F) and the back side (B) of the AD (b). The I-V curves exhibit degradation of the conductivity for the (L) facet relative to the (R) facet.

in Fig. 4.4. One of the problems in KPFM is the strong electrostatic interaction between

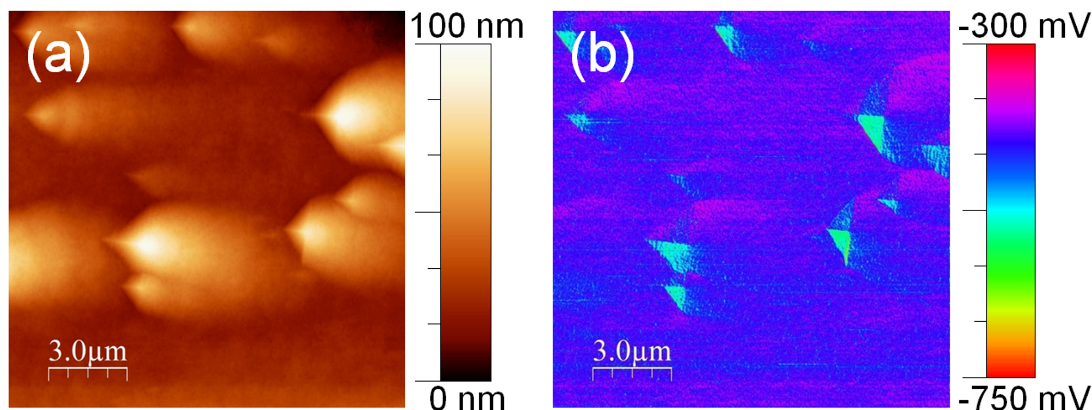

Figure 4.4 KPFM results representing topography (a) simultaneously acquired with the bucking voltage (b) of the ADs. While the value of the contact potential difference for the (L) plane differs by ~70 meV from the value found for the surrounding, no difference for the (R) plane was observed.

cantilever and sample surface resulting in a strong dependence of the bucking voltage (tip bias which is used to nullify the tip-to-sample electric interaction applied simultaneously with the excitation signal; ideally the bucking voltage is equal to CPD) on the voltage of the electrical excitation (V_{AC}). Therefore, the determined values for the CPD have to be considered as a rough estimation. It is customary in KPFM to use bucking voltages rather than the values of CPD, especially in the cases when the determination of the real values of CPD is not possible. The images represent measurements in one certain tip-to-sample geometry. Measurements were performed also in different relative tip-to-sample orientations with the same result. Since the KPFM measurements were performed under ambient conditions, not all influences

on the work function of the surface can be filtered out. The values of the Bucking Voltage (BV) at V_{AC} = 5 V average to ∼525 meV for the L plane and ∼455 meV for the R plane. The R plane value differs from the surrounding film by about 40 meV. At higher excitation voltages V_{AC}, we observed an increase in the difference between the bucking voltages for the L plane and the rest of the film. The difference increased up to 300 meV at V_{AC} = 9 V. At the same moment, we observed a positive shift in the bucking voltages for the surface in general.

4.3.3 Analysis and discussion of the obtained results

In the following, the possible explanations for the experimental observations are discussed. First, we focus on the tip-sample contact properties [45]. A certain issue is the tip contact area, which alters coincidentally with the change in the relative tip-to-surface tilt angle. We were able to eliminate this factor by measuring the sample in different in-plane orientations, which also led to unalterable contrast in the current map. The effective electrical contact area A_{eff} was estimated to [63]:

$$A_{eff} = \pi r_{cont}^2 \tag{4.1}$$

$$r_{cont}^3 = \frac{3}{4}(k_1 + k_2) F_{ts} R_{tip} \tag{4.2}$$

where F_{ts} is the tip-sample force, r_{cont} is the tip-sample contact radius, and k_i is given by $k_i = \frac{1-\nu_i}{E_i}$ with ν_i and E_i are Poissons ratios and Youngs moduli of the tip and sample, respectively. During the course of the measurements, the tip-to-sample force was equal or higher than 100 nN and the tip apex radius was taken equal to 50 nm. With these estimates, the tip-sample contact radius is ∼1.5 nm and therefore, the tip-sample contact area is ∼7 nm^2. According to the literature, a stable tip-sample contact is achieved at the above mentioned conditions [105].

Second we discuss the physical origin of our observations. Several possible mechanisms have to be considered when speculating on the origin of the different values of conductivity for the terminating L and R planes. First, the electrical properties (band gap, carrier concentration, etc.) of the bulk below the tip-sample contact have to be considered. The variation in composition of the AD can significantly differ from its surrounding causing shifts in the band gap and position of the Fermi level. However, we think that variations in the composition between the AD and its surrounding would lead to a less pronounced effect in the current map than that which has been observed. Another concern is the obvious difference in the electrical properties of the two terminating planes which cannot be explained simply in terms of compositional difference. At this point the possible influence of surface contaminations has to be discussed. Sample heating in the load lock of our UHV system upon 70 °C at 5×10^{-6} mbar for several hours will indeed remove water from the sample surface but might not be sufficient to remove contaminations such as surface oxides or hydrocarbon layers. This might result in a change of conductivity due to the fact that the contact is formed between the conductive tip and the contamination layer. In the case of a native

oxide layer, this contamination layer would be 0.9 nm thick under the applied preparation conditions [106].

For the current maps, which are recorded in contact mode under high tip loads, the coincidence of the measured currents obtained for both scan directions, trace and retrace, however indicates that there is no significant influence of a contamination layer. Otherwise the tip should cause a change in the layer during the trace cycle due to scratching the layer or stripping off contaminations, which would lead to different electrical tip-sample contact for the retrace direction. It is known from the literature that the impurity incorporation and activation as well as the affinity to adsorbates depend on the crystallographic orientation [107, 108], which then might also lead to orientation dependent electrical properties.

Since both planes are assumed to be of {105} type and therefore are crystallographically equivalent, this seems unlikely in the present case. Additionally, the GaInP layer is nominally undoped and the background doping in MOVPE is just around 10^{16} cm^{-3}, which makes doping effects also unlikely. According to Lee et al. [103], the higher conductivity of the GaInP can be explained by a higher degree of order in the epilayer. It is also known that epitaxially grown GaInP exhibits the tendency for CuPt-type ordering [104], resulting in a band gap shrinkage and Fermi level pinning in ordered GaInP [102]. In fact, we can assume that the increase of conductivity for the AD is caused by ordering, which is consistent with the concept of band gap shrinkage. The differences in the I-V characteristics can be explained in terms of the degree of order in the material under the two terminating facets. The degree of order is hard to determine just on the basis of the electrical characteristics, but at least some qualitative conclusions can be made. According to Lee et al. [103], an improvement in the I-V characteristics (high breakdown voltage and low leakage current) implies a lower degree of order. This fact is related to the existence of Antiphase Borders (APB) in ordered materials which act as scattering and/or recombination centers [109], inducing degraded I-V characteristics in ordered material [103]. According to the foregoing phenomenology, the R facet has a higher degree of order.

On closer inspection, the current is concentrated within confined areas of ∼5-10 nm in their lateral dimensions, seen as small blue spots in Fig. 4.2 (b), which could correspond to the ordered domains. This is supported by the fact that, in general, for III-V ternary alloys there is a preference for short-range ordering [110, 111]. However, a long range ordering may also appear spontaneously during epitaxial growth of those materials [112].

Besides the main observation discussed above, we found also a lowering in current measured from the sharp edge separating the L and R planes of the AD. This behavior is unusual since one would expect higher currents due to the field enhancement at the sharp edge. Also in some I-V curves we found a small hysteresis (which is seen as a small separation between a pair of I-V characteristics depicted in blue color in Fig. 4.3) at higher, positive voltages, while the negative voltage region remains preferentially stable over the whole range. The absence of hysteresis can serve here as an indication of a stable tip-sample contact, without oxide layer formation during the voltage ramping.

The KPFM data are in a reasonable agreement with the data obtained by C-AFM, because a higher value of BV corresponds to the case of lower conductivities for the L facet.

For the analysis of the data, we can exclude an influence of different surface roughness on the KPFM CPD map, based on the facet analysis of the terminating planes which reveals that both planes exhibit equivalent surface profiles (taken along the [010] and [001] directions, Fig. 4.1(b)). The planes are composed from {105} facets with a width of (43±9) nm alternating with 20 nm wide high-index {10n} planes. Within the limits achievable in conventional AFM, n was determined to be about 9. This suggests that the distinctive behavior of the terminating planes originates in surface properties, namely, the difference in work function due to the different surface termination on the L and R planes. According to the model proposed by Baxter et al. [113], the ordering structure consists of two interlocking variants (occurring in the $[1\bar{1}1]$ and $[11\bar{1}]$ directions for GaInP (Ref. [104])) on nearly atomic scale in the [001] direction, which could also lead - in the case of ADs - to a different surface termination. Since the KPFM measurements were carried out under ambient conditions, it has to be pointed out here that an influence of adsorbed species on the local work function cannot be excluded.

For solar cell applications, the existence of APBs implies a degradation of the minority carrier lifetime as result of additional recombination mechanisms, which leads to a drop in the photocurrent generation. According to our results, the conductivity of the ADs is higher than that of the defect free film. Therefore, the ADs can act as a shunt resistance provoking internal shortcuts resulting in a decrease of the open circuit voltage. Thus the formation of ADs will weaken the solar cell performance.

In summary, we have measured the surface morphology of arrowhead defects forming in GaInP epitaxial layers grown on vicinal Ge(100) and performed electrical characterization by means of C-AFM and KPFM. The terminating planes of the AD have been found to be composed from two alternating sub-planes which are about 12° and 6° inclined towards the (100) plane corresponding most likely to {105} and {109} facets. The topographical analysis of the ADs suggests that the terminating planes are morphologically identical. At the same time, we observed that the electrical behavior of the ADs significantly differs from the behavior of the defect-free surface. Interestingly, the terminating planes appear different relative to each other with respect to their electrical properties both in C-AFM and KPFM. Specifically, the current densities (C-AFM) for the two terminating planes amount to (-278±35) and (-445±35) μA/m^2, respectively, while this value drops to (-20±35) μA/m^2 for the defect-free surface. In turn, the BV (KPFM) value for the ADs differs from the value for the surrounding film up to ~100 meV (L plane). According to Leng et al. [102] and and Lee et al. [103], we conclude that the ADs in GaInP/Ge are composed most likely from material with a higher degree of order. However, the origin of the bucking voltage difference between the AD and its surrounding is still an open question.

Chapter 5

Results III: ZnO nanorods

The present chapter is based on the results published in Ref. [4, 11, 12] from the publications list.

ZnO nanostructures are promising candidates for the development of novel electronic devices due to their unique electrical and optical properties. In particular ZnO nanostructures as upright standing ZnO NRs show future prospects for a wide range of next-generation electronic and opto-electronic devices. Fields of application involve solar cells [12, 114–116], piezo-actuators, and energy harvesting devices [10]. Regardless of the mechanism of photoconductivity in ZnO, it is intensely proposed as a UV-sensor material in several configurations [117–126]. The surface conductivity of ZnO is highly dependent on the presence of adsorbates on its surface. Such surface defects serve as binding sites for chemisorption processes and may contribute to the scattering and trapping of carriers [127] which lower the intrinsic conductivity of the material. Here, we present a study of individual upright standing ZnO nanorods grown by hydrothermal and thermal evaporation methods in terms of their electrical and optical properties by means of C-AFM and PC-AFM. The applicability of PC-AFM to the local opto-electrical characterization of semiconductor nanostructures and surfaces is demonstrated.

The nanorods have been grown on Si(100) and Fluorine-doped Tin Oxide (FTO) substrates by two methods, namely thermal evaporation and hydrothermal growth. Measurements were performed in air and nitrogen atmosphere at variable temperatures. The current-voltage spectroscopy on the individual upright standing nanorods, taken with diamond coated, conductive tips revealed a characteristic similar to that of a p-n diode. The analysis of the I-V characteristics in terms of Schottky barrier formation is presented in Sec. 5.4.4.

Detailed discussion of the optoelectrical properties is based on local I-V curves, measured under- and without illumination, as well as on the transient photocurrent behavior and photocurrent spectroscopy.

5.1 Synthesis of ZnO NRs

The synthesis of the ZnO nanorods has been performed by the group of Prof. Alexandra Djurišič from University of Hong Kong, P.R. China, employing two fabrication routs.

Thermal evaporation (TE) For rods fabricated by Thermal Evaporation (TE), the fluorine-doped tin oxide (FTO)/quartz substrate was placed in dry argon flow 1.5 cm above the Zn source (0.2 g, Aldrich, 99.995%). The reaction was performed in a horizontal tube furnace with a base pressure (no gas flow) of $\sim 10^{-2}\ Torr$. Prior to growth, the furnace was flushed with 0.1 L/min of argon. When the furnace reached 500 $°C$, a flow of 0.01 L/min oxygen gas was added. The pressure during growth was 1.1 Torr, the reaction time was 70 min [14].

Hydrothermal growth (HT) For Hydrothermal Growth (HT), a seed layer was prepared using zinc acetate solution and annealed at 350 °C. The fluorine-doped tin oxide (FTO)/quartz substrates covered with the seed layer were then placed upside down in a 75 mL aqueous growth solution containing 0.1 g polyethylene (Aldrich, 50 wt% in water), 25 mM zinc nitrate hydrate (Aldrich, 99.999%), and hexamethylenetetramine (Aldrich, 99+%). The reaction time was 10 h, with the replacement of fresh solution every 2.5 h.

5.2 Characterization of the morphology

For imaging of semiconductor NRs, so far mainly Scanning Electron Microscopy (SEM) and TEM have been used. However, it was demonstrated recently that AFM in tapping mode also yields reliable information on the NR morphology [36, 128], including information on transition facets between the (0001) top and $\{10\bar{1}0\}$ side facets. Prior to electrical investigations, the morphology of the ZnO NRs has been pre-characterized by means of intermittent contact mode AFM. For these measurements we used PPP-NCHR cantilevers with force constants varying from 10 to 130 N/m. In Fig. 5.1, topographies of the TE (a) and HT (b) samples are presented. ZnO NR diameters vary in a wide range from 150 nm to 1.2 μm for the TE grown sample whereas the rods of the HT grown sample are significantly smaller in diameter (20-80 nm). Rod lengths of TE are $\sim$1.5 μm as determined from SEM (see inset in Fig. 5.1). The height distributions corresponding to the topography images presented in Fig. 5.1 are shown in Fig. 5.2 (a) and (b), respectively. In both cases the height distributions are rather uniform, the average ZnO NRs height determined from the height distribution is $\sim$1.1 μm for the TE grown sample and is $\sim$300 nm for the hydrothermally grown one. The later value is due to the fact that the AFM tip does not reach the substrate. Thus, the value does not reflect the height of the NRs which is much larger.

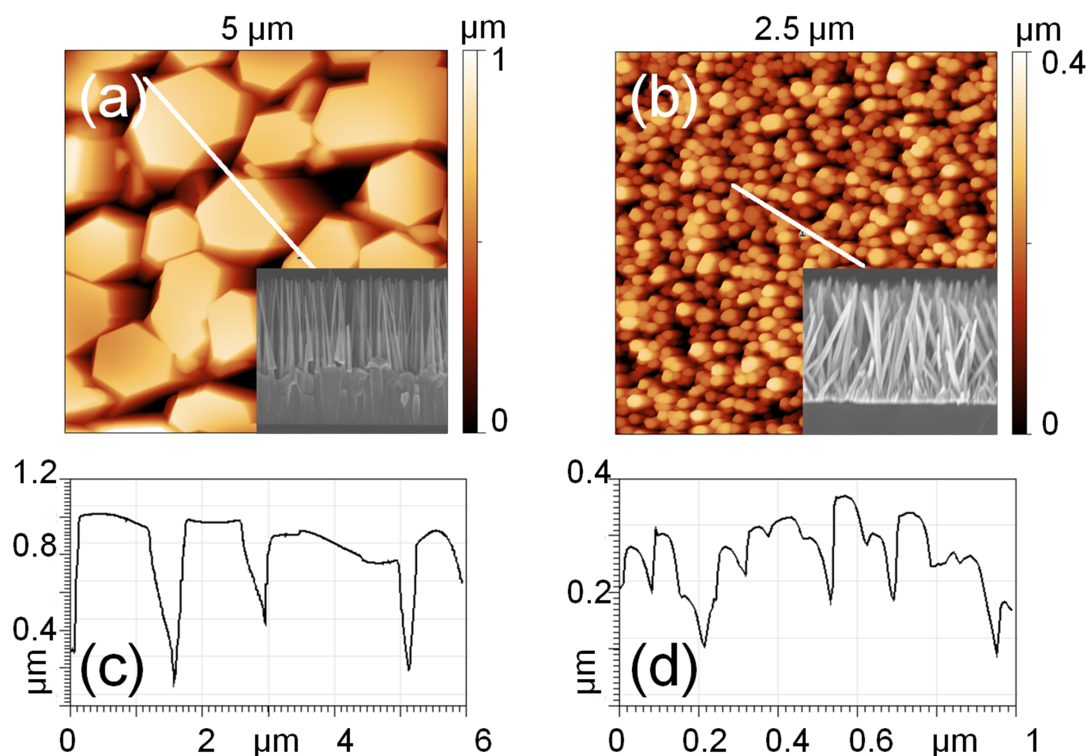

Figure 5.1 5 μm×5 μm intermittent contact mode image of ZnO nanorods grown by TE (a) and 2.5 μm×2.5 μm tapping mode image of HT grown samples (b) with the corresponding cross-sections depicted in (c) and (d).

5.2.1 Structural characterization

Experimental details

The morphology of the arrays of upright standing ZnO NRs was studied by means of SEM and intermittent contact mode AFM using PPP-NCHR probes from Nanosensors™ with a cantilever resonance frequency of $\sim$ 330 kHz. For additional characterization of the ZnO NRs' crystallographic properties as well as their orientation, X-ray Diffraction (XRD) measurements were performed. We recorded the XRD-spectra of the ZnO NRs by performing ω-2θ-scans perpendicular to the sample surface using a standard lab diffractometer with an analyzing crystal in front of the detector at 1.54 Å x-ray wavelength.

Discovered structural peculiarities

Fig. 5.3 summarizes the structural properties of the ZnO NR array. The sample's morphology is presented in the intermittent contact mode AFM image (Fig. 5.3(a)). We observe NRs with hexagonal cross-section and diameters in the range from 150 to 1200 nm. Along with exactly upright standing NRs one can find rods which are significantly tilted with respect to

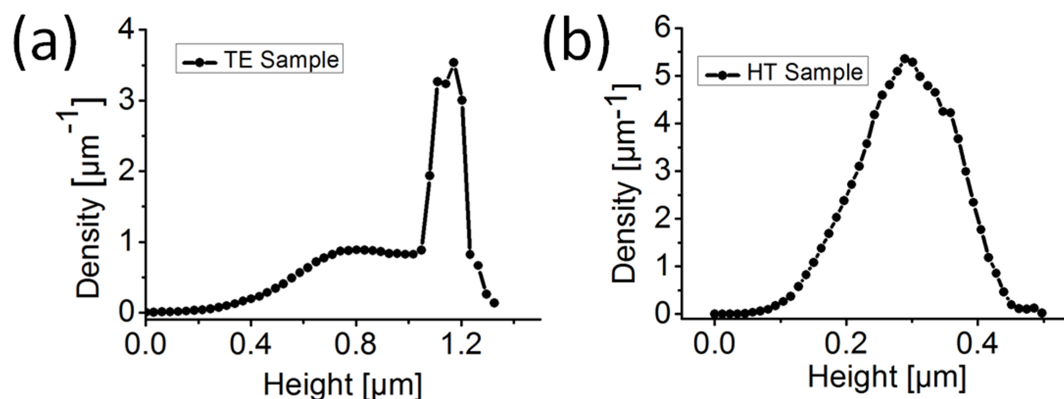

Figure 5.2 Height distribution plots of (a) TE and (b) HT sample taken from the 10 μm intermittent contact mode AFM images of arrays of upright standing ZnO NRs grown on FTO.

the substrate. The crystallographic orientation of the vertically aligned planes is difficult to define solely from the AFM measurements. However, the tilted side planes are sometimes composed of step bunches separated by (0001) facets which can easily be distinguished from the rest. The height of the steps (Fig. 5.9) on the side plane ranges from 22 to 30 nm. The protruding part of the (0001) facet at the steps of the side planes has a width of about 1-2 nm. The difference in the electrical properties between top and side planes of the ZnO NRs was one of the key issues examined in the present investigation. In order to have an easier access to both the top and side planes, we dealt preferentially with NRs where the side plane is represented by a number of steps bunches instead of one crystallographic facet. Such a structure may be also of interest for some practical applications.

In Fig. 5.3(c) the section of the XRD-spectrum between the $(10\bar{1}0)$ and the $(20\bar{2}2)$ Bragg peak of ZnO is shown as a function of the reciprocal lattice vector q_z along to the [0001] direction. The peak positions of bulk wurtzite ZnO with a=3.250 Å and c=5.207 Å hexagonal lattice constants are marked by dashed lines and the theoretical peak intensities are indicated by crosses. These positions show excellent correspondence to the measured ones proving unstrained crystalline ZnO NRs. (The peaks which have not been indexed can be related to the substrate material.) Furthermore, we compared the measured integrated peak intensities with the theoretical values for a powder like distribution of ZnO. We found that, e.g., the hexagonal (0002) ZnO peak depicted a 180 times higher intensity as expected for random oriented nanorods, indicating that a majority of ZnO NRs is oriented with the c-planes parallel to the sample surface. We could detect only one other preferred lattice plane along the surface normal, i.e. the $(10\bar{1}3)$ plane with $\sim$4 times higher intensity. Assuming a constant volume for all ZnO NRs we can estimate from all intensity values that 93% of the NRs are aligned with the c-axis along the surface normal. However, 4% are aligned parallel to the $(10\bar{1}3)$ planes of the ZnO NRs, i.e., they are tilted by 28.1° to the sample surface. In fact in our previous AFM study of ZnO NR arrays we already observed the existence of - in such

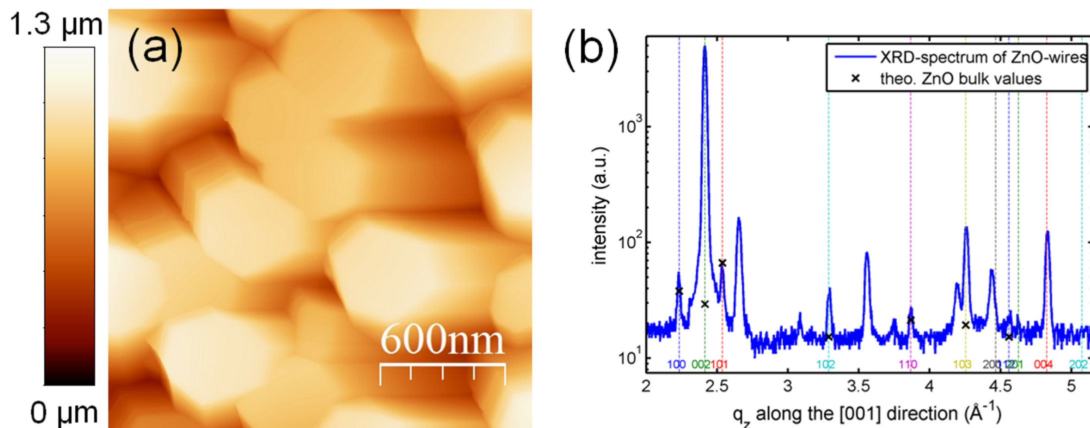

Figure 5.3 (a) Intermittent contact mode AFM image of ZnO NRs grown on FTO. The diameter of the ZnO varied in a wide range from 150 to 1200 nm, the length of the NRs was $\sim 2.5\ \mu m$ as it was determined from the comparison of SEM and AFM data. (b) XRD spectrum of the ZnO NRs perpendicular to the sample surface. XRD intensity over the reciprocal lattice vector q_z along the [0001] direction. ZnO bulk Bragg peak positions and intensities are marked as dashed lines and crosses, respectively.

a way oriented - $\{10\bar{1}3\}$ intermediate facets between the steep $\{10\bar{1}0\}$ side facets and the (0001) top [128]. All other orientation directions are found to contribute below ~1%.

5.3 Time-resolved photoluminescence spectroscopy

ZnO NRs have been also characterized macroscopically by means of Time-Resolved Photo Luminescence (TR-PL). The conventional steady-state Photoluminescence (PL) and TR-PL were measured at 300 K. The monochromator used for both types of PL experiments has a linear dispersion of 0.8 nm/mm and was equipped with a photomultiplier tube as photodetector. The setup for the time-resolved PL experiments utilizes a stroboscopic oscilloscope with 0.1 ns gating registration system. As a source of optical excitation for PL measurements, we used the 337.1 nm emission line of a nitrogen laser with a pulse duration of 8 ns and a repetition rate of 100 Hz. PL emission was detected during the laser excitation pulse either at the leading edge of the laser excitation pulse (starting from ~0.7 ns after the pulse onset), or at the trailing edge of the laser pulse after a variable delay time, t_{del}, with respect to the onset of the laser pulse.

The spectral dependencies of the time-resolved spectra of photoluminescence of a ZnO NR array recorded using the 337 nm line of a pulsed nitrogen laser are presented in Fig. 5.4. The TR-PL spectra presented in Fig. 5.4 reveal both band-edge and defect emission. A strong peak at 383 nm (3.2 eV) which occurs within 0-0.7 ns after onset of the excitation pulse can

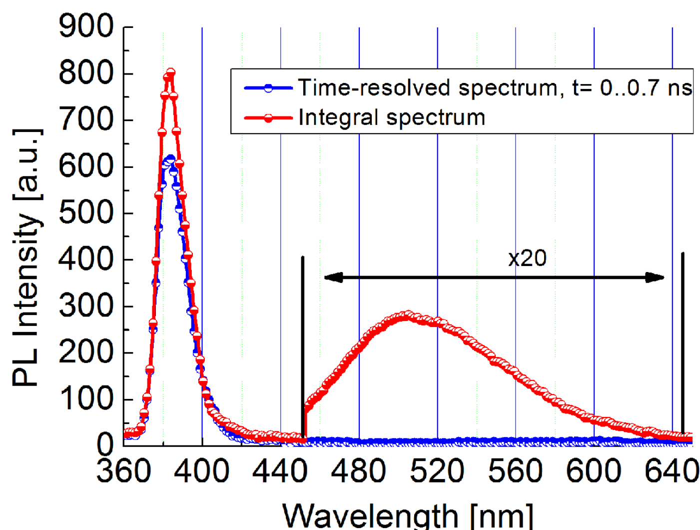

Figure 5.4 Time-resolved and integral spectra from the array of upright standing ZnO nanorods, of photoluminescence obtained at 300 K. The red curve shows the steady-state photoluminescence spectrum each point on the plot averages the photoluminescence signal measured over approximately 1 sec. The blue curve represents a time-resolved photoluminescence spectrum where each point was measured in the time slot from 0 to 0.7 ns from the moment of excitation.

be attributed to the emission of localized excitons. Therefore, the absorption of light with photon energies of 3.2 eV and higher may lead to the generation of excitons with possible subsequent dissociation into free charge carriers. The low temperature spectrum shows that the exciton peak has a maximum at 3.4 eV and a shift of $\sim$200 meV with respect to the one measured at RT. The broad band with the maximum at 504 nm is commonly attributed to the presence of oxygen vacancies. The crystalline quality can be estimated by a simple comparison of intensities of exciton peak and defect band. From the PL measurements we conclude that the generation of the electron-hole pairs at room temperature becomes possible with a photon energy greater than or equal to 3.2 eV under the formation of free excitons. We conclude also that a relatively large number of oxygen vacancies is present in the bulk.

The fast component - which has been recorded in a time window 0-0.1 ns after the excitation pulse onset - has a peak with the maximum at 382 nm. The integral spectrum reveals the broad band with the maximum at 504 nm which is usually attributed to the presence of defect states, caused in particular by the presence of oxygen vacancies. From the TR-PL measurements we can conclude that the sample has a relatively high optical quality.

5.4 Electrical characterization by means of C-AFM

To gain - in addition to morphology - information on electrical properties of individual NRs, it seems to be natural to apply C-AFM which is one of the most appropriate techniques for this purpose. However, the main problem of C-AFM measurements is the proper adjustment of the feedback loop parameters for the contact mode, which is a severe difficulty on rough surfaces. In the present section, a complementary study of the electrical transport in individual upright standing ZnO NRs utilizing C-AFM is described. This technique is promising for the characterization of as-grown nanostructures and provides the access to electrical properties on the nanometer scale. Applying C-AFM to study the electrical properties of the rods is an additional challenge, since the method operates in contact mode [29, 36]. In this technique, a conductive AFM probe is utilized as probing electrode and force sensor at the same time. The electrical contact area formed between the AFM probe and the sample depends on the mechanical properties of the tip's and sample's materials and the tip loading force [63]. Usually, the contact area is ranging from a few square nanometers up to some several hundreds of square nanometers, reaching in some cases μm^2 size. The size of the contact area determines to a high extent the electrical transport regime. The electrical transport via the tip-to-sample interface involves usually several mechanisms, like tunneling, field and thermal emissions [129]. This makes an analysis in the majority of cases difficult. Nevertheless, the dual functionality of the conductive probe enables one to influence the electrical transport regime by the application of proper tip loading forces thus favoring a certain mechanism of transport.

A poor electric contact stability and ill-defined tip conditions are usually the limiting factors in C-AFM applications. As a solution, a high tip loading force is applied in order to improve the contact stability. The formation and rupture of nanocontacts formed by the conductive AFM tip to ZnO NRs have been a subject of a recent study where it has been shown that a stable electrical contact may be formed with tip loading forces as low as $\sim$12 nN [105]. Measuring with forces above this value one can expect reproducible behavior of the two-dimensional (2D) current maps and Current-to-voltage curves (I-V). The I-V characterization of ZnO NRs using C-AFM reveals usually rectifying behavior which can be analyzed in terms of Schottky barrier formation between the C-AFM tip and the NR [105].

Here, we applied C-AFM to study electrical properties of as-grown ZnO NRs. C-AFM was used to record 2D current maps simultaneously with topography. These measurements have been complemented by local I-V characterization of the top and side planes of individual NRs as it is depicted in Fig. 5.10. The I-V curves were analyzed using the Shockley diode equation. The electrical and morphological data were correlated.

5.4.1 2D current maps

2D current maps: Acquisition conditions

The local electric properties of the NRs have been investigated using an MFP3D^{TM} AFM from Asylum Research equipped with the standard ORCA^{TM} module which allows to carry out C-AFM experiments and measure currents in the range from 1 pA to 20 nA. Further, a Nanoscope^{TM}IIIa AFM from Digital Instruments equipped with a home built C-AFM module was used, which allows to measure currents in the range from 50 fA to 200 pA [44]. The investigation of the electrical properties of ZnO NRs has been carried out solely in contact mode AFM under ambient conditions. It has been found that the stability of the feedback loop and imaging process in general are strongly dependent on the force constant of the cantilever and the scan rate. The best results for the topography in contact mode were obtained using PPP-EFM ($k = 0.5 - 9.5N/m$) conductive probes, where the feedback loop stability and the image quality are close to those obtained in intermittent contact mode AFM.

We also performed C-AFM measurements using DCP11 diamond coated conductive probes from NT-MDT^{TM}. Both the topography and current maps recorded with these probes exhibit less stability compared to those obtained using PPP-EFM probes, however, good stability could be achieved when carrying out measurements with deactivated slow scan axis. Since the roughness of the surface covered with ZnO NRs is very high, several requirements should be fulfilled to make the measurement possible. Relatively stable measurement conditions could be achieved on the NRs with an average diameter of ∼600 nm or larger and lengths up to 2.5-3 μm (measured by SEM). It has also been found that instabilities during C-AFM mapping may lead to a wear of the probe's conductive coating. Therefore, the scan velocity during C-AFM mapping was 0.5 μm/s or lower in order to achieve most stable conditions avoiding damages of the tip coating and to minimize the influence of parasitic capacitance effects at the tip-to-sample interface. The I-V characteristics were recorded between ±10 V applied to the sample at 0.1 Hz of voltage ramping rate and activated feedback loop. The 2D mapping in C-AFM as well as the tip positioning for I-V characterization have been performed with the scanner driven in a closed-loop mode. We did not observe any significant difference in the stability of the electrical contact for both types of probes at a loading force of ∼50 nN.

2D current maps: Si(111) substrate

During the course of the measurements in C-AFM mode, CDT-CONTR (Nanosensors^{TM}) silicon cantilevers with a boron doped diamond coating on the tip were used. The force constants k for such sensors were in the range from 0.02 to 0.77 N/m. The recording speed was reduced as much as possible to obtain better current images (0.18 to 0.6 μm/s), applied voltages were within the range -0.5 to -2 V. The loading force during the C-AFM characterization was of the order of 510 nN. The morphology of a single upright standing ZnO NR recorded in contact mode is presented in Fig. 5.5(a).

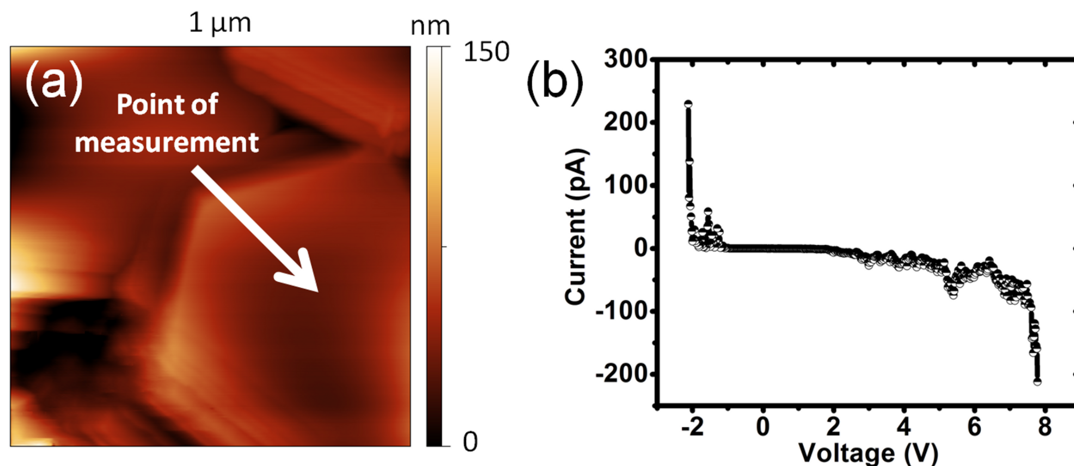

Figure 5.5 (a) Contact mode AFM image of ZnO NRs grown by thermal evaporation on Si(111). (b) The I-V characteristic recorded from the center of the NR marked in (a) with an arrow. (After [36]).

The relatively low quality of topography images in C-AFM mode results from a larger radius of the tips due to the conductive coating and from higher forces that have to be applied to the tip in comparison with intermittent contact mode AFM. In spite of this fact, the current images are in accordance with topography images for the TE- grown specimen. We have managed to obtain current maps on NRs with diameters as small as 300-500 nm, measuring as-grown samples without any additional treatment, like filling the NR array with a polymer matrix, etc. The topography image presented in Fig. 5.6(a) reveals clearly both the top and side facets of the NR. Interestingly there was always an increased current observed on the side planes of ZnO NRs. The current map has been recorded at -0.5 V which was a practical limit in the negative voltage region because of the large current bursts originating from the side plane of the NRs resulting in amplifier saturation.

For the conditions used here we did not notice any significant variation of the current originating from the top facets. It is worth mentioning that the topography and current map depicted in Fig. 5.6 are both recorded for the trace scan direction (left-to-right), the current spikes appear in this case preferentially on the left side of the NRs. The current varied in the range from 0 to 200 pA (which is the amplifier limit). A comparison of the topography and current profiles (Fig. 5.6(c)) reveals that the maximum current bursts appear simultaneously with the moments of rapid height increase. According to [16, 130] a possible explanation for this observation is possible piezoelectric charge carrier generation in the ZnO NR due to bending of the NR. However, the observation of this phenomenon by C-AFM technique is currently under strong discussion [17, 131].

Here, the observation of currents on the edges of ZnO NRs may not be solely related to the piezoelectric response. In order to address this problem we performed C-AFM experiments on a ZnO NR containing step-like structures which are presented in Sec. 5.4.2. As mentioned

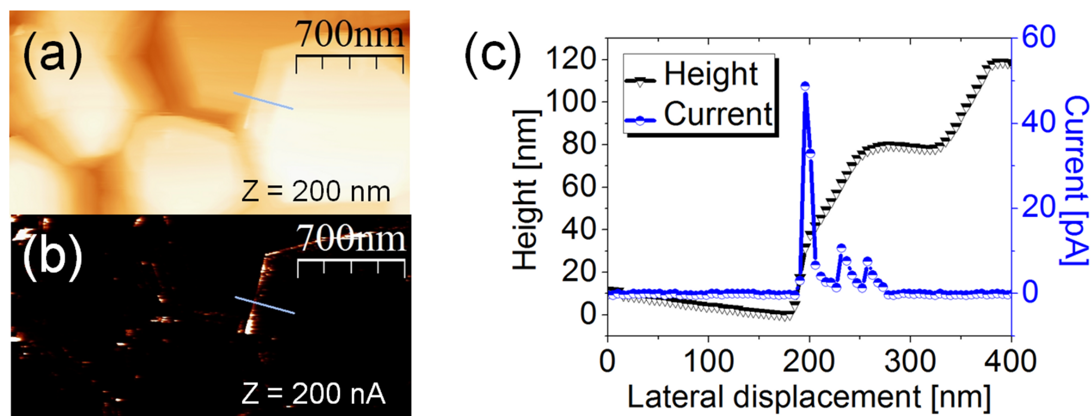

Figure 5.6 2.5 μm$\times$1.25 μm C-AFM images of ZnO nanorods grown by TE on Si: (a) topography, (b) current map at -0.5 V, (c) topography and current cross-sections taken across the edge of the NR as marked in (a) and (b).

above, the C-AFM measurements have been performed at low tip-to-surface forces. Though, the tip loading force of 5-10 nN should guarantee a mechanically and electrically stable contact, according to Ref. [105], this is the region where the abruption-formation of Schottky nano-contacts to ZnO takes place which can potentially cause instabilities. As it will be shown in the following, the current bursts appear even at higher tip loading force, where the electrical contact should be stable according to Ref. [105]. Additionally, an investigation of the electrical transport through Schottky nano-diodes indicates that the barrier is lowered significantly if the contact size is smaller than the characteristic length in the material [132]. The current bursts might also be caused by feedback instabilities which led to a decrease of the contact area resulting in a lowering of the barrier height.

For the HT-grown specimen, however, there are still difficulties with C-AFM measurements due to the small diameter of the rods.

In addition to two-dimensional C-AFM images at fixed voltages, also I-V curves can be recorded from a single ZnO NR. The I-V characteristic recorded from the center of a ZnO NR on a Si(111) substrate is presented in Fig. 5.5(b). The observed I-V characteristics are similar to that of a p-n diode. More details on local I-V characterization are presented in Sec. 5.4.3.

2D current maps: FTO substrate

The results of the C-AFM measurements are presented in Fig. 5.7. Topography images are given in 2D (a) and 3D (b) presentation, respectively, in order to provide a better insight into the structural peculiarities of the investigated system. The current maps were recorded in forward (from left to right, (a)) and backward (from right to left, (b)) scan directions at a sample bias of +0.1 V. The small value of the applied bias is conditioned by the fact that ZnO NRs exhibit a high conductivity, most likely due to their high surface conductivity [133].

It is seen that the current maps recorded in forward and backward scan direction differ from each other. The current map in the forward direction exhibits more localized and intense current bursts, whereas in the opposite scan the bursts are distributed more homogeneously and have a lower magnitude. The difference is artificial and results most likely from the non-symmetrical tip geometry with respect to the sample. The appearance of the current bursts, however, is an interesting phenomenon. The current map recored in the forward

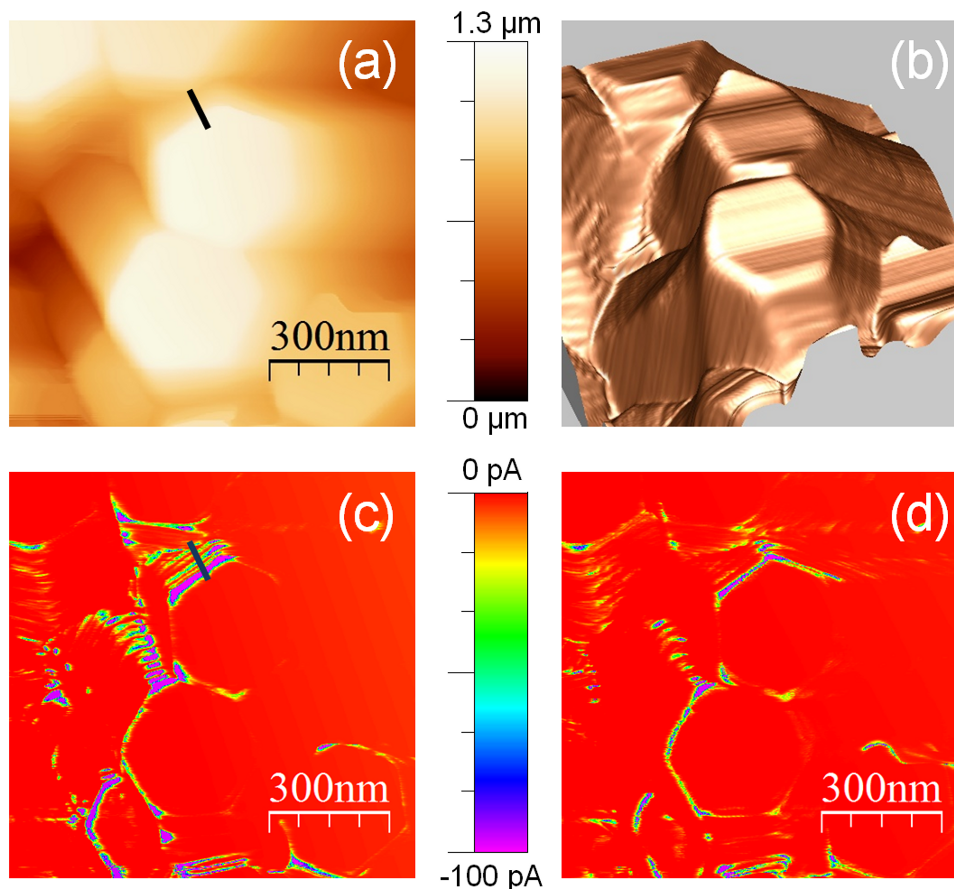

Figure 5.7 C-AFM images of ZnO NRs grown on FTO. 2D (a) and 3D (b) topography images of ZnO NRs reveal the presence of step bunch-like structures at the side plane instead of a singular facet. The current maps recorded at +0.1 V of sample bias in forward (c) and backward (d) directions demonstrate the presence of current spikes which appear seemingly at the edges within the side plane.

scan direction has been post-processed, and the line profiles taken from the post-processed image are subject of further analysis. The first derivative of the current map is shown in Fig. 5.8. This representation helps to locate the current extrema and has been applied in order to perform a simple analysis of the current behavior at the step edges of the side plane of the ZnO NR. The 2D current map derivative presented in Fig. 5.8 reveals a number of

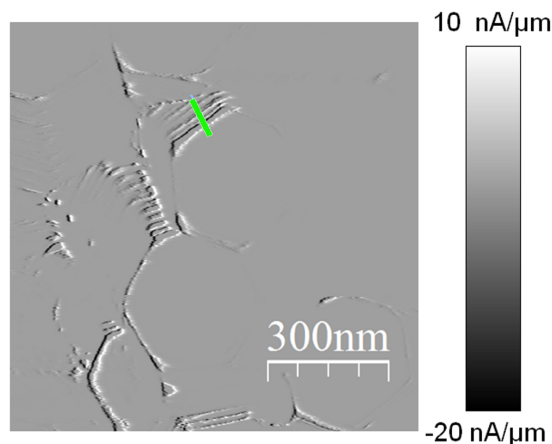

Figure 5.8 First derivative of the forward current map presented in Fig. 5.7(c).

clear bursts originating from the step-like side planes of the ZnO NRs. The points where the current derivative reaches its extrema correspond to the situations when the current changes its behavior from rise to decay or vice versa. The points where the current derivative is equal to zero correspond to either current minimum or maximum.

5.4.2 Current line profiles

A comparison of the profiles taken from the current (Fig. 5.7(c)) and current derivative (Fig. 5.8) maps with the corresponding topography profile taken from the Fig. 5.7(a), is presented in Fig. 5.9. It provides a clear view into the behavior of the current at the step-like side plane for one of the ZnO NRs. The scan direction is denoted by the arrow in Fig. 5.9. The correlation between zero points on the current derivative profile and corresponding points on the topography is depicted by dashed lines. This kind of behavior is valid for the other NRs inspected, i.e. a general trend is that the current reaches its maximum at the points with a large height gradient, whereas the current minima can be associated with a smaller height gradient.

5.4.3 Local I-V characterization

The I-V characterization on individual upright standing ZnO NRs has been the subject of our study in order to determine their carrier transport properties. The force applied to the tip was varied from values typical for two-dimensional C-AFM measurements to twice this value. It has been found that for PtIr coated probes, the I-V characteristics are non-reproducible when measuring with tip loading forces of ~50 nN or larger. Therefore, the I-V characterization of the ZnO NRs has been performed entirely using diamond coated conductive probes (DCP11 from NT-MDT^{TM}). The low-speed scan direction was turned off at the moment when the NR's position and geometry were defined.

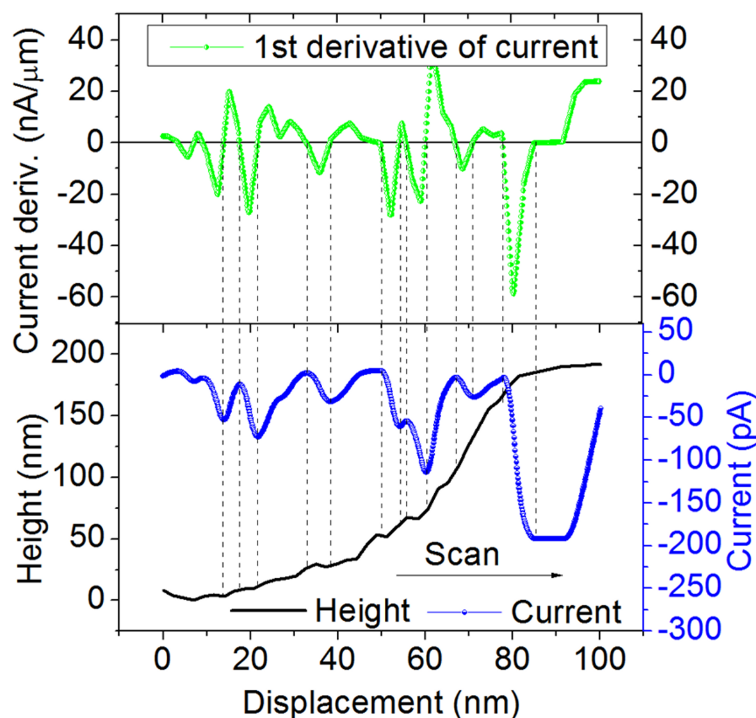

Figure 5.9 Correlation between the topography, current, and current derivative profiles taken from the locations marked by correspondently colored lines in Fig. 5.7(a), (c) and Fig. 5.8.

HT-grown ZnO NRs

The small diameter and high aspect ratio of the HT grown samples hamper 2D measurements in contact mode. Though, the characterization of their electrical properties can be done via I-V curve measurements as presented in Fig. 5.11(a). Since the morphology of the HT grown NRs is not achievable via the measurements in contact mode, the positioning of the conductive probe should be done in tapping mode. In order to obtain I-V characteristics, the system is switched to contact mode after probe positioning in tapping mode. Small lateral displacements (up to 20-30 nm) are unavoidable. Therefore, the I-V characterization of HT grown samples presented in Fig. 5.11(a) has been performed in "hit-or-miss" fashion and ohmic curves which occurred due to the contact with the FTO substrate were removed from the plot. The rest of the I-V curves demonstrated rectifying behavior, with little distortion, perhaps due to additional field emission during the experiment. The characteristic feature of the I-V curves is the presence of a jump at around +1.8 V sample bias (reverse direction) which happens probably due to contact instabilities.

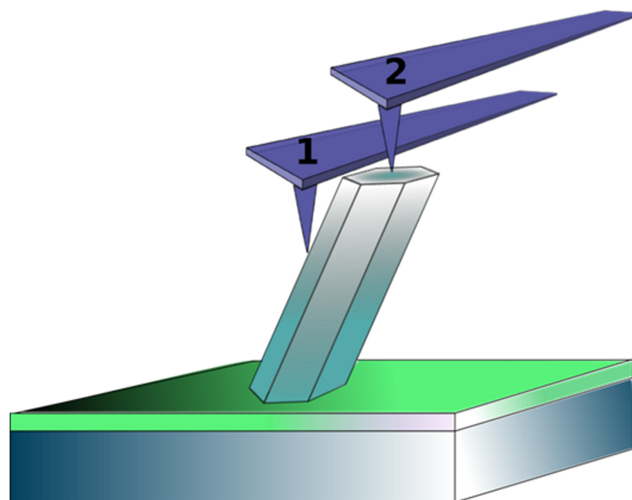

Figure 5.10 Scheme of the experiment for the case of a TE grown sample.

TE-grown ZnO NRs

The I-V characteristics presented in Fig. 5.11(b) have been recorded at the top and side

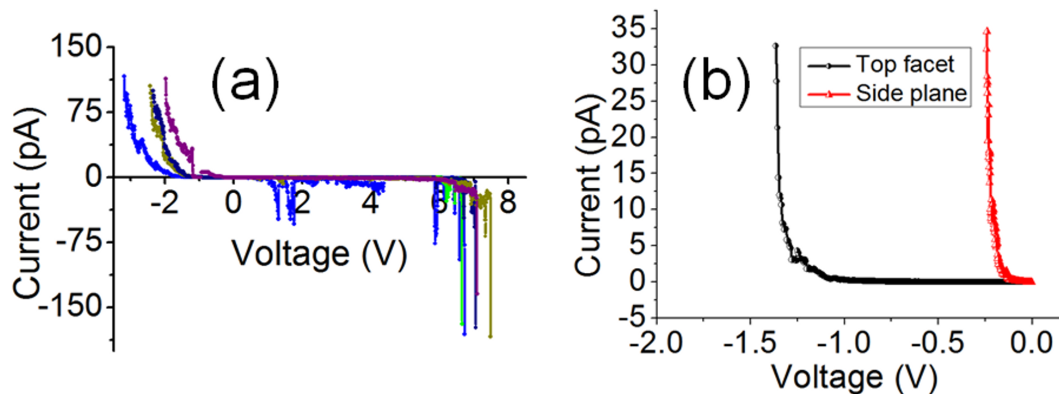

Figure 5.11 (a) I-V curves recorded from HT grown NR on FTO, (b) Forward I-V characteristics recorded from the top facet (circles, black) and side plane (triangles, red) of a tilted TE grown ZnO NR. The characteristics revealing a significant difference between turn-on voltages.

planes (as it is depicted in Fig. 5.10) of the ZnO NRs with a tip loading force of about 50 nN. Such a loading force is at least twice as large as the one needed to obtain a stable Schottky contact between the PtIr coated tip and ZnO NR [105]. The characteristics reveal that the side plane has a much smaller turn-on voltage which can not be simply explained via the difference in electrical contact area (see Sec. 5.4.4). In fact the effective electrical contact area has been estimated as 10 nm^2 by a method described by Sarid [63], and the current

densities J used for the presentation in Fig. 5.12 were calculated with this value. The reverse diode current (not shown) demonstrated in some cases rather significant deviation from zero level at a sample bias higher than +5.5 V. We also examined the same structure with diamond coated conductive probes (the data are not presented), and found the same type of electrical behavior, however the electrical contact stability was lower at comparable tip loading forces. Nevertheless, the I-V curves in both cases are asymmetrical, demonstrating rectifying behavior and linearize when presented in an (lnJ) $vs.$ V plot (Fig. 5.12).

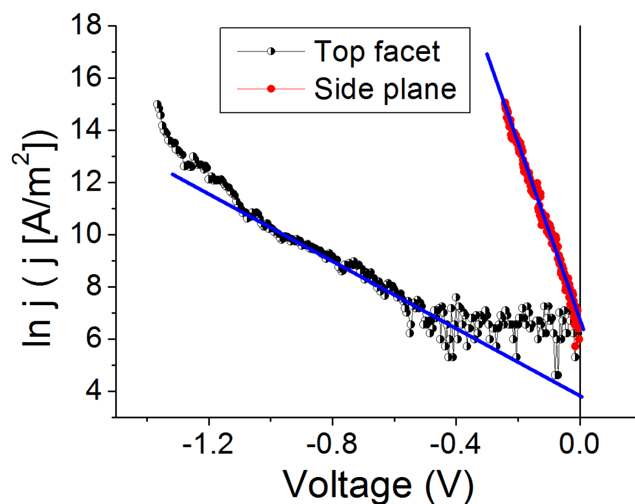

Figure 5.12 Forward I-V characteristics recorded from the top facet (half-filled circles, black) and side plane (filled circles, red) of a tilted TE grown ZnO NR linearized in logarithmic scale. The fits (blue lines) were used to determine the Schottky barrier heights and ideality factors.

5.4.4 Analysis of the dark conductivity

As mentioned above, C-AFM measurements rely on the fulfillment of several requirements, such as proper tip loading force, scanning rate, applied bias, etc. The 2D current maps measured in contact mode C-AFM revealed a number of current bursts originating from the side planes of the ZnO NRs. The appearance of the current bursts is an interesting phenomenon indeed which will be discussed in the following. We believe that the difference between backward and forward scan directions of 2D current maps is originating from the non-symmetric tip-to-sample geometry. The current maps in forward and backward directions are recorded with two essentially different electrical contacts (back and front sides of the tip), thus showing some discrepancy. Several possible mechanisms can be responsible for the appearance of the current bursts. The current bursts appear already at very low sample bias, indicating high conductivity of ZnO NRs and low barrier height between the PtIr coated tip and the

ZnO NRs. ZnO is a wide band gap semiconductor (3.37 eV) [134] and the intrinsic bulk conductivity is very low even if one takes into account that ZnO exhibits n-type conductivity in absence of intentional doping. Studies of the surface conductivity [135–138] reveal that the presence of various adsorbates on the ZnO surface may enhance the conductivity by some orders of magnitude. Also, ZnO exhibits persistent photoconductivity, and its conductive state may persist for very long time like hours or even days [139, 140]. Therefore, the pre-exposure to ambient light could also lead to enhanced conductivity.

The analysis of the current derivative profile presented in Fig. 5.9 reveals that the current bursts appear at the points with a large gradient of height. On the first glance, this may serve as an indication for instabilities in the feedback loop of the AFM which cause a rapid increase in the loading force with the consequent decrease of the contact resistance. At the same time, the appearance of the current bursts at the side planes of the NRs may be associated with a larger contact area of the tip-to-sample contact. However, one has to admit that the dependence of the current on the contact area is linear and does not explain the essentially different behavior of the I-V characteristics recorded from the top and side planes (Fig. 5.11(b)) of the NRs. We also performed analysis of the I-V characteristics (Fig. 5.12) in terms of Schottky barrier formation between the tip and the ZnO NR. The values of the Schottky barrier heights have been determined using the diode equation [54]:

$$J = J_0(\exp(-qV_{bias}/\eta k_B T) - 1) \tag{5.1}$$

where q and k_B are the electron charge and Boltzmann constant respectively, V_{bias} is the sample bias, T is the temperature, η is the ideality factor, and J_0 is the saturation current density. The I-V characteristics measured from the top and side planes have been linearized in $ln(J)$ vs. V coordinates. The intersection with the y-axis gives the value for the saturation current density which is defined as:

$$J_0 = A^{**}T^2 \exp(-q\Phi_{SB}/k_B T) \tag{5.2}$$

where $A^{**} = 72\ Am^{-2}$ is the Richardson constant for ZnO and Φ_{SB} is the Schottky barrier height. The saturation current densities determined from the intersection with the y-axis (Fig. 5.12) equaled to 83.2±0.1 $\text{A}\cdot\text{m}^{-2}$ and 1077±0.1 $\text{A}\cdot\text{m}^{-2}$ for the top and side planes, respectively. The data have been averaged over 10 measurements. The corresponding Schottky barrier heights have been estimated as ∼0.54 eV and ∼0.48 eV for the top and side planes, respectively. The ideality factors have been determined from the slope of the $ln(J)$ vs. V curves as:

$$\eta \equiv \left(\frac{q}{k_B T}\right)\left(\frac{\partial V}{\partial(lnJ)}\right) \tag{5.3}$$

The ideality factor equaled to ∼6.7 for the top and ∼1.2 for the side plane, respectively. We believe that it is worthwhile to collate the ideality factors measured at different voltages for this case, even though they should not be directly compared. Since the ideality factor of the Schottky contact formed between the side plane of the ZnO NR and conductive PtIr probe is close to unity, thermionic emission can be considered as the main mechanism of

transport. The electrical transport is driven by the drift of charge carriers due to the electric field applied, rather than due to the non-thermal generation-recombination processes which can take place at the tip-to-sample interface or in the depletion region. For the contact between the top plane and the probe, the deviation of the ideality factor from unity could be caused by several reasons. A high rate of non-equilibrium generation-recombination processes is considered commonly as a main mechanism causing deviation of the ideality factor from unity. Other important influences are the shunt, series resistances, image-force lowering effects and tunneling. The analysis of 2D current maps and I-V characteristics recorded with different types of conductive probes (using the same tip loading force) reveal a difference in the magnitudes of the current recorded. Comparison of the current maps recorded with PtIr (PPP-EFM from Nanosensors^{TM}) and conductive diamond coated probes (DCP11 and NT-MDT^{TM}) reveals that the utilization of the latter leads usually to smaller current magnitudes. This is most likely due to the increased barrier height between the tip and ZnO NRs. The second important parameter defining the magnitude of the current flowing via the tip-to-sample interface is the contact resistance which can be regulated to some extent by the force applied to the tip.

5.4.5 Remarks on the local electrical characterization of ZnO NRs by C-AFM

Here, we investigated the electrical properties of as-grown upright standing ZnO NRs by means of C-AFM. The 2D current maps have been recorded solely in contact mode using PtIr coated probes. The current maps revealed current bursts at the side planes of the NRs and a discrepancy between the scans recorded in backward and forward directions. We believe that the discrepancy originates from the asymmetrical tip geometry, whereas the observed current bursts are due to the difference in the electrical properties between the side and top planes of the ZnO NRs. However, we can not rule out completely that they appear as a result of instabilities in the feedback loop [17]. In order to gain more clarity about the correlation between the structural peculiarities and electrical properties, we performed preliminary C-AFM experiments on lying ZnO NRs which are presented in Fig. 5.13. For this experiment, the ZnO NRs prepared by the method described above were mechanically removed from the substrate, dispersed by an organic solvent on an insulating substrate and contacted with tungsten by the help of Focused Ion Beam (FIB). With C-AFM measurements we faced so far problems resulting from contamination of the NRs with residuals of the organic solvent used. However, we expect that experiments performed in this configuration will help to rule out the possible artifacts mentioned above.

For I-V characterization of upright standing NRs we used diamond coated, conductive probes. These measurements reveal Schottky barrier heights equal to ~ 0.54 eV and ~ 0.48 eV for the top and side planes, respectively. Thus, the lower Schottky barrier height for the contact to the side plane of the ZnO NR also contributes to higher currents. Therefore, this difference of the Schottky barrier heights for the side and top planes of the ZnO

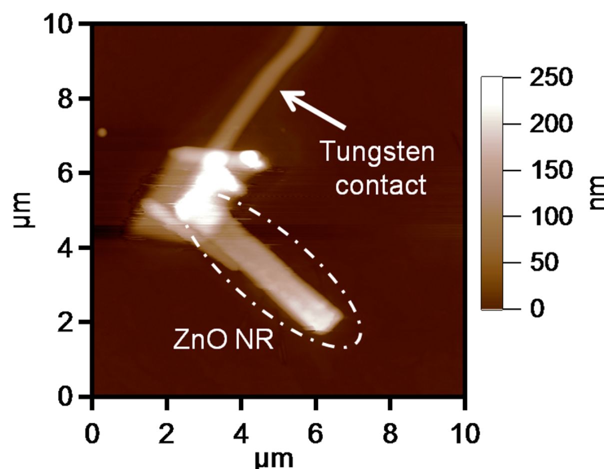

Figure 5.13 Topography of a ZnO NR lying on an insulating substrate (native oxide covered silicon wafer) and contacted with tungsten by FIB. This setup is planned to use for C-AFM inspection of the NR side facets.

NRs should be taken into account when analyzing the appearance of the 2D current bursts. The other influences like parasitic capacitance effects, leakage currents, etc., can not be completely excluded from the consideration.

5.5 Electrical characterization by means of PC-AFM

It is commonly believed that exposure of ZnO surfaces to light irradiation induces photodesorption of oxygen molecules [141] from the surface which leads in turn to a rise of conductivity. Therefore, the photoresponse in ZnO is very often considered as an exclusively surface induced process whereas the role of the bulk properties is negligible. However, it has been shown recently that the phenomenon of persistent photoconductivity in ZnO can also be attributed to the presence of oxygen vacancies in the bulk [142]. Thus, more precise confirmation of the origin of this phenomena is required and the characterization of single, separated as-grown ZnO NRs is of big importance.

Here, we employ the PC-AFM (described in Sec. 2.3) technique to study the electrical transport in individual upright standing ZnO NRs grown by thermal evaporation under illumination. The results together with the results obtained by means of time-resolved PL suggest that the photoresponse in ZnO NRs originates preferentially from the photoexcitation of charge carriers from Defect Localized States (DLS). The experimental findings stay in a good agreement with previous theoretical predictions based on density functional theory calculation [143] and will be discussed on the basis of the presence of oxygen vacancies.

The local photoelectric properties of the NRs have been investigated using an MFP3D^{TM}

AFM from Asylum Research equipped with the standard ORCA™ module which allows to carry out C-AFM experiments and measure currents in the range from 1 pA to 20 nA. We also used an external amplifier (Model 1211 from DL Instruments) described in Sec. 2.3 in order to extend the range of measured currents.

5.5.1 I-V characterization under illumination

The influence of illumination on the current-to-voltage characteristics of a single upright standing ZnO NR is shown in Fig. 5.14. The current-to-voltage characteristics were recorded from the sample surface which was under illumination directly from the optical fiber placed under an angle of ∼15° - 20° towards the surface. For this measurements we used standard ORCA C-AFM holder and conductive diamond coated DCP11™ probes from NT-MDT with a force constant of ∼5.5 N/m. The tip height for probes of this type is about 15-20 μm which implies a restriction on the angle of illumination to the aforementioned ∼15° - 20° with respect to the sample surface due to shadowing. The illumination at large angle of incidence causes also an increase in the reflection from the surface, therefore the photoresponse is significantly suppressed in this configuration of illumination.

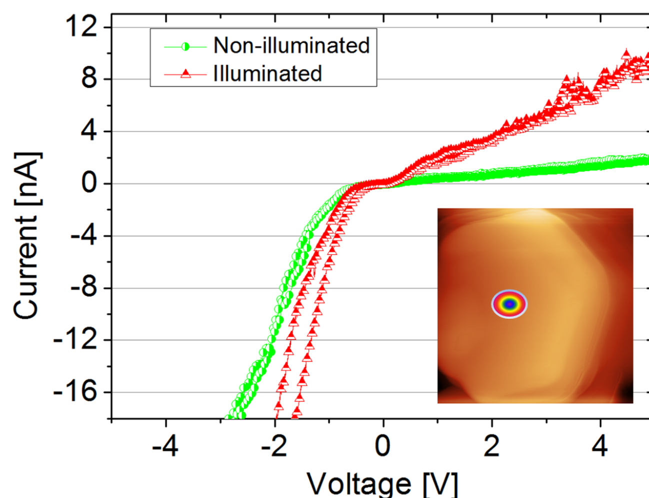

Figure 5.14 Current-to-voltage characteristics of dark (green curve, circles) and illuminated state (red curve, triangles) recorded from a single upright standing ZnO nanorod. The illuminated characteristic was recorded using a Xe 150W lamp (white light) as light source.

The dark and illuminated $I-V$ characteristics were both recorded with 30 s delay between the measurements, the voltage was ramped back and forth with a rate of 20 V/A. Both, illuminated and dark characteristics demonstrate rectifying behavior with rather significant deviation of the reverse current from zero level. Moreover, the reverse current in both cases demonstrates a linear dependence on the applied voltage which may be due to the

photoexcitation of charge carriers from the valence band to defect Perturbed Host State (PHS) (depicted as transition (3) in Fig. 5.18). The $I-V$ characteristics recorded from ZnO NRs under illumination are degenerated which indicates the increase of the charge carrier concentration.

5.5.2 Transient photocurrent

The investigation of transient photocurrent behavior in ZnO NRs has been carried out in contact mode AFM, the tip location was done in intermittent contact mode. After the ZnO NR had been located, the system was switched to contact mode. The loading force during the transient PC-AFM characterization was of the order of 2030 nN. For these experiments we used ATEC-CONTPt probe with the force constant $k = 0.02 - 0.75N/m$.

To find the optimal probe location and to avoid possible probe damage we performed imaging of the sample surface with the slow scan axis of the AFM switched off. After stable conditions were achieved, the conductive ATEC-CONTPt probe was located on the top facet of one of the upright standing NRs and the sample bias was applied. The photocurrent has been recorded over a long period of time ($\sim$ 3 hours) at a sample bias of $U_{smp} = -10\ V$. In order to determine the rise and decay time constants we applied several cycles of illumination using white light (full spectrum) of the Xe lamp at 150 W. The transient photocurrent curve recorded during the first cycle of the illumination is shown in Fig. 5.15. The bias was applied

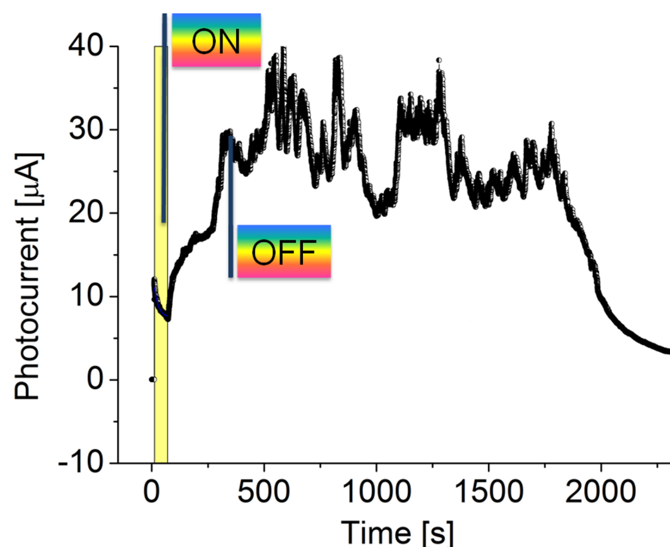

Figure 5.15 Photocurrent rise and relaxation during the first cycle of the experiment. The bias of -10 V was applied at 0 s, the yellow bar (shadowed rectangular area) indicates the initial dark current decay. After sample was illuminated it is clearly visible that photoconductivity persists for about 1835 s and then decays exponentially.

at time 0 which caused a current jump from 0 to 12 μA. This increase is followed by a slow decay which is well approximated by the exponent:

$$I = I_0 + C_1 e^{-(t-t_0)/\tau} \tag{5.4}$$

where t is time and τ is the decay time constant. As the result of fitting, the initial decay of the dark current after the application of sample bias was determined to be ∼18 s. The illumination of the sample surface for the first cycle was started at $t = 75$ s and stopped at $t = 300$ s when the current was saturated. After the illumination was switched on, the photocurrent raised in several steps. Each step of this raise can be well approximated by the so called logistic equation:

$$I = I_0 + \frac{K_1 - I_0}{1 + (t/t_0)^p} \tag{5.5}$$

where p is a number which can take various real values, increasing with $p = 1.5$ for the first step. Surprisingly, the photocurrent persisted at about the level of saturation (or even higher) from $t = 500$ s to $t = 1835$ s exhibiting instabilities in the form of pronounced current spikes which appeared randomly. At $t = 1835$ s the current abruptly started to decrease following the trend which can be well fitted by Eq. 5.4.

Further cycles (including the first cycle) of the sample illumination and corresponding transient photocurrent behavior are shown in Fig. 5.16. During all cycles - excluding the

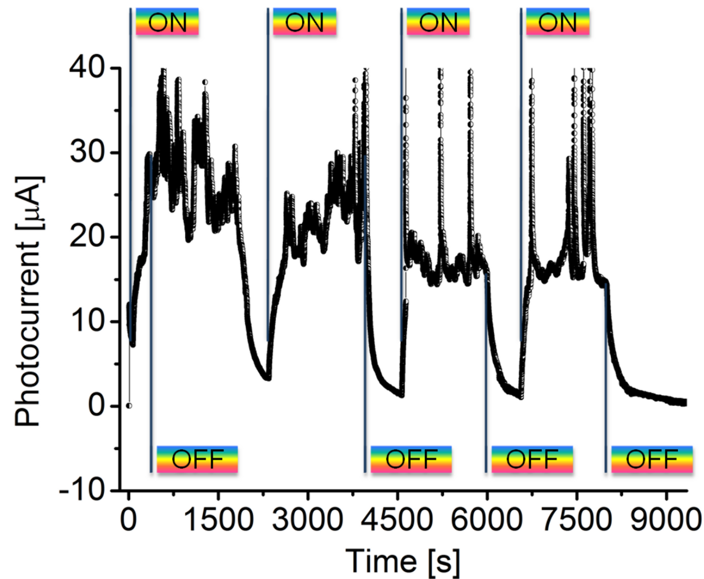

Figure 5.16 The plot demonstrates the course of the experiment over several cycles of the illumination. The sample bias is -10 V, the source of illumination is a 150 W Xe lamp (white light source).

first one - the photocurrent raised, reached the saturation level and stayed there until the

illumination was switched off. Interestingly, the saturation level is decreasing in time. When fitted by Eq. 5.4 it gives the decay time constant of $\tau \simeq 1400$ s.

The transient photocurrent experiments taken from a single separated NR provide information about the characteristic rise and decay time of the photoresponse. An interesting peculiarity of the transient photocurrent measured at different ZnO NRs is that the current initially stays at the saturation level during the first cycle of the illumination even when illumination is switched off and than rapidly decays. In principle, this behavior can be caused by several mechanisms, like water dissociation and desorption, recharging of defects, etc. We believe that this phenomenon should be considered as a current induced electrochemical process. Apparently, the first cycle of illumination of the NR causes a rise of the photocurrent initiating some electrochemical processes which endure until material for the electrochemical reaction is available.

Unfortunately, we were not able to detect the fast component of the photocurrent since it has a much lower magnitude compared to the slow component and further investigations using lock-in technique are needed.

5.5.3 Photocurrent spectroscopy

In order to gain insight into the electronic structure of single upright standing ZnO NRs, we measured the spectral characteristics of the photocurrent by means of PC-AFM. The measurements were performed in contact mode using ATEC-CONTPt probes applying a tip loading force of ∼30 nN. The result of these measurements is presented in Fig. 5.17. It

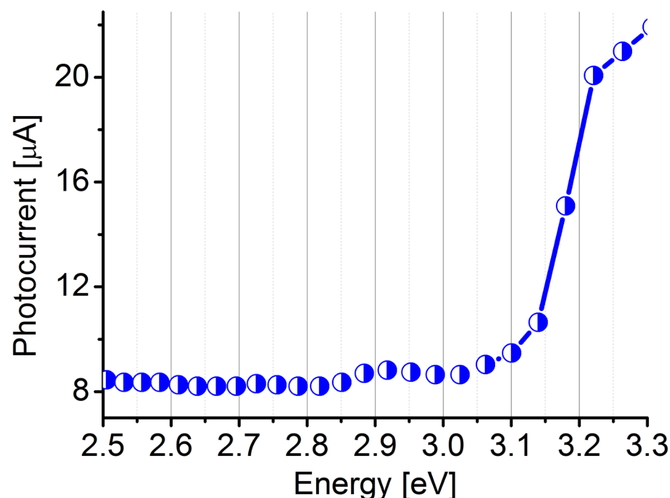

Figure 5.17 The photoconductivity spectral response from a single upright standing ZnO NR recorded using a 150 W Xe lamp connected to the monochromator. The sample bias was -10 V. The spectrum was recorded starting from the lower energies withstanding the interval of ∼30 sec between the points.

has been found that the sample is already sensitive to illumination with a wavelength below 400 nm, i.e. with a photon energy of 3.1 eV which is smaller than the band gap of ZnO (3.37 eV). The photocurrent spectra were measured starting from longer wavelengths with the time delay varying in the range from 30 s to 2 min between acquisition of two neighboring data points. This time delay was sufficient to account for the time needed for photocurrent saturation. Each data point in the photocurrent spectra represents the average value for 100 points measured at 1 kHz of acquisition rate.

Recently, a theoretical explanation of the persistent photoconductivity in ZnO has been provided on the basis of predictions made by density functional theory calculations [143]. The model involves a two-step process where an oxygen vacancy V_O changes its state from non-conductive (α - configuration, V_O^0) to conductive (β - configuration, $V_O^{2+} + 2e^-$) with the subsequent appearance of a PHS below the conduction band minimum under illumination. The corresponding energy-level diagram is presented in Fig. 5.18. The electrons from the

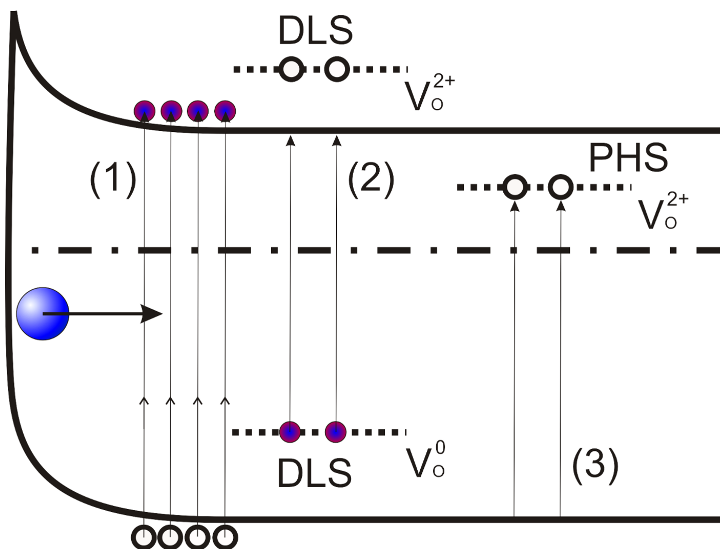

Figure 5.18 Schematic energy-level diagram of ZnO taking into account the existence of theoretically predicted [143] $\alpha-$ and $\beta-$ type states of oxygen vacancies. The processes of electron-hole pair generation, charge carrier photo-excitation from DLS and to PHS states of oxygen vacancy are marked as (1), (2), and (3), respectively.

energy level which corresponds to the α - configuration are photoexcited to the conduction band contributing to the photocurrent. The existence of the PHS state implies also a trapping of the mobile charge carriers in this state. The transition back to the non-conductive state requires a simultaneous thermal activation of the electrons from the PHS state to the conduction band and capturing them back on the defect. The presence of the PHS state makes a transition from the valence band to the PHS state possible, which leads to the formation of holes and therefore to an increase in p-type conductivity under illumination.

Basically, this assumption fits very well to our experimental observations.

The photocurrent spectrum presented in Fig. 5.17 reveals that the sample becomes photosensitive at ~400 nm (3.1 eV). To estimate a band gap energy which could be directly compared with the values derived from the PL experiments, we normalized the data presented in Fig. 5.17 taking into account the emission spectrum of our light source (i.e., we switched in the presentation to the characteristic of quantum efficiency of light conversion). Then, the data were plotted in coordinates $(I_{PN}\hbar\omega)$ *vs.* $\hbar\omega$ where the I_{PN} is the normalized photocurrent. The result of the linearization is presented in Fig. 5.19. We used an extrapo-

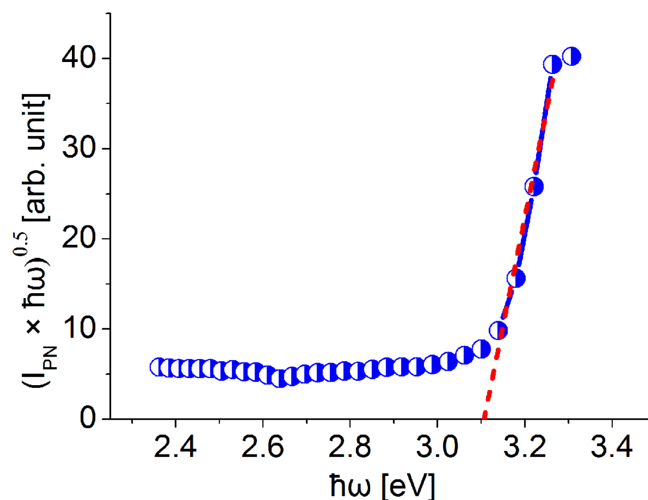

Figure 5.19 The quantum efficiency of light conversion linearized in coordinates $(I_{PN}\hbar\omega)$ *vs.* $\hbar\omega$. The extrapolation until $I_{PN}\hbar\omega = 0$ provides the energy corresponding to the transition involved in the photocarrier generation process.

lation of the linear region to obtain the energy of the transition involved in the photocarrier generation process. The obtained value $E_{min} \cong 3.1\ eV$ is the minimal photon energy sufficient for the photoexcitation of mobile charge carriers. This value turned out to be ~100 meV lower than the band gap energy determined from the PL experiments. Therefore, we can conclude that photocurrent in this region can not be simply explained via band-to-band transition with subsequent electron-hole pair generation and oxygen desorption. We believe that the phenomenon of the persistent conductivity is attributed to the presence of defect states at energies 100 meV higher than the valence band maximum. On the other hand, the transformation of defects from α to β configuration stays in a good agreement with the experimentally observed increase in the p-type conductivity. The increase in conductivity at positive voltages during the $I - V$ characterization under illumination can be explained on the basis of this model as well.

It is important to note that in contrast to the explanation given above, the standard model [141] involves the processes of oxygen molecule photodesorption to explain photoresponse in ZnO. Adsorption of oxygen on the ZnO surface causes the capture of electrons leading to the

formation of a negatively charged layer and a depletion region near the surface. The presence of adsorbed oxygen introduces a trap surface state within the band gap. The probability P_s of population for this level is given by [144]:

$$P_s = \frac{n_s(T)}{n_b(T)} = \exp\left(\frac{-qV_b}{k_B T}\right) \tag{5.6}$$

where qV_b is the band bending caused by the adsorbed oxygen, n_s and n_b are the concentrations of the charge carriers near the surface and in the bulk, respectively. The probability drops with an increasing amount of oxygen adsorbed at the surface. As a result, the process of electron transport from the bulk to the surface is also getting slower. The level of saturation is achieved when the energy of the trap state reaches the Fermi level due to the bend bending. This model based on photodesorption explains the changes in conductivity very well, however, it is inconsistent with our data obtained by photocurrent spectroscopy which reveal the photoresponse caused by photons with energies lower than the band gap.

It is generally assumed that when the surface is exposed to light with a photon energy higher than the band gap in ZnO, electron-hole pairs are created [141]. Then, the holes move toward the surface in the electric field of the surface depletion region and recombine with the electrons there $[h^+ + O_2^- \rightarrow O_2(g)]$. As a result we have an excess of electrons which were generated during the light absorption and which contribute to the photocurrent when the sample is biased. The aforementioned model implies that the photoconductivity in ZnO is limited to the fundamental absorption range (i.e with the photon energies higher than the band gap). This model would be inappropriate if the photoresponse is observed in the range of energies lower than the band gap. If the energy of the incident photon is lower than the band gap, the conductivity could increase only at the expense of the photoexcitation of electrons from defect levels. This process excludes generation of free holes and photodesorption due to the recombination of free holes with trapped electrons on the oxygen molecules (standard model to explain photoresponse in ZnO [141]).

Chapter 6

Results IV: Application of C-AFM to the electrical characterization of high-temperature superconductors

The present chapter is based on the results published in Ref. [6, 7] from the publications list.

Superconducting devices may provide many advantages for future electronic circuits. However, the majority of nowadays available materials operate at very low temperatures and demand cooling, which makes them cost inefficient and limits their use. The cuprate High-Temperature Superconductors (HTSC) with their higher critical temperatures offer practically achievable cooling requirements. The technological implementation, however, is limited due to the problems with reliable patterning of this material at the nanometer scale. Most of the currently used patterning methods are based on the removal of material, affecting the mechanical stability of the remaining HTSC structures [145]. Nano-patterning of films requires advanced technology such as focused ion-beam lithography [146].

Here, we characterized the electrical properties of patterned high-T_c superconducting $YBa_2Cu_3O_7$ (YBCO) thin films by C-AFM. The YBCO films were modified and patterned by Masked Ion-Beam Structuring (MIBS) with He^+ ions of 75 keV energy. The C-AFM has been employed to examine the influence of He^+ irradiation on the surface conductivity of the YBCO thin films.

6.1 Sample preparation

Epitaxial YBCO thin film were grown on MgO(001) single crystal substrates by pulsed-laser deposition. The substrate surface area was 25 mm^2, the substrate thickness was 1 mm. The thickness of the as-grown YBCO layer was 230 nm for 6000 pulses of a KrF UV excimer laser at a laser fluence of 3.2 J/cm^2. Surface planarization of the as-prepared YBCO thin film was achieved by a three-step process consisting of chemo-mechanical polishing, plasma etching,

and thermal annealing. The film was polished by a paste containing diamond particles of 100 nm diameter (Kemet company), ethanol and developer (Shipley MF-319). After cleaning of the polished film in an acetone ultrasonic bath, the residues of diamond paste were etched away in a glow discharge at 0.04 mbar of argon background. After plasma etching, the films were annealed in oxygen (T = 750 °C, P = 800 mbar) to compensate for oxygen depletion and to annihilate surface defects introduced by polishing and glow discharge cleaning.

For sub-micron patterning of planarized YBCO films, a commercial Si stencil mask 2 μm thick was used. The stencil mask had various apertures ranging from 1.5 μm to 125 nm in size. The narrowest Si lamella separating adjacent mask openings had a width of approx. 70 nm (as determined by SEM).

For MIBS on small sample area ($\sim$1 mm^2), a Van de Graaff accelerator (AN700 system) was used. Here, the He^+ ion beam current was $I = 1\pm0.1$ nA, the spot area at the sample position $A_{spot} = 1.33$ mm^2, and the beam current density $J_B = I/A_{spot} = 75$ nA/cm^2. The irradiation dose applied to all samples was 3.0×10^{15} ions/cm^2 corresponding to an exposure time of 106 min. The divergence of the ion beam was $\leq$1 mrad and the angle of incidence was 0° with respect to the surface normal. Film samples were irradiated at T = 300 K and at a background pressure of 10^{-7} mbar.

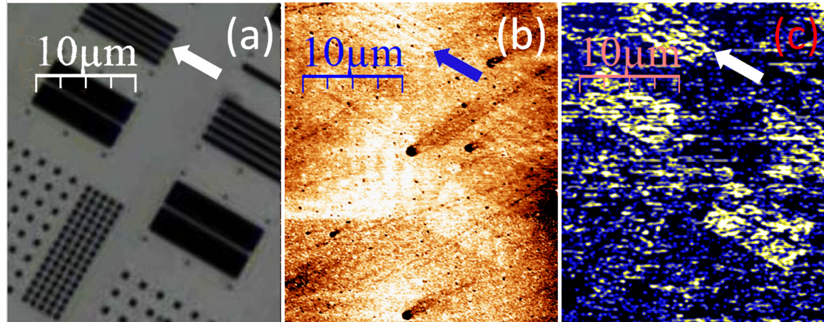

Figure 6.1 A comparison of (a) SEM image of the silicon stencil mask, (b) AFM topography and (c) 2D current map of the YBCO film surface after He^+ ion irradiation.

6.2 C-AFM characterization ion beam patterned HTSC films

The ion-induced modification of the electrical conductivity of the film on the micrometer scale was investigated by means of C-AFM. For C-AFM measurements we used conductive diamond coated (boron doped) CDT-NCHR probes from Nanosensors^{TM}. For 2D current mapping a sample bias of +5 V was applied to the sample. The measurements have been performed under ambient conditions using a DI Nanoscope IIIa AFM equipped with a home-made amplifier described in Sec. 2.1. Topographic signals (surface corrugation) and electrical

signals (spreading current) of film samples were recorded simultaneously. The influence of He^+ ion irradiation on the morphology and electrical properties of YBCO film is clearly visible in Fig. 6.1 where the SEM image of the Si tensile mask is depicted simultaneously with the resulting AFM topography and C-AFM 2D current map. The 50×50 μm topography

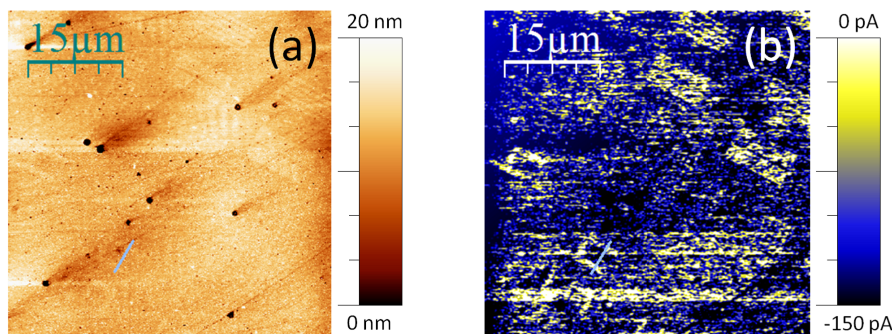

Figure 6.2 50μm×50 μm topography (a) with the corresponding current map (b) recorded on the surface of a planarized YBCO film after He^+ ion irradiation. The current map was recorded at +5 V of sample bias.

image (Fig. 6.2(a)) reveals an almost flat YBCO film surface with the roughness less than 10 nm (excluding defect surface areas). The patterned microstripes are hardly or not visible in the topography image due to their small relative height (±1 nm). In order to demonstrate that the contrast is not influenced by the surface corrugation we took a cross-section from the region with the minimal surface roughness. The correlation between the topography and current map cross-sections depicted as blue lines in Fig. 6.2 are presented in Fig. 6.3. Regardless the surface roughness, the micro-stripes from He^+ irradiated areas, can be easily

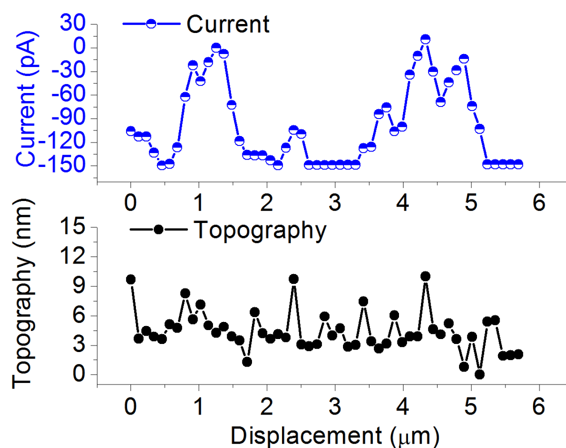

Figure 6.3 The comparison of the topography and current cross sections marked by blue lines in Fig. 6.2 (a) and (b), respectively.

distinguished in the current map. Since the C-AFM has been carried out under ambient conditions, the presence of a water film on the surface is unavoidable and slightly distorts the experiment inducing the appearance of interruptions in the current map. Hence, the resolution of the C-AFM measurements is limited and affected by some noise. Therefore, the small squares within the pattern of the mask are not clearly detectable by C-AFM. The

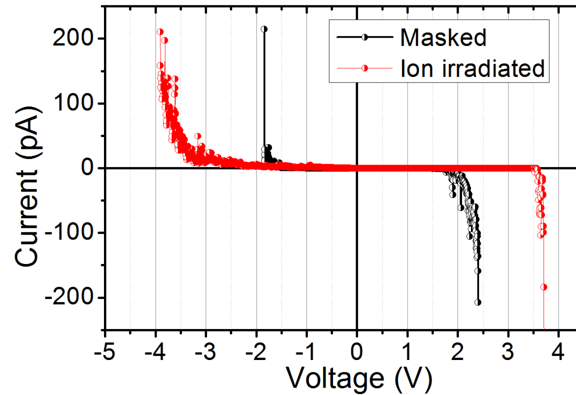

Figure 6.4 I-V characteristics recorded from the masked and ion-irradiated regions of YBCO thin film.

I-V characteristics were recorded using C-AFM from the masked and He^+ ion-irradiated positions on the surface of the YBCO film, respectively. The results are presented in Fig. 6.4. The I-V curves obtained at both positions were almost symmetrical, however, the I-V characteristic recorded from the masked region demonstrate significantly lower pseudo-breakdown voltage [30] compared to the characteristics recorded from the He^+ ion irradiated region. The characteristics are consistent with the contrast observed in the 2D current maps, indicating lower conductivity of the He^+ ion irradiated regions.

In conclusion, the C-AFM technique has been successfully applied to investigate the influence of He^+ irradiation on the electrical properties of the thin films of YBCO. Both, 2D current maps and I-V characteristics reveal the irradiation induced changes in the electrical properties of YBCO.

Chapter 7

Conclusions and Outlook

In the present work, conductive probe based AFM techniques, in particular, C-AFM, KPFM, and PC-AFM, have been applied to the electrical characterization of electronic and opto-electronic materials at the nanometer scale. The applicability of C-AFM and related methods for the investigation of low-dimensional semiconductor structures with potential for photodetector-, semiconductor laser-, and solar cell- applications has been demonstrated for several examples.

During the course of our investigations we examined epitaxially grown InAs nanostructures, namely nanowires, nanodots and quantum rings. C-AFM has been used to investigate the growth morphologies and electrical properties of InAs grown by conventional and atomic hydrogen-assisted MBE on self-organized GaAs(110) vicinal substrates with step bunches oriented along different crystallographic directions. Along with the investigation of electrical properties of conventionally grown InAs nanowires, we investigated the effect of atomic hydrogen and step orientation on the growth behavior of InAs. The measurements have been performed both under ambient conditions and in UHV. The experiments carried out in UHV are demonstrating much higher stability of the imaging conditions compared to those which were performed under ambient conditions. It has been shown that conventionally grown samples exhibit higher conductivity along $[1\bar{1}0]$ oriented step bunches, where preferential nucleation of InAs nanowires takes place by step decoration. On H-terminated substrates with triangular terraces bounded by $[1\bar{1}5]$ and $[\bar{1}15]$ steps, three-dimensional InAs clusters grow selectively at the terrace apexes. Along with InAs NWs and NDs we also investigated electrical properties of InAs QRs. C-AFM under UHV is demonstrated to be a valuable tool in compositional analysis of these self-assembled structures, however, further investigations are needed.

For GaInP thin films grown by MOVPE on vicinal Ge(100), a combination of C-AFM and KPFM measurements has been performed to study the electrical properties of so called arrowhead defects. In particular, we measured local current-to voltage characteristics of the terminating planes of the ADs and attributed them to the bucking voltage (related to contact potential difference) measured by KPFM. It has been found that the terminating planes of the AD consist of two alternating sub-planes which are about 12° and 6° inclined towards

the (100) plane corresponding most likely to {105} and {109} facets. The topographical analysis of the ADs suggests that the terminating planes are morphologically identical. At the same time, we observed that the electrical behavior of the ADs significantly differs from the behavior of the defect-free surface. Interestingly, the terminating planes appear different relative to each other with respect to their electrical properties both in C-AFM and KPFM. Specifically, the current densities (C-AFM) for the two terminating planes amount to (-278±35) and (-445±35) μA/m^2, respectively, while this value drops to (-20±35) μA/m^2 for the defect-free surface. In turn, the bucking voltage (KPFM) value for the ADs differs from the value for the surrounding film up to ~100 meV. According to Leng et al. [102] and Lee et al. [103], we conclude that the ADs in GaInP/Ge are composed most likely from material with a higher degree of order. However, the origin of the bucking voltage difference between the AD and its surrounding is still an open question. In order to clarify this issue, photoconductive AFM (PC-AFM) can be applied in the future.

A significant part of the presented results was devoted to C-AFM and PC-AFM based investigations of electrical and optical properties of upright standing ZnO NRs, a very challenging task since both methods are performed in contact mode. The electrical properties of arrays of upright standing ZnO NRs were characterized via two-dimensional current maps measured at different bias voltages applied to the sample. Further, C-AFM was utilized to determine the local current-to-voltage (I-V) characteristics of the top and side facets of individual upright standing NRs. These measurements reveal that the Schottky barrier heights of the contacts formed between the ZnO NRs and the diamond coated quasi-metallic tip (the work function is about 5.7 eV) equal to ~ 0.54 eV and ~ 0.48 eV for the top and side planes, respectively. A novel PC-AFM technique has been implemented to study the electrical transport in individual upright standing ZnO NRs under illumination from the top. The current passing through the AFM tip was measured as a function of time, illumination intensity, and/or wavelength. I-V curves taken from the top facet of a single upright standing NR under illumination appears more degraded with respect to the non-illuminated state. Further, we pioneered the application of PC-AFM to resolve the photoconductivity spectra measured from a single, upright standing ZnO NR. The corresponding photocurrent spectrum revealed that the minimum photon energy sufficient for photocurrent excitation is 3.1 eV. This value turned out to be ~100 meV lower than the band gap energy determined from the photoluminescence experiments. Therefore, it has been concluded that the photocurrent in this region can not be simply explained via band-to-band transition with subsequent electron-hole pair generation and oxygen desorption as it was explained in the framework of recent models [141]. Indeed, we believe that the phenomenon of the persistent conductivity is attributed to the presence of defect states in the band gap. In fact our experimental findings stay in a good agreement with theoretical predictions based on density functional theory calculations [143].

Finally, C-AFM - for the first time - applied to HTSC materials yielded a clear difference in the electrical properties between ion irradiated and masked areas. The 2D current map contrast has been analyzed in terms of cross-sectional analysis, and a correlation between the topography and current profiles was observed. The results have been confirmed by I-V

spectroscopy performed at specific locations. These results demonstrate the potential of C-AFM technique for high-resolution evaluation of HTSC circuits.

The immense potential of conductive probe based AFM techniques for characterization of a broad range of materials is obvious. The current understanding of underlaying physical mechanism along with the development of methodology and technical realization, however, bears large room for improvements. In the following, several ongoing projects are briefly introduced.

First of all, the implementation of UHV counterparts of techniques currently used under ambient conditions such as PC-AFM and PA-KPFM is vital. Here, a constructive problem is to avoid coupling of mechanical oscillations to the AFM stage by the glass fiber. Further, for both, UHV and ambient, setups it is important to decouple the influence of the feedback laser (preferentially used to detect cantilever bending) and the illumination source. Staying under the illumination from two light sources at the same moment, the conductivity of the sample may be influenced by each of them, therefore, making the obtained data hard to interpret. In order to avoid the above-mentioned problem one can use additional modulation of the feedback loop laser. When coupled with the lock-in technique this will allow to detect the photocurrent from the illumination laser separately, if the light from the illumination source is modulated as well [73]. It is also possible to overcome this problem by using a piezoresistive cantilever with a conductive tip as it was demonstrated in [147].

With respect to ZnO NRs it is well known that their piezoelectric properties can be accessed via the well-established PFM technique [26]. Since conductivity and free charge carrier concentration are interrelated quantities, the influence of the latter on the piezoelectric response can be studied by combined C-AFM and PFM measurements. Fig. 7.1 shows the

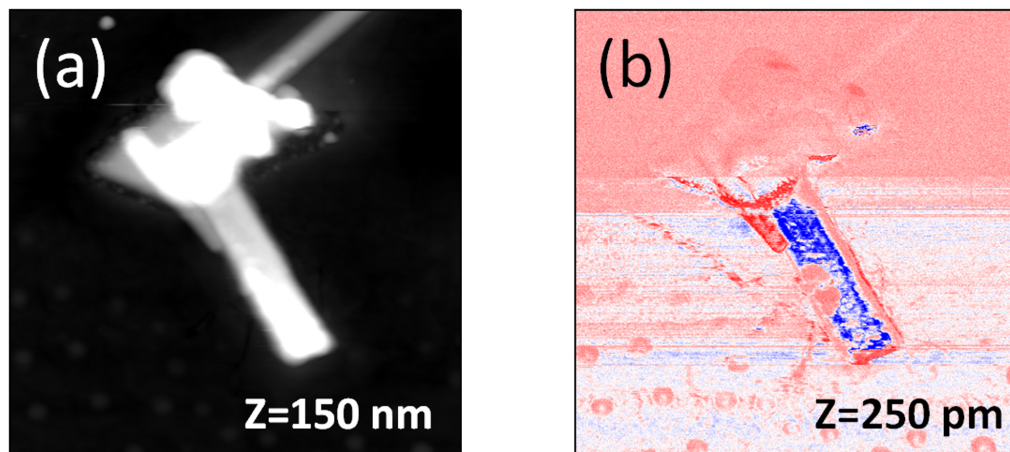

Figure 7.1 (a) Topography and (b) corresponding PFM amplitude images recorded in DART mode of PFM from a single lying ZnO NR.

first results obtained by dual amplitude resonance tracking (DART) PFM [148]. The PFM

amplitude image recorded on a side plane of a single ZnO NR contacted with the help of focused ion beam lithography demonstrates a piezo-response of ∼30 pm/V.

Finally, photo-assisted techniques like PC-AFM and PA-KPFM can also be successfully applied for the characterization of organic solar cells. Preliminary measurements have been performed using a newly implemented closed cell for measurements in inert atmosphere with the possibility to carry out experiments at elevated temperatures. The scheme of the experiment for the investigation of an organic solar cell in a configuration with illumination from the top is depicted in Fig. 7.2. In this respect, it is also planned to incorporate an external source meter in order to perform C-AFM and PC-AFM experiments using high electric fields. This will provide big advantage for characterization of low conductive organic thin films and will enable easier analysis of the numerical data.

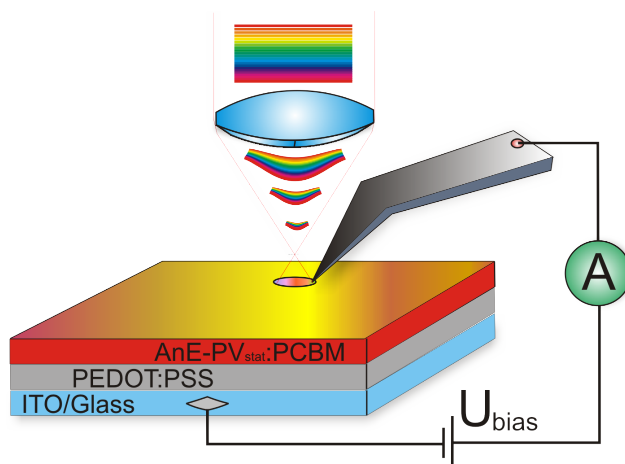

Figure 7.2 Schematic drawing of the experiment on the opto-electrical characterization of AnE-PV$_{stat}$:PCBM blends.

List of Figures

2.1 Schematic drawing of the C-AFM setup. 6
2.2 Schematic drawing of the Kelvin probe force microscopy (KPFM) setup. . . 13
2.3 The tip and cantilever derivative contributions are plotted simultaneously. The tip contribution becomes "visible" at the tip-to-sample separation equal to 15 nm or less for a given set of parameters. (example is taken from [63]) . 15
2.4 SEM image of AdvancedTEC probe from Nanosensors [71] used in conductive probe based AFM experiments under illumination. 18
2.5 Schematic drawing of the photoconductive AFM (PC-AFM) setups presented in the literature so far: illumination from the back side (a) of the sample, oblique illumination from the top (b) 18
2.6 Possible mechanisms of light absorption in semiconductors. 20
2.7 Schematic drawing of the implemented PC-AFM setup employing lock-in detection principle. 23
2.8 Schematic drawing of the modified PC-AFM setup using AdvancedTEC conductive probes. The sample in the present configuration is illuminated from the top side and biased. Conductive, Pt- coated ATEC-CONTPt^{TM} probes are used to avoid shadowing of the area under investigation by the cantilever. 24

3.1 Schematic representation of self-organized GaAs(110) substrates used for the growth of supported InAs NWs (a) and NDs (b). 28
3.2 2.5 μm$\times$2.5 μm topography image of InAs/GaAs NWs measured under ambient conditions (a) and 2D current map recorded at -5 V of sample bias (b) (from [29]). 29
3.3 C-AFM results of InAs NW on GaAs recorded in UHV. 2.5 μm$\times$ 2.5 μm topography image (a), 2D current map recorded at -9.1 V of sample bias (b) (from [29]). 30
3.4 Cross-sections along the line marked in Fig. 3.3; (a), schematic drawing of InAs NWs growth on the giant steps of the GaAs surface (b). Comparatively small amounts of InAs on the $[1\bar{1}2]$ and $[\bar{1}12]$ edges depicted by the *dashed line* (from [29]). 30

3.5 C-AFM results of InAs/GaAs NDs measured under UHV conditions. 2.5 μm$\times$2.5 μm topography image (a), 2D current map recorded at -9.1 V sample bias (b) (from [29]). 32
3.6 Topography and corresponding 2D current map cross-sections (a) along the lines marked in Fig. 3.5, current peaks are marked by arrows. Schematic drawing of InAs ND growth on the terrace apexes of GaAs surface is presented in (b) (from [29]). 32
3.7 The I-V curves recorded from the NW region (a) and the terrace free of InAs (b) of the conventionally grown sample (template A). 34
3.8 Possible mechanism for the self-assembled InAs quantum ring formation (adapted from [96]). First, InAs quantum dots are epitaxially grown on GaAs and followed by the deposition of a 2 nm capping GaAs layer with 30 s annealing at 490 °C (b). The InAs transport from the central hole and mixing with GaAs is denoted by arrows. The resulting structure is schematically depicted in (c). 37
3.9 Contact (a) and intermittent contact (b) mode topography AFM images of InGaAs quantum ring sample containing some small amounts of As_4 residuals (seen as small white spots of random shape) in addition to the QRs. 38
3.10 Topography acquired in contact mode under ambient conditions (a) and cross-sections (b) taken from the topography image and corresponding 2D autocorrelation hight map. The 2D ACM is given as inset in (b). 38
3.11 C-AFM images of InGaAs quantum rings recorded in UHV: topography (a), current map (b) and corresponding cross-sections (c) taken along the white lines indicated in (a) and (b). The images were acquired in contact mode AFM at +2 V of sample bias. 40
3.12 C-AFM images of InGaAs quantum rings recorded in UHV: topography (a), current map (b) and corresponding cross-sections (c) recorded along the white lines marked in (a) and (b). The images were acquired in contact mode AFM at -2 V of sample bias. 41
3.13 2D autocorrelation maps of the topography (a) and corresponding current map (b) recorded in contact mode AFM at -2 V sample bias. A comparison of the topography and current map ACM cross-sections (c) taken at 45° with respect to the fast scan line direction. A possible decomposition of the topography ACM cross-section into several peaks is presented in (d). 42
3.14 Schematic drawings of the C-AFM measurement of QRs performed using diamond coated tip (a), and possible compositional distribution within a single InGaAs QR (b). 43
3.15 The effect of As_4 residuals on the topography and current maps. The images acquired in contact mode AFM at -2 V of sample bias. 2 μm$\times$2 μm and 1 μm$\times$1 μm topography images (a,c) with the corresponding current maps (b,d) were recorded from the same sample after the first cycle of uncapping. 44

4.1 3D AFM image of arrowhead defects on the surface of InGaP/Ge(100) (a) recorded in intermittent contact mode. Analysis of the cross-sectional profiles taken along [001] and [0$\bar{1}$0], respectively, reveals that both terminating planes (L and R) are composed of alternating facets of {105} and {109} type, which are tilted with respect to (100) by about 12° and 6°, respectively (b) (From [35]). 49
4.2 C-AFM investigation of arrow head defects. Morphology image (a) and corresponding two dimensional current map recorded at -3 V (b). The current map of the arrowhead defect reveals a different conductivity for (L) and (R) terminating planes. (F) and (B) denote the surrounding film and the back side of the AD, respectively. 50
4.3 Current-voltage curves recorded for several (L) and (R) planes of the arrowhead defects (a), surrounding film (F) and the back side (B) of the AD (b). The I-V curves exhibit degradation of the conductivity for the (L) facet relative to the (R) facet. 51
4.4 KPFM results representing topography (a) simultaneously acquired with the bucking voltage (b) of the ADs. While the value of the contact potential difference for the (L) plane differs by ∼70 meV from the value found for the surrounding, no difference for the (R) plane was observed. 51

5.1 5 μm×5 μm intermittent contact mode image of ZnO nanorods grown by TE (a) and 2.5 μm×2.5 μm tapping mode image of HT grown samples (b) with the corresponding cross-sections depicted in (c) and (d). 57
5.2 Height distribution plots of (a) TE and (b) HT sample taken from the 10 μm intermittent contact mode AFM images of arrays of upright standing ZnO NRs grown on FTO. 58
5.3 (a) Intermittent contact mode AFM image of ZnO NRs grown on FTO. The diameter of the ZnO varied in a wide range from 150 to 1200 nm, the length of the NRs was $\sim 2.5\ \mu m$ as it was determined from the comparison of SEM and AFM data. (b) XRD spectrum of the ZnO NRs perpendicular to the sample surface. XRD intensity over the reciprocal lattice vector q_z along the [0001] direction. ZnO bulk Bragg peak positions and intensities are marked as dashed lines and crosses, respectively. 59
5.4 Time-resolved and integral spectra from the array of upright standing ZnO nanorods, of photoluminescence obtained at 300 K. The red curve shows the steady-state photoluminescence spectrum each point on the plot averages the photoluminescence signal measured over approximately 1 sec. The blue curve represents a time-resolved photoluminescence spectrum where each point was measured in the time slot from 0 to 0.7 ns from the moment of excitation. . 60
5.5 (a) Contact mode AFM image of ZnO NRs grown by thermal evaporation on Si(111). (b) The I-V characteristic recorded from the center of the NR marked in (a) with an arrow. (After [36]). 63

5.6 2.5 μm$\times$1.25 μm C-AFM images of ZnO nanorods grown by TE on Si: (a) topography, (b) current map at -0.5 V, (c) topography and current cross-sections taken across the edge of the NR as marked in (a) and (b). 64
5.7 C-AFM images of ZnO NRs grown on FTO. 2D (a) and 3D (b) topography images of ZnO NRs reveal the presence of step bunch-like structures at the side plane instead of a singular facet. The current maps recorded at +0.1 V of sample bias in forward (c) and backward (d) directions demonstrate the presence of current spikes which appear seemingly at the edges within the side plane. 65
5.8 First derivative of the forward current map presented in Fig. 5.7(c). 66
5.9 Correlation between the topography, current, and current derivative profiles taken from the locations marked by correspondently colored lines in Fig. 5.7(a), (c) and Fig. 5.8. 67
5.10 Scheme of the experiment for the case of a TE grown sample. 68
5.11 (a) I-V curves recorded from HT grown NR on FTO, (b) Forward I-V characteristics recorded from the top facet (circles, black) and side plane (triangles, red) of a tilted TE grown ZnO NR. The characteristics revealing a significant difference between turn-on voltages. 68
5.12 Forward I-V characteristics recorded from the top facet (half-filled circles, black) and side plane (filled circles, red) of a tilted TE grown ZnO NR linearized in logarithmic scale. The fits (blue lines) were used to determine the Schottky barrier heights and ideality factors. 69
5.13 Topography of a ZnO NR lying on an insulating substrate (native oxide covered silicon wafer) and contacted with tungsten by FIB. This setup is planned to use for C-AFM inspection of the NR side facets. 72
5.14 Current-to-voltage characteristics of dark (green curve, circles) and illuminated state (red curve, triangles) recorded from a single upright standing ZnO nanorod. The illuminated characteristic was recorded using a Xe 150W lamp (white light) as light source. 73
5.15 Photocurrent rise and relaxation during the first cycle of the experiment. The bias of -10 V was applied at 0 s, the yellow bar (shadowed rectangular area) indicates the initial dark current decay. After sample was illuminated it is clearly visible that photoconductivity persists for about 1835 s and then decays exponentially. 74
5.16 The plot demonstrates the course of the experiment over several cycles of the illumination. The sample bias is -10 V, the source of illumination is a 150 W Xe lamp (white light source). 75
5.17 The photoconductivity spectral response from a single upright standing ZnO NR recorded using a 150 W Xe lamp connected to the monochromator. The sample bias was -10 V. The spectrum was recorded starting from the lower energies withstanding the interval of $\sim$30 sec between the points. 76

5.18 Schematic energy-level diagram of ZnO taking into account the existence of theoretically predicted [143] $\alpha-$ and $\beta-$ type states of oxygen vacancies. The processes of electron-hole pair generation, charge carrier photo-excitation from DLS and to PHS states of oxygen vacancy are marked as (1), (2), and (3), respectively. 77
5.19 The quantum efficiency of light conversion linearized in coordinates $(I_{PN}\hbar\omega)$ $vs.$ $\hbar\omega$. The extrapolation until $I_{PN}\hbar\omega = 0$ provides the energy corresponding to the transition involved in the photocarrier generation process. 78

6.1 A comparison of (a) SEM image of the silicon stencil mask, (b) AFM topography and (c) 2D current map of the YBCO film surface after He^+ ion irradiation. 82
6.2 50μm$\times$50 μm topography (a) with the corresponding current map (b) recorded on the surface of a planarized YBCO film after He^+ ion irradiation. The current map was recorded at +5 V of sample bias. 83
6.3 The comparison of the topography and current cross sections marked by blue lines in Fig. 6.2 (a) and (b), respectively. 83
6.4 I-V characteristics recorded from the masked and ion-irradiated regions of YBCO thin film. 84

7.1 (a) Topography and (b) corresponding PFM amplitude images recorded in DART mode of PFM from a single lying ZnO NR. 87
7.2 Schematic drawing of the experiment on the opto-electrical characterization of AnE-PV$_{\text{stat}}$:PCBM blends. 88

List of publications:

[1] **I. Beinik**, B. Galiana, M. Kratzer, C. Teichert, I. Rey-Stolle, C. Algora, and P. Tejedor. Nanoscale electrical characterization of arrowhead defects in GaInP thin films grown on Ge. *Journal of Vacuum Science & Technology B: Microelectronics and Nanometer Structures*, 28(4):C5G5, 2010.

[2] Christian Teichert and **Igor Beinik**. Conductive Atomic-Force microscopy investigation of nanostructures in microelectronics. In Bharat Bhushan, editor, *Scanning Probe Microscopy in Nanoscience and Nanotechnology 2*, pages 691–721. Springer, Berlin Heidelberg, 2011.

[3] Paloma Tejedor, Laura Díez-Merino, **Igor Beinik**, and Christian Teichert. Conductive atomic force microscopy study of InAs growth kinetics on vicinal GaAs (110). *Applied Physics Letters*, 95(12):123103, 2009.

[4] Gerhard Brauer, Wolfgang Anwand, Dieter Grambole, Werner Egger, Peter Sperr, **Igor Beinik**, Lin Wang, Christian Teichert, Jan Kuriplach, Jan Lang, Sergei Zviagin, Erik Cizmar, Chi Chung Ling, Yuk Fan Hsu, Yan Yan Xi, Xinyi Chen, A B Djurišić, and Wolfgang Skorupa. Characterization of ZnO nanostructures: A challenge to positron annihilation spectroscopy and other methods. *physica status solidi (c)*, 6(11):2556–2560, 2009.

[5] A. Kadashchuk, S. Schols, P. Heremans, Yu. Skryshevski, Yu. Piryatinski, **I. Beinik**, C. Teichert, G. Hernandez-Sosa, H. Sitter, A. Andreev, P. Frank, and A. Winkler. Origin of the low-energy emission band in epitaxially grown para-sexiphenyl nanocrystallites. *The Journal of Chemical Physics*, 130(8):084901, 2009.

[6] J.D. Pedarnig, K. Siraj, M.A. Bodea, I. Puica, W. Lang, R. Kolarova, P. Bauer, K. Haselgrübler, C. Hasenfuss, **I. Beinik**, and C. Teichert. Surface planarization and masked ion-beam structuring of $YBa_2Cu_3O_7$ thin films. *Thin Solid Films*, 518(23):7075–7080, 2010.

[7] W. Lang, M. Marksteiner, M.A. Bodea, K. Siraj, J.D. Pedarnig, R. Kolarova, P. Bauer, K. Haselgrübler, C. Hasenfuss, **I. Beinik**, and C. Teichert. Ion beam irradiation of cuprate high-temperature superconductors: Systematic modification of the electrical

properties and fabrication of nanopatterns. *Nuclear Instruments and Methods in Physics Research Section B: Beam Interactions with Materials and Atoms*, In Press, Available online: 10.1016/j.nimb.2011.01.087

[8] B. Galiana, I. Rey-Stolle, **I. Beinik**, C. Algora, C. Teichert, J.M. Molina-Aldareguia, and P. Tejedor. Characterization of antiphase domains on GaAs grown on ge substrates by conductive atomic force microscopy for photovoltaic applications. *Solar Energy Materials and Solar Cells*, In Press, Available online: doi:10.1016/j.solmat.2010.12.021

[9] A. Kadashchuk, Y. Skryshevski, **I. Beinik**, C. Teichert, G. Hernandez-Sosa, H. Sitter, A. Andreev, P. Frank, and A. Winkler. Spectroscopy of defects in epitaxially grown para-sexiphenyl nanostructures. *Springer Proceedings in Physics*, 129:121, 2009.

[10] Kartik Pondicherry, **Igor Beinik**, Florian Grün, Istvan Godor, and Christian Teichert. Application of conductive AFM technique to measure electrical conductance of tribofilms. In Lehrstuhl für Allgemeinen Maschinenbau, editor, *Proceedings of 26th Danubia-Adria Symposium on Advances in Experimental Mechanics*, pages 205 – 206, September 2009.

[11] Christian Teichert, Yue Hou, **Igor Beinik**, Xinyi Chen, Y. F. Hsu, Aleksandra B. Djurisic, Wolfgang Anwand, and Gerhard Brauer. Scanning probe microscopy-based characterization of ZnO nanorods. In *2010 3rd International Nanoelectronics Conference (INEC)*, pages 438–439, Hong Kong, China, 2010.

[12] **I. Beinik**, M. Kratzer, A. Wachauer, L. Wang, R. T. Lechner, C. Teichert, C. Motz, W. Anwand, G. Brauer, X. Y. Chen, Y. F. Hsu, and A. B. Djurisic. Electrical properties of ZnO nanorods studied by conductive atomic force microscopy. Submitted to *Journal of Applied Physics*, Jan. 2011.

Bibliography

[1] Ohno, Y., Terauchi, R., Adachi, T., Matsukura, F., and Ohno, H. *Physical Review Letters* **83**(20), 4196 November (1999).

[2] Hall, K. C., Gündoğdu, K., Hicks, J. L., Kocbay, A. N., Flatté, M. E., Boggess, T. F., Holabird, K., Hunter, A., Chow, D. H., and Zinck, J. J. *Applied Physics Letters* **86**(20), 202114 (2005).

[3] García, J. M., Medeiros-Ribeiro, G., Schmidt, K., Ngo, T., Feng, J. L., Lorke, A., Kotthaus, J., and Petroff, P. M. *Applied Physics Letters* **71**(14), 2014 (1997).

[4] Joyce, P. B., Krzyzewski, T. J., Bell, G. R., and Jones, T. S. *Applied Physics Letters* **79**(22), 3615 (2001).

[5] Warburton, R. J., Schaflein, C., Haft, D., Bickel, F., Lorke, A., Karrai, K., Garcia, J. M., Schoenfeld, W., and Petroff, P. M. *Nature* **405**(6789), 926–929 June (2000).

[6] Kleemans, N. A. J. M., Bominaar-Silkens, I. M. A., Fomin, V. M., Gladilin, V. N., Granados, D., Taboada, A. G., García, J. M., Offermans, P., Zeitler, U., Christianen, P. C. M., Maan, J. C., Devreese, J. T., and Koenraad, P. M. *Physical Review Letters* **99**(14), 146808 October (2007).

[7] Lorke, A., Luyken, R. J., Govorov, A. O., Kotthaus, J. P., Garcia, J. M., and Petroff, P. M. *Physical Review Letters* **84**(10), 2223 March (2000).

[8] Offermans, P., Koenraad, P. M., Wolter, J. H., Granados, D., Garcia, J. M., Fomin, V. M., Gladilin, V. N., and Devreese, J. T. *Applied Physics Letters* **87**(13), 131902 (2005).

[9] King, R. R., Law, D. C., Edmondson, K. M., Fetzer, C. M., Kinsey, G. S., Yoon, H., Sherif, R. A., and Karam, N. H. *Applied Physics Letters* **90**(18), 183516 (2007).

[10] Wang, Z. L. *Materials Science and Engineering: R: Reports* **64**(3-4), 33–71 April (2009).

[11] Djurisic, A., Ng, A., and Chen, X. *Progress in Quantum Electronics* **34**(4), 191–259 July (2010).

[12] Law, M., Greene, L. E., Johnson, J. C., Saykally, R., and Yang, P. *Nature Materials* **4**(6), 455–459 (2005).

[13] Galoppini, E., Rochford, J., Chen, H., Saraf, G., Lu, Y., Hagfeldt, A., and Boschloo, G. *The Journal of Physical Chemistry B* **110**(33), 16159–16161 (2006).

[14] Hsu, Y. F., Xi, Y. Y., Djurišić, A. B., and Chan, W. K. *Applied Physics Letters* **92**(13), 133507 (2008).

[15] Cheng, K., Cheng, G., Wang, S., Li, N., Dai, S., Zhang, X., Zou, B., and Du, Z. *New Journal of Physics* **9**, 214 (2007).

[16] Wang, Z. L. and Song, J. *Science* **312**(5771), 242 –246 April (2006).

[17] Alexe, M., Senz, S., Schubert, M. A., Hesse, D., and Gösele, U. *Advanced Materials* **20**(21), 4021–4026 (2008).

[18] Scrymgeour, D. A. and Hsu, J. W. P. *Nano Letters* **8**(8), 2204–2209 (2008).

[19] Guo, W., Yang, Y., Liu, J., and Zhang, Y. *Phys. Chem. Chem. Phys.* **12**(45), 14868–14872 (2010).

[20] O'Shea, S. J., Atta, R. M., Murrell, M. P., and Welland, M. E. *Journal of Vacuum Science & Technology B: Microelectronics and Nanometer Structures* **13**(5), 1945 (1995).

[21] Abraham, D. W., Williams, C., Slinkman, J., and Wickramasinghe, H. *Journal of Vacuum Science & Technology B: Microelectronics and Nanometer Structures* **9**(2), 703 (1991).

[22] Dreyer, M. and Wiesendanger, R. *Applied Physics A Materials Science & Processing* **61**(4), 357–362 (1995).

[23] Sakaguchi, H., Iwata, F., Hirai, A., Sasaki, A., and Nagamura, T. *Japanese Journal of Applied Physics* **38**(Part 1, No. 6B), 3908–3911 (1999).

[24] Coffey, D. C., Reid, O. G., Rodovsky, D. B., Bartholomew, G. P., and Ginger, D. S. *Nano Letters* **7**(3), 738–744 March (2007).

[25] Nonnenmacher, M., O'Boyle, M. P., and Wickramasinghe, H. K. *Applied Physics Letters* **58**(25), 2921 (1991).

[26] Gruverman, A. *Journal of Vacuum Science & Technology B: Microelectronics and Nanometer Structures* **14**(2), 602 (1996).

[27] Murrell, M. P., Welland, M. E., O'Shea, S. J., Wong, T. M. H., Barnes, J. R., McKinnon, A. W., Heyns, M., and Verhaverbeke, S. *Applied Physics Letters* **62**(7), 786 (1993).

[28] Kremmer, S., Teichert, C., Pischler, E., Gold, H., Kuchar, F., and Schatzmayr, M. *Surface and Interface Analysis* **33**(2), 168–172 (2002).

[29] Teichert, C. and Beinik, I. In *Scanning Probe Microscopy in Nanoscience and Nanotechnology 2,* Bhushan, B., editor, 691–721. Springer, Berlin Heidelberg (2011).

[30] Kremmer, S., Wurmbauer, H., Teichert, C., Tallarida, G., Spiga, S., Wiemer, C., and Fanciulli, M. *Journal of Applied Physics* **97**(7), 1–7 (2005).

[31] Bierwagen, O., Geelhaar, L., Gay, X., Piešiņš, M., Riechert, H., Jobst, B., and Rucki, A. *Applied Physics Letters* **90**(23), 232901 (2007).

[32] Lanza, M., Porti, M., Nafria, M., Benstetter, G., Frammelsberger, W., Ranzinger, H., Lodermeier, E., and Jaschke, G. *Microelectronics Reliability* **47**(9-11), 1424–1428 (2007).

[33] Martin, D., Grube, M., Weber, W. M., Rüstig, J., Bierwagen, O., Geelhaar, L., and Riechert, H. *Applied Physics Letters* **95**(14), 142906 (2009).

[34] Tejedor, P., Díez-Merino, L., Beinik, I., and Teichert, C. *Applied Physics Letters* **95**(12), 123103 (2009).

[35] Beinik, I., Galiana, B., Kratzer, M., Teichert, C., Rey-Stolle, I., Algora, C., and Tejedor, P. *Journal of Vacuum Science & Technology B: Microelectronics and Nanometer Structures* **28**(4), C5G5 (2010).

[36] Brauer, G., Anwand, W., Grambole, D., Egger, W., Sperr, P., Beinik, I., Wang, L., Teichert, C., Kuriplach, J., Lang, J., Zviagin, S., Cizmar, E., Ling, C., Hsu, Y., Xi, Y., Chen, X., Djurišić, A., and Skorupa, W. *Physica Status Solidi (C) Current Topics in Solid State Physics* **6**(11), 2556–2560 (2009).

[37] Schloffer, M., Teichert, C., Supancic, P., Andreev, A., Hou, Y., and Wang, Z. *Journal of the European Ceramic Society* **30**(7), 1761–1764 (2010).

[38] Eyben, P., Janssens, T., and Vandervorst, W. *Materials Science and Engineering: B* **124-125**, 45–53 (2005).

[39] Schaadt, D. M., Yu, E. T., Sankar, S., and Berkowitz, A. E. *Applied Physics Letters* **74**(3), 472 (1999).

[40] Wolf, P. D., Snauwaert, J., Clarysse, T., Vandervorst, W., and Hellemans, L. *Applied Physics Letters* **66**(12), 1530 (1995).

[41] Olbrich, A., Ebersberger, B., and Boit, C. *Applied Physics Letters* **73**(21), 3114 (1998).

[42] Aguilera, L., Lanza, M., Porti, M., Grifoll, J., Nafría, M., and Aymerich, X. *Review of Scientific Instruments* **79**(7), 073701 (2008).

[43] Aguilera, L., Polspoel, W., Volodin, A., Haesendonck, C. V., Porti, M., Vandervorst, W., Nafria, M., and Aymerich, X. *Journal of Vacuum Science & Technology B: Microelectronics and Nanometer Structures* **26**(4), 1445 (2008).

[44] Kremmer, S., Peissi, S., Teichert, C., and Kuchar, F. In *ISTFA 2002. Proceedings of the 28th International Symposium for Testing and Failure Analysis*, 473–82 (ASM Int, Materials Park, OH, USA, 2002).

[45] Kremmer, S., Peissl, S., Teichert, C., Kuchar, F., and Hofer, H. *Materials Science and Engineering B* **102**(1-3), 88–93 September (2003).

[46] Koeck, F. A. and Nemanich, R. J. *Diamond and Related Materials* **15**(2-3), 217–220 (2006).

[47] Kim, K., Moldovan, N., Ke, C., Espinosa, H. D., Xiao, X., Carlisle, J. A., and Auciello, O. *Small* **1**(8-9), 866–874 (2005).

[48] Weast, R. C. *CRC handbook of chemistry and physics: a ready-reference book of chemical and physical data*. CRC Press, (1977).

[49] Lin, C. M., Shen, S. Y., and Chen, J. *Journal of The Electrochemical Society* **158**(2), H146–H149 February (2011).

[50] Klaua, M., Ullmann, D., Barthel, J., Wulfhekel, W., Kirschner, J., Urban, R., Monchesky, T. L., Enders, A., Cochran, J. F., and Heinrich, B. *Physical Review B* **64**(13), 134411 (2001).

[51] Gröning, O., Küttel, O. M., Gröning, P., and Schlapbach, L. *Journal of Vacuum Science & Technology B: Microelectronics and Nanometer Structures* **17**(5), 1970 (1999).

[52] Lujan, G., Schram, T., Pantisano, T., Hooker, J., Kubicek, S., Rohr, E., Schuhmacher, J., Kilpela, O., Sprey, H., Gendt, S. D., and Meyer, K. D. In *Proceeding of the 32nd European*, 583–586, September (2002).

[53] Trenkler, T., Hantschel, T., Stephenson, R., Wolf, P. D., Vandervorst, W., Hellemans, L., Malavé, A., Büchel, D., Oesterschulze, E., Kulisch, W., Niedermann, P., Sulzbach, T., and Ohlsson, O. *Journal of Vacuum Science & Technology B: Microelectronics and Nanometer Structures* **18**(1), 418 (2000).

[54] Sze, S. M. and Ng, K. K. *Physics of semiconductor devices*. John Wiley and Sons, Hoboken, New Jersey, (2007).

[55] Tal, O., Epstein, I., Snir, O., Roichman, Y., Ganot, Y., Chan, C. K., Kahn, A., Tessler, N., and Rosenwaks, Y. *Physical Review B* **77**(20), 201201 May (2008).

[56] Reid, O. G., Munechika, K., and Ginger, D. S. *Nano Letters* **8**(6), 1602–1609 June (2008).

[57] Kremmer, S. *Applicability of conducting AFM for characterization and modification of thin silicon oxides*. PhD thesis, Leoben, Austria, November (2003).

[58] Fowler, R. H. and Nordheim, L. *Proceedings of the Royal Society of London. Series A* **119**(781), 173 –181 May (1928).

[59] Lenzlinger, M. *Journal of Applied Physics* **40**(1), 278 (1969).

[60] Zhang, H., Miller, E. J., and Yu, E. T. *Journal of Applied Physics* **99**(2), 023703 (2006).

[61] Mott, N. and Gurney, R. W. *Electronic Processes In Ionic Crystals*. Dover Publications Inc., Oxford, 2nd edition, (1964).

[62] Luginsland, J. W., Lau, Y. Y., and Gilgenbach, R. M. *Physical Review Letters* **77**(22), 4668 November (1996).

[63] Sarid, D. *Exploring scanning probe microscopy with mathematica*. Wiley-VCH, Weinheim, (2007).

[64] Jacobs, H. O., Knapp, H. F., and Stemmer, A. *Review of Scientific Instruments* **70**(3), 1756 (1999).

[65] Sadewasser, S., Glatzel, T., Shikler, R., Rosenwaks, Y., and Lux-Steiner, M. C. *Applied Surface Science* **210**(1-2), 32–36 March (2003).

[66] Müller, F. and Müller, A. *Journal of Vacuum Science & Technology B: Microelectronics and Nanometer Structures* **27**(2), 969 (2009).

[67] Sommerhalter, C., Glatzel, T., Matthes, T. W., Jäger-Waldau, A., and Lux-Steiner, M. C. *Applied Surface Science* **157**(4), 263–268 April (2000).

[68] Kronik, L. and Shapira, Y. *Surface Science Reports* **37**(1-5), 1–206 December (1999).

[69] Streicher, F., Sadewasser, S., Enzenhofer, T., Schock, H., and Lux-Steiner, M. *Thin Solid Films* **517**(7), 2349–2352 February (2009).

[70] Adamowicz, B. and Szuber, J. *Surface Science* **247**(2-3), 94–99 May (1991).

[71] http://www.nanosensors.com/AdvancedTEC.pdf.

[72] Lee, J., Choi, I., Hong, S., Lee, S., Yang, Y. I., Kim, Y., and Yi, J. *Ultramicroscopy* **108**(10), 1090–1093 (2008).

[73] Brezna, W., Strasser, G., and Smoliner, J. *Physica E: Low-dimensional Systems and Nanostructures* **40**(5), 1229–1231 March (2008).

[74] Pingree, L. S. C., Reid, O. G., and Ginger, D. S. *Nano Letters* **9**(8), 2946–2952 (2009).

[75] Heng, L., Tian, D., Chen, L., Su, J., Zhai, J., Han, D., and Jiang, L. *Chemical Communications* **46**(7), 1162 (2010).

[76] Wang, S., Zhang, X., Cheng, G., Jiang, X., Li, Y., Huang, Y., and Du, Z. *Chemical Physics Letters* **405**(1-3), 63–67 (2005).

[77] Takahashi, T., Takada, K., and Takeuchi, M. *Ultramicroscopy* **97**(1-4), 1–6 (2003).

[78] Tejedor, P., Crespillo, M. L., and Joyce, B. A. *Applied Physics Letters* **88**(6), 063101 (2006).

[79] Zhang, X. M., Pashley, D. W., Kamiya, I., Neave, J. H., and Joyce, B. A. *Journal of Crystal Growth* **147**(1-2), 234–237 (1995).

[80] McCoy, J. M. and LaFemina, J. P. *Physical Review B* **54**(20), 14511 November (1996).

[81] Liang, Y., Packard, W. E., Dow, J. D., Ho, H., and Lapeyre, G. J. *Physical Review B* **48**(16), 11942 October (1993).

[82] Nannarone, S. and Pedio, M. *Surface Science Reports* **51**(1-8), 1–149 September (2003).

[83] Michely, T. and Krug, J. *Islands, mounds, and atoms: patterns and processes in crystal growth far from equilibrium.* Springer-Verlag, Berlin Heidelberg, (2004).

[84] Porte, L. *Journal of Crystal Growth* **273**(1-2), 136–148 December (2004).

[85] Bales, G. S. and Zangwill, A. *Physical Review B* **55**(4), R1973 January (1997).

[86] Snyder, C. W. and Orr, B. G. *Physical Review Letters* **70**(7), 1030 February (1993).

[87] Ono, S., Takeuchi, M., and Takahashi, T. *Ultramicroscopy* **91**(1-4), 127–132 May (2002).

[88] Baier, H., Koenders, L., and Mönch, W. *Journal of Vacuum Science & Technology B: Microelectronics and Nanometer Structures* **4**(4), 1095 (1986).

[89] Biasiol, G., Magri, R., Heun, S., Locatelli, A., Mentes, T., and Sorba, L. *Journal of Crystal Growth* **311**(7), 1764–1766 March (2009).

[90] Mlakar, T., Biasiol, G., Heun, S., Sorba, L., Vijaykumar, T., Kulkarni, G. U., Spreafico, V., and Prato, S. *Applied Physics Letters* **92**(19), 192105 (2008).

[91] Granados, D., García, J. M., Ben, T., and Molina, S. I. *Applied Physics Letters* **86**(7), 071918 (2005).

[92] Tanaka, I., Kamiya, I., Sakaki, H., Qureshi, N., Allen, S. J., and Petroff, P. M. *Applied Physics Letters* **74**(6), 844 (1999).

[93] Yamamoto, H., Takahashi, T., and Kamiya, I. *Applied Physics Letters* **77**(13), 1994 (2000).

[94] Okada, Y., Miyagi, M., Akahane, K., Iuchi, Y., and Kawabe, M. *Journal of Applied Physics* **90**(1), 192 (2001).

[95] Biasiol, G., Heun, S., Golinelli, G. B., Locatelli, A., Mentes, T. O., Guo, F. Z., Hofer, C., Teichert, C., and Sorba, L. *Applied Physics Letters* **87**(22), 223106 (2005).

[96] Lorke, A., Luyken, R. J., Garcia, J. M., and Petroff, P. M. *Japanese Journal of Applied Physics* **40**(Part 1, No. 3B), 1857–1859 (2001).

[97] Tobin, S. P., Vernon, S. M., Bajgar, C., Haven, V. E., Geoffroy, L. M., and Lillington, D. R. *IEEE Electron Device Letters* **9**(5), 256–258 (1988).

[98] Karam, N. H., King, R. R., Haddad, M., Ermer, J. H., Yoon, H., Cotal, H. L., Sudharsanan, R., Eldredge, J. W., Edmondson, K., Joslin, D. E., Krut, D. D., Takahashi, M., Nishikawa, W., Gillanders, M., Granata, J., Hebert, P., Cavicchi, B. T., and Lillington, D. R. *Solar Energy Materials and Solar Cells* **66**(1-4), 453–466 February (2001).

[99] Galiana, B., Barrigón, E., Rey-Stolle, I., Corregidor, V., Espinet, P., Algora, C., and Alves, E. *Superlattices and Microstructures* **45**(4-5), 277–284 (2009).

[100] Chapman, D. C., Stringfellow, G. B., Bell, A., Ponce, F. A., Lee, J. W., Seong, T. Y., Shibakawa, S., and Sasaki, A. *Journal of Applied Physics* **96**(12), 7229–7234 (2004).

[101] Lankinen, A., Knuuttila, L., Kostamo, P., Tuomi, T. O., Lipsanen, H., McNally, P. J., and O'Reilly, L. *Journal of Crystal Growth* **311**(22), 4619–4627 (2009).

[102] Leng, Y., Williams, C. C., Su, L. C., and Stringfellow, G. B. *Applied Physics Letters* **66**(10), 1264 (1995).

[103] Lee, M. K., Horng, R. H., and Haung, L. C. *Applied Physics Letters* **59**(25), 3261–3263 (1991).

[104] Gomyo, A., Suzuki, T., and Iijima, S. *Physical Review Letters* **60**(25), 2645–2648 (1988).

[105] Pérez-García, B., Zúñiga-Pérez, J., Muñoz-Sanjosé, V., Colchero, J., and Palacios-Lidón, E. *Nano Letters* **7**(6), 1505–1511 June (2007).

[106] Moser, M., Geng, C., Lach, E., Queisser, I., Scholz, F., Schweizer, H., and Dörnen, A. *Journal of Crystal Growth* **124**(1-4), 333–338 (1992).

[107] Reynolds, C. L. and Grenko, J. A. *physica status solidi (a)* **206**(4), 691–696 (2009).

[108] Cruz, S. C., Keller, S., Mates, T. E., Mishra, U. K., and DenBaars, S. P. *Journal of Crystal Growth* **311**(15), 3817–3823 (2009).

[109] Fang, S. F., Adomi, K., Iyer, S., Morkoç, H., Zabel, H., Choi, C., and Otsuka, N. *Journal of Applied Physics* **68**(7), R31–R58 (1990).

[110] Martins, J. L. and Zunger, A. *Physical Review B* **30**(10), 6217–6220 (1984).

[111] Ichimura, M. and Sasaki, A. *Journal of Applied Physics* **60**(11), 3850–3855 (1986).

[112] Sasaki, A., Tsuchida, K., Narukawa, Y., Kawakami, Y., Fujita, S., Hsu, Y., and Stringfellow, G. B. *Journal of Applied Physics* **89**(1), 343–347 (2001).

[113] Baxter, C. S., Stobbs, W. M., and Wilkie, J. H. *Journal of Crystal Growth* **112**(2-3), 373–385 (1991).

[114] Baxter, J. B. and Aydil, E. S. *Applied Physics Letters* **86**(5), 053114 (2005).

[115] Olson, D. C., Piris, J., Collins, R. T., Shaheen, S. E., and Ginley, D. S. *Thin Solid Films* **496**(1), 26–29 February (2006).

[116] Ji, L. W., Shih, W. S., Fang, T. H., Wu, C. Z., Peng, S. M., and Meen, T. H. *Journal of Materials Science* **45**(12), 3266–3269 (2010).

[117] Lupan, O., Chow, L., and Chai, G. *Sensors and Actuators B: Chemical* **141**(2), 511–517 September (2009).

[118] Lupan, O., Chai, G., Chow, L., Emelchenko, G. A., Heinrich, H., Ursaki, V. V., Gruzintsev, A. N., Tiginyanu, I. M., and Redkin, A. N. *physica status solidi (a)* **207**(7), 1735–1740 (2010).

[119] Yadav, H. K., Sreenivas, K., and Gupta, V. *Applied Physics Letters* **96**(22), 223507 (2010).

[120] Hullavarad, S., Hullavarad, N., Look, D., and Claflin, B. *Nanoscale Research Letters* **4**(12), 1421–1427 (2009).

[121] Zhou, J., Gu, Y., Hu, Y., Mai, W., Yeh, P., Bao, G., Sood, A. K., Polla, D. L., and Wang, Z. L. *Applied Physics Letters* **94**(19), 191103 (2009).

[122] Kim, W. and Chu, K. S. *physica status solidi (a)* **206**(1), 179–182 (2009).

[123] Cheng, G., Li, Z., Wang, S., Gong, H., Cheng, K., Jiang, X., Zhou, S., Du, Z., Cui, T., and Zou, G. *Applied Physics Letters* **93**(12), 123103 (2008).

[124] Law, J. B. K. and Thong, J. T. L. *Applied Physics Letters* **88**(13), 133114 (2006).

[125] Guo, Z., Zhao, D., Liu, Y., Shen, D., Zhang, J., and Li, B. *Applied Physics Letters* **93**(16), 163501 (2008).

[126] Hu, Y., Zhou, J., Yeh, P., Li, Z., Wei, T., and Wang, Z. L. *Advanced Materials* **22**(30), 3327–3332 (2010).

[127] Chen, C., Chen, M., Ke, J., Lin, C., Retamal, J. R. D., and He, J. *Pure and Applied Chemistry* **82**, 2055–2073 (2010).

[128] Brauer, G., Anwand, W., Grambole, D., Skorupa, W., Hou, Y., Andreev, A., Teichert, C., Tam, K. H., and Djurišić, A. B. *Nanotechnology* **18**(19), 195301 (2007).

[129] Sun, Y., Mortensen, H., Schär, S., Lucier, A., Miyahara, Y., Grütter, P., and Hofer, W. *Physical Review B* **71**(19), 193407 May (2005).

[130] Zhou, J., Fei, P., Gao, Y., Gu, Y., Liu, J., Bao, G., and Wang, Z. L. *Nano Letters* **8**(9), 2725–2730 (2008).

[131] Wang, Z. L. *Advanced Materials* **21**(13), 1311–1315 (2009).

[132] Smit, G. D. J., Rogge, S., and Klapwijk, T. M. *Applied Physics Letters* **81**(20), 3852 (2002).

[133] Krusemeyer, H. J. *Physical Review* **114**(3), 655 May (1959).

[134] Klingshirn, C. *physica status solidi (b)* **244**(9), 3027–3073 (2007).

[135] Aranovich, J. *Journal of Vacuum Science and Technology* **16**(4), 994 (1979).

[136] Sberveglieri, G. *Sensors and Actuators B: Chemical* **23**(2-3), 103–109 February (1995).

[137] Pearton, S. J., Norton, D. P., Ip, K., Heo, Y. W., and Steiner, T. *Journal of Vacuum Science & Technology B: Microelectronics and Nanometer Structures* **22**(3), 932 (2004).

[138] Schmidt, O., Geis, A., Kiesel, P., de Walle, C. G. V., Johnson, N. M., Bakin, A., Waag, A., and Döhler, G. H. *Superlattices and Microstructures* **39**(1-4), 8–16 January (2006).

[139] Collins, R. *Physical Review* **112**(2), 388–395 (1958).

[140] Beinik, I., Kratzer, M., Wachauer, A., Wang, L., Teichert, C., Piryatinski, Y. P., Brauer, G., Chen, X., and Djurisic, A. *in preparation* (2011).

[141] Zhang, D. *Materials Chemistry and Physics* **45**(3), 248–252 September (1996).

[142] Liu, P., She, G., Liao, Z., Wang, Y., Wang, Z., Shi, W., Zhang, X., Lee, S., and Chen, D. *Applied Physics Letters* **94**(6), 063120 (2009).

[143] Lany, S. and Zunger, A. *Physical Review B* **72**(3), 035215 July (2005).

[144] Brillson, L. J. *Surfaces and Interfaces of Electronic Materials*. Wiley-IEEE, Weinheim, (2010).

[145] Lang, W., Marksteiner, M., Bodea, M., Siraj, K., Pedarnig, J., Kolarova, R., Bauer, P., Haselgrübler, K., Hasenfuss, C., Beinik, I., and Teichert, C. *Nuclear Instruments and Methods in Physics Research Section B: Beam Interactions with Materials and Atoms* **In Press, Available online**.

[146] Watt, F., Bettiol, A. A., Kan, J. A. V., Teo, E. J., and Breese, M. B. H. *International Journal of Nanoscience* **4**(3), 269–286 (2006).

[147] Masuda, H., Takeuchi, M., and Takahashi, T. *Ultramicroscopy* **105**(1-4), 137–142 (2005).

[148] Rodriguez, B. J., Callahan, C., Kalinin, S. V., and Proksch, R. *Nanotechnology* **18**(47), 475504 (2007).

List of Acronyms

ACM	Autocorrelation Height Map.
ADC	Analog-to-Digital Converter.
ADs	Arrowhead Defects.
AM	Amplitude Modulation.
APB	Antiphase Borders.
APD	Antiphase Domains.
BV	Bucking Voltage.
C-AFM	Conductive Atomic Force Microscopy.
CPD	Contact Potential Difference.
DC	Direct Current.
DLS	Defect Localized States.
DOS	Density of States.
EFM	Electrostatic Force Microscopy.
ER	Einstein Relation.
F-N	Fowler-Nordheim Tunneling.
FIB	Focused Ion Beam.
FM	Frequency Modulation.
FTO	Fluorine-doped Tin Oxide.
HT	Hydrothermal Growth.
HTSC	High-Temperature Superconductors.
I-V	Current-to-voltage curves.
KPFM	Kelvin Probe Force Microscopy.
MBE	Molecular Beam Epitaxy.
MIBS	Masked Ion-Beam Structuring.
MIS	Metal-Insulator-Semiconductor.
ML	Monolayer.
MOVPE	Metalorganic Vapor Phase Epitaxy.
NDs	Nanodots.
NRs	Nanorods.
NWs	Nanowires.
OA	Operational Amplifiers.
P-F	Poole-Frenkel Emission.

PA-KPFM	Photo-Assisted KPFM.
PC-AFM	Photoconductive AFM.
PFM	Piezoresponse Force Microscopy.
PHS	Perturbed Host State.
PL	Photoluminescence.
QRs	Quantum Rings.
SCLC	Space Charge Limited Current.
SCM	Scanning Capacitance Microscopy.
SEM	Scanning Electron Microscopy.
SPM	Scanning Probe Microscopy.
SPV	Surface Photovoltage.
SSRM	Scanning Spreading Resistance Microscopy.
STM	Scanning Tunneling Microscopy.
TE	Thermal Evaporation.
TEM	Transmission Electron Microscopy.
TR-PL	Time-Resolved Photo Luminescence.
UHV	Ultra High Vacuum.
UNCD	Ultrananocrystalline Diamond.
XRD	X-ray Diffraction.
YBCO	$YBa_2Cu_3O_7$.